



## **Terms and Conditions of Use of Digitised Theses from Trinity College Library Dublin**

### **Copyright statement**

All material supplied by Trinity College Library is protected by copyright (under the Copyright and Related Rights Act, 2000 as amended) and other relevant Intellectual Property Rights. By accessing and using a Digitised Thesis from Trinity College Library you acknowledge that all Intellectual Property Rights in any Works supplied are the sole and exclusive property of the copyright and/or other IPR holder. Specific copyright holders may not be explicitly identified. Use of materials from other sources within a thesis should not be construed as a claim over them.

A non-exclusive, non-transferable licence is hereby granted to those using or reproducing, in whole or in part, the material for valid purposes, providing the copyright owners are acknowledged using the normal conventions. Where specific permission to use material is required, this is identified and such permission must be sought from the copyright holder or agency cited.

### **Liability statement**

By using a Digitised Thesis, I accept that Trinity College Dublin bears no legal responsibility for the accuracy, legality or comprehensiveness of materials contained within the thesis, and that Trinity College Dublin accepts no liability for indirect, consequential, or incidental, damages or losses arising from use of the thesis for whatever reason. Information located in a thesis may be subject to specific use constraints, details of which may not be explicitly described. It is the responsibility of potential and actual users to be aware of such constraints and to abide by them. By making use of material from a digitised thesis, you accept these copyright and disclaimer provisions. Where it is brought to the attention of Trinity College Library that there may be a breach of copyright or other restraint, it is the policy to withdraw or take down access to a thesis while the issue is being resolved.

### **Access Agreement**

By using a Digitised Thesis from Trinity College Library you are bound by the following Terms & Conditions. Please read them carefully.

I have read and I understand the following statement: All material supplied via a Digitised Thesis from Trinity College Library is protected by copyright and other intellectual property rights, and duplication or sale of all or part of any of a thesis is not permitted, except that material may be duplicated by you for your research use or for educational purposes in electronic or print form providing the copyright owners are acknowledged using the normal conventions. You must obtain permission for any other use. Electronic or print copies may not be offered, whether for sale or otherwise to anyone. This copy has been supplied on the understanding that it is copyright material and that no quotation from the thesis may be published without proper acknowledgement.



# Paramagnetic Defects in Thin Carbon Films

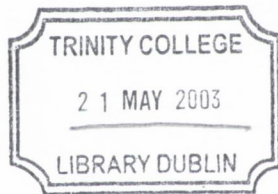
by

Benjamin James Jones

Submitted for the degree of  
Doctor in Philosophy  
of the University of Dublin

Department of Physics  
Trinity College Dublin

January 2003



THESIS  
~~7553~~  
703

## Declaration

I declare that the work in this thesis has not been previously submitted as an exercise for a degree to this or any other university. The work described herein is entirely my own, except where acknowledged in the text. I agree that this thesis may be freely lent or copied, provided original authorship is accredited.

A handwritten signature in black ink, appearing to read 'Benjamin Jones', with a large, sweeping flourish at the end.

Benjamin James Jones

January 2003

## Summary

This thesis is an investigation into paramagnetic defects in thin carbon films, their nature and the effects of deposition parameters and post deposition treatments. Electron paramagnetic resonance (EPR) is used to examine samples with a wide range of structures from the hard tetrahedral amorphous carbons (ta-C) with a high percentage of  $sp^3$  bonded carbon, to soft polymer-like films with high hydrogen concentrations, grown by plasma enhanced chemical vapour deposition at low bias.

Some samples were, post manufacture, subjected to implantation of a range of ion species with doses of up to  $2 \times 10^{16} \text{ cm}^{-2}$ . The EPR measurements show that the defect associated with carbon has a volume spin density that increases approximately linearly with dose, to  $2.7 \times 10^{20} \text{ cm}^{-3}$  for implantation of  $2 \times 10^{16} \text{ ions cm}^{-2}$ . At high doses the carbon line narrows (to 0.13 mT at  $2 \times 10^{16} \text{ ions cm}^{-2}$ ), and the spin-lattice relaxation time decreases and approaches the spin-spin relaxation time; this is attributed to motional narrowing of the signal, resulting from greater wavefunction overlap. This in turn may arise from increased delocalisation due to an increase in  $sp^2$  cluster size.

EPR was carried out on films with a variety of structures, at temperatures from 5K to 300K and at two frequencies ( $\approx 9.5 \text{ GHz}$  and  $\approx 94 \text{ GHz}$ ). For all films at all temperatures and frequencies studied, the EPR signal due to unpaired carbon spins is observed to be a single symmetric line. For all samples studied, room temperature EPR shows that there is little or no increase in the width of the resonance line with increasing microwave frequency. This shows that there is little or no linewidth component due to a spread in  $g$ -values.

The temperature dependence of the susceptibility shows adherence to the Curie law at temperatures above  $\approx 13 \text{ K}$ . Below this temperature some deviation from this dependence may occur, possibly due to the onset of local magnetic ordering, further evidence of which comes from the presence of a magnetic hysteresis loop at 5K.

Measurements of the temperature dependence of the X-band EPR linewidth and relaxation times show that exchange interaction, rather than variable range hopping, becomes increasingly dominant as the  $sp^2$  content of the films is increased. Strong evidence for this is the highly “graphite-like” sample, which shows no variation of linewidth or relaxation time, within error, over the entire temperature range studied.

Measurements on “diamond-like” and “graphite-like” carbon show that the position of resonance at low temperature displays a dependence on the orientation of the sample within the field. Detailed analysis shows that this anisotropy can be attributed to shape effects associated with the anisotropy of the demagnetising field, the effect can be explained in terms of magnetization of unpaired carbon electrons.

In contrast to the X-band measurements, at W-band the linewidths of the diamond-like and graphite-like films increase substantially as the temperature is lowered from room temperature to 5K (the strongest increase, from 4.8G to 24.3G, is seen in sample C320). This increase in width is correlated with, and is approximately the same magnitude as, the shift in resonance position. Thus the broadening of the line is attributed to variation in the demagnetising field over the sample, causing a spread in effective  $g$  value and therefore increasing the linewidth.

Nitrogen incorporation into amorphous hydrogenated carbon (a-C:H) films is shown to decrease the defect density in all types of films studied. This is attributed to a decrease in the disorder of the  $sp^2$  structure, the aromatic rings becoming less buckled and distorted and thus allowing greater delocalisation. The linewidth decrease associated with this fall in spin density, as predicted by a model assuming dipolar broadening, is observed only for polymer-like films. A reduction in exchange narrowing for the highly nitrogenated films could outweigh the effect of the dipolar interaction and result in the broadening of lines with the addition of nitrogen, as observed in the more diamond-like films. Comparing measurements with simulated spectra shows that at most one in one million of the incorporated nitrogen atoms act as donors.

In summary, this work provides a comprehensive, coherent picture of the nature of paramagnetic defects within amorphous carbon thin films.

## **Acknowledgements**

My thanks and appreciation are due to my supervisor Dr. Robert (Bob) Barklie for his guidance, encouragement and unflagging enthusiasm.

For supply of the amorphous carbon films under study in this work, I thank Drs. Riz Khan and David Carey, and Prof. Ravi Silva at the University of Surrey; Prof. John Robertson and Dr. Manish Chhowalla at the University of Cambridge; Dr. Paul Maguire from the University of Ulster at Jordanstown and Dr. Christian Godet of Ecole Polytechnique, Paliseau.

Thanks also to Drs. Smith and El Mkami of the University of St. Andrews, for help and guidance with W-band experiments, Dr. M Venkatesan for SQUID measurements and munificent loan of low temperature apparatus, and Chris Smith for ellipsometry measurements and analysis.

Dr. Michael Collins worked indefatigably creating and editing software. Pat Flanagan and Ken Concannon provided valuable technical support in the face of strong opposition from the equipment, whilst Liz Grey, Michelle Duffy, Susan Priest and Suzanne Richmond assisted with logistics and narrow doorways.

My whole hearted thanks go to Steven Watterson, Simon Branford, Mia Kjellsdotter Karlsson, Michelle Apostolides, Alex Scroxtton and David Griffiths for providing support whilst only causing minor rises in the sea of insanity; Tricia Jones for English proof reading, and Justin Wells for solidarity and coffee.

# Contents

Declaration	i
Summary	ii
Acknowledgements	iv
Contents	v
1. Introduction	1
1.1. References	4
2. Amorphous Carbon Films: Deposition and structure	5
2.1. Introduction	5
2.2. Carbon Films	
2.2.1. Carbon Bonding	5
2.2.2. Types of a-C and a-C:H films	7
2.2.3. a-C (:H) structure and models	8
2.2.4. Defects	10
2.2.5. Film conditioning	11
2.3. Plasma enhanced chemical vapour deposition, PECVD	
2.3.1. Details of apparatus	11
2.3.2. Properties of PECVD films (a-C:H)	12
2.4. Integrated Distributed Electron Cyclotron Resonance, IDECR	14
2.5. Filtered cathodic vacuum arc, FCVA	15
2.5.1. Description of technique	16
2.5.2. Properties of FCVA films (a-C and a-C:H)	16
2.6. References	18
3. Electron Paramagnetic Resonance (EPR)	20
3.1. Basic Principles	20
3.2. g-values and spin density	23
3.3. Simple models of lineshape	26

3.3.1. Relaxation time, $T_1$ , Transition Probability Derivation.	26
3.3.2. Contributions to Transition Probabilities, Mechanisms for $T_1$	27
3.3.3. Spin Temperature	28
3.3.4. Bloch Model	29
3.4. High Frequency measurements, Dispersion	32
3.5. Line broadening mechanisms	
3.5.1. Homogeneous Broadening	35
3.5.2. Inhomogeneous Broadening	36
3.6. Motional Narrowing	38
3.6.1. Exchange Narrowing	40
3.7. Calculation of Relaxation Times from Spectra	
3.7.1. Simple lines	42
3.7.2. Voigt shape lines	43
3.8. References	46
4. Ion Implanted Polymer-like Amorphous Carbon	47
4.1. Introduction	47
4.2. Film characteristics	48
4.3. Defect variation with implantation dose	51
4.4. Annealing	58
4.5. Carbon and nitrogen implantation	59
4.6. Conclusion	60
4.7. References	61
5. Nitrogen inclusion	62
5.1. Introduction	62
5.2. Nitrogen in a-C:H	63
5.3. Film Properties	65
5.4. EPR Results	
5.4.1. Polymer like Films ("GQ")	68
5.4.2. Diamond-like films ("GR")	71

5.4.3. Intermediate films ("GS")	76
5.5. Discussion	79
5.6. Conclusions	81
5.7. References	82
6. Nature of Defects	85
6.1. Introduction	85
6.2. Experimental	86
6.2.1. Analysis of W-band spectra	88
6.3. Curie-like susceptibility	
6.3.1. Introduction	90
6.3.2. Results and discussion	91
6.3.2.1. Instrumental effects	93
6.3.2.2. Real effects	96
6.3.3. Conclusions	100
6.4. Line broadening and narrowing mechanisms	
6.4.1. Introduction	101
6.4.2. Experimental	102
6.4.3. Results	
6.4.3.1. X-Band linewidths	103
6.4.3.2. Relaxation times	105
6.4.3.3. W-Band linewidths	107
6.4.4. Discussion	
6.4.4.1. g value spread	109
6.4.4.2. Exchange narrowing	109
6.4.4.3. Hopping	111
6.4.5. Conclusions	116
6.5. Anisotropy and demagnetising factor	
6.5.1. Introduction	118
6.5.2. Resonance position versus orientation	118
6.5.3. Resonance shift versus temperature and spin concentration	120
6.5.4. Discussion	123

6.5.4.1.	Mathematical analysis of demagnetising factor	124
6.5.4.2.	Orientation dependence of resonance position	126
6.5.4.3.	Resonance shift versus temperature and spin concentration	126
6.5.4.4.	Linewidth versus temperature	129
6.5.5.	Conclusions	130
6.6.	Low temperature lineshape	
6.6.1.	Introduction	131
6.6.2.	Results and discussion	133
6.6.3.	Conclusion	136
6.7.	Conclusions on the nature of defects	137
6.8.	References	139
7.	Other Experiments	143
7.1.	Defect location and concentration in ta-C and ta-C:N	
7.1.1.	Introduction	144
7.1.2.	Experimental	145
7.1.3.	Results and discussion	147
7.1.3.1.	Un-etched ta-C films	147
7.1.3.2.	Un-etched ta-C:N films	148
7.1.3.3.	sp <sup>2</sup> surface layer, etched samples	150
7.1.4.	Conclusions	152
7.2.	Influence of substrate temperature on defects in tetrahedral amorphous carbon (ta-C) films	
7.2.1.	Introduction	153
7.2.2.	Results and discussion	155
7.2.3.	Conclusions	159
7.3.	Characteristics of PECVD a-C:H films as a function of rf-power	160
7.4.	Depth profile of defects in diamond-like carbon films	
7.4.1.	Introduction	164
7.4.2.	Experimental	165
7.4.3.	Results and discussion	
7.4.3.1.	Defect Densities	166

7.4.3.2. Linewidths and relaxation times	168
7.4.4. Conclusions	170
7.5. References	171
8. Overall Conclusions	173
8.1. References	177
Appendices	
A. Temperature dependence – Calculating $\chi$	I
B. Temperature dependence – Measuring $\chi$	V
C. Related Publications	IX

# *Chapter 1*

## *Introduction*

A man will turn over half a library,  
to make one book.

-Samuel Johnson

# 1. Introduction

Amorphous carbon (a-C) is a very versatile material. It can be deposited as a uniform flat film over a large area, and by changing deposition conditions its electronic and topological properties can be adjusted over a wide range [1, 2].

Plasma enhanced chemical vapour deposition, PECVD, uses a plasma of gases, such as methane, to manufacture films with a variety of structures, ranging from soft “polymer-like” carbons, with high hydrogen content and low defect density, through “diamond-like” harder films, to “graphite-like” carbons with a high fraction of  $sp^2$  bonded carbon.

Filtered cathodic vacuum arc (FCVA) systems can be used to create films without hydrogen, including the tetrahedral amorphous carbon (ta-C) with a high percentage of “diamond”  $sp^3$  bonds.

The properties of amorphous carbon films are not solely determined by hydrogen content and  $sp^2$  fraction, they are also affected by medium range order. The olefinic chains and aromatic rings are thought to form clusters of  $sp^2$  bonded carbon in the  $sp^3$  matrix. [3, 4]

Because of this wide range of properties and ability to make films of a large area, research is being conducted into the use of a-C, and hydrogenated amorphous carbon, a-C:H, in an extensive number of applications. Possible uses range from hard disk coatings, to razor blades, to medical applications such as bio-compatible

hip-replacement joint coatings, to flat panel displays, water treatment and solar cells. [1, 2, 5]

Some applications also take advantage of the fact that ion species can be added to the film, either in the gaseous form added to the plasma gas mix, or post-deposition by ion implantation.

All amorphous carbon contains defects, which may, for example, be dangling bonds or odd-numbered graphite rings. Defects affect the properties of the films and many applications require the concentration of such defects to be reduced. Thus the nature of defects, and the effects of manufacturing conditions and post-deposition treatment on the defects, and on the film structure, need to be examined to facilitate the greater use of this material.

In this work I use electron paramagnetic resonance (EPR) to examine a-C(:H) films made by both PECVD and FCVA. Paramagnetic defects can be observed using this technique; the intensity of the resonance line gives the population, and hence if the volume is known, the average concentration of defects. The shape and width of the EPR line, and how it changes with temperature, microwave power and frequency, can give valuable insights into the nature of the material.

After introducing the material and technique in chapters two and three, I look at the effects of implanting nitrogen, boron and carbon ions into polymer-like films, in a variety of doses, and show how this implantation affects the concentration of defects and structure and ordering of carbon within the film.

Chapter five concentrates on the effect of the addition of nitrogen to films deposited by integrated distributed electron cyclotron resonance (IDECR) PECVD. Carbon nitride film deposition is an expanding area of interest due to the recent desire to find the  $\beta$ - $C_3N_4$  compound, expected to have a hardness greater than that of diamond [6]. Whilst this has not been discovered, films with <57% nitrogen show interesting properties and this chapter is devoted to showing how the structure and defects of the films are affected by increasing nitrogen content.

In chapter six I report on experiments involving the variation of temperature and frequency at which EPR measurements are conducted. The Curie-like dependence of susceptibility; the causes of line broadening and narrowing; and anisotropy observed in the orientation dependence of the EPR signal at low temperatures, are all investigated in this extensive chapter. I also try to replicate previous work [7] that finds powder pattern spectra initially claimed to arise from carbon unpaired electrons in  $sp^2$  clusters.

Chapter seven is an investigation into the effect of deposition temperature on film structure and the uniformity of distribution of unpaired spins within diamond-like carbon. Films of various thicknesses are examined to obtain a depth profile of the defects in the material.  $ta$ -C films are studied to discover whether the  $sp^2$  region on the surface of the film [8] contains the majority (or a number disproportionate to its size) of the defects within the film, as previous EPR measurements [9] have suggested spins are concentrated in  $sp^2$  regions of these highly  $sp^3$ -bonded films.

In chapter eight the work outlined above is used to draw conclusions on the nature of paramagnetic defects in thin carbon films.

## 1.1 References

- [1] M. Lacerda, M. Lejeune, B.J. Jones, R.C. Barklie, R. Bouzerar, K. Zellama, N.M.J. Conway, C. Godet *J. Non-Cryst. Solids* 299-302(2002)907
- [2] S.R.P. Silva, J. Robertson, W.I. Milne and G.A.J. Amaratunga eds. "*Amorphous Carbon: State of the Art*" pub. World Scientific Singapore (1998)
- [3] J. Robertson, E.P. O'Reilly *Phys. Rev. B* 35(1987)2946
- [4] J. Robertson *J. Non-Cryst. Solids* 198-200(1996)615
- [5] S.R.P. Silva, J. Robertson, Rusli, G.A.J. Amaratunga *Phil. Mag. B* 74(1996)369
- [6] K. Kitaguchi, H. Kiyota, M. Iida, T. Kurosu, T. Ando, I. Kusunoki *Diamond 2000 presentation chair J. Robertson* (2000)5.7.03
- [7] H.J. von Bardeleben, J.L. Cantin, A. Zeinert, B. Racine, K. Zellama, P.N. Hai *Appl. Phys. Lett.* 78(2001)2843
- [8] C.A. Davis, G.A.J. Amaratunga, K.M. Knowles *Phys. Rev. Lett* 80(1998)3280
- [9] S. Sattel, J. Robertson, H. Ehrhardt *J. Appl. Phys.* 82(1997)4566

## *Chapter 2*

### *Amorphous Carbon*

And malt does more than Milton can,  
To justify God's ways to man.

A.E. Housman

## 2. Amorphous Carbon Films: Deposition and structure

### 2.1 Introduction

Amorphous carbon (a-C) and amorphous hydrogenated carbon (a-C:H) deposited from medium energy ions contain both  $sp^2$  and  $sp^3$  sites and it is possible to vary the relative fraction of the bonds by controlling the deposition conditions. The properties of the films, such as hardness, band gap and conductivity can then be optimised for different applications. [1, 2, 3]

Amorphous carbon films can be grown by various methods, including plasma enhanced chemical vapour deposition (PECVD) and filtered cathodic vacuum arc (FCVA) techniques. In this chapter I describe the types or classifications of a-C and a-C:H, as well as outlining the various methods of film deposition, and the characteristics of the films grown by each method.

### 2.2 Carbon Films

#### 2.2.1 Carbon Bonding

Unlike silicon and other group IV elements, which hybridise almost exclusively to  $sp^3$ , carbon can easily hybridise to  $sp^1$ ,  $sp^2$  and  $sp^3$  configurations, as shown schematically in figure 2.1 below [3]

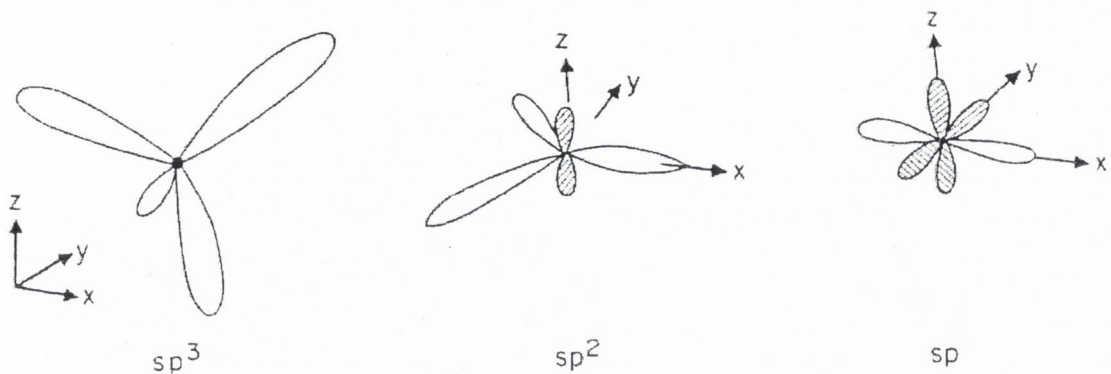


**Figure 2.1** Schematic representation of  $sp^3$ ,  $sp^2$  and  $sp$  hybridised atoms.

In  $sp^3$  configuration (as in diamond) each of the carbon's valence electrons is in a tetrahedrally directed orbital which forms a strong sigma ( $\sigma$ ) bond with an adjacent atom. A material, such as crystalline diamond, consisting only of carbon bonded with such single bonds, is said to be "saturated", has a wide (5.5eV) band gap, is strong and exhibits low conductivity [3,4].

If the atom is in  $sp^2$  configuration, one electron lies in a  $p\pi$  ( $p_z$ ) orbital lying normal to the plane containing the other three valence electrons, assigned to trigonally  $sp^2$  hybrids forming  $\sigma$  bonds. The  $p\pi$  orbital forms  $\pi$  bonds with adjacent  $p\pi$  orbitals, atoms joined with both  $\sigma$  and  $\pi$  bonds are said to be double bonded. Graphite consists of "aromatic" six-membered rings of  $sp^2$  bonded carbon, in layers which are weakly bonded together by van der Waals forces, with the  $\pi$ -electrons delocalising over an entire graphite layer [4]. Thus the strength and conductivity of graphite are high along the basal plane but correspondingly low on an axis normal to this.

Finally, in  $sp$  bonded carbon, two electrons lie in orthogonal  $p_y$  and  $p_z$  orbitals which form  $\pi$  bonds, the two others forming  $\sigma$  bonds.[3]

Amorphous carbon, then, in both its hydrogenated and non-hydrogenated forms, with concentrations of  $sp^2$  and  $sp^3$  bonded carbon that can be varied according to deposition and treatment conditions can, qualitatively, have structure and properties ranging from somewhat similar to those of diamond to those of graphite. This is discussed in detail in later sections; however, as an example, room temperature conductivity,  $\sigma_{RT}$ , and band gap,  $E_g$ , of graphite, a-C:H and diamond are listed in table 2.1 below [1, 5-9]

	Graphite	a-C:H	Diamond
$\sigma_{RT} / \Omega^{-1} \text{cm}^{-1}$	$2.5 \times 10^4$	$10^{-7}$ to $10^{-16}$	$10^{-18}$
$E_g$ (eV)	-0.04	1 to 4	5.5

**Table 2.1** Summary of properties of forms of carbon.

### 2.2.2 Types of a-C and a-C:H films

The  $sp^3$  fraction and hydrogen content affect the properties of the films such as hardness, band gap (which can be varied from about 1 to 4eV), photoluminescence and conductivity [1, 3]. It is convenient, therefore, to divide the films into different categories dependent on their properties and structure. The composition of various categories can best be displayed in a 'ternary phase diagram' (figure 2.2), which indicates the  $sp^2$ ,  $sp^3$  and hydrogen content for each type of film. The following categories are often used: 'polymer-like' amorphous carbon, PAC, is a soft film with a high, ~50%, hydrogen content and high  $sp^3$  fraction; DLC, diamond-like carbon, is harder, has a lower hydrogen content, a high  $sp^3/sp^2$  ratio, and generally has a higher

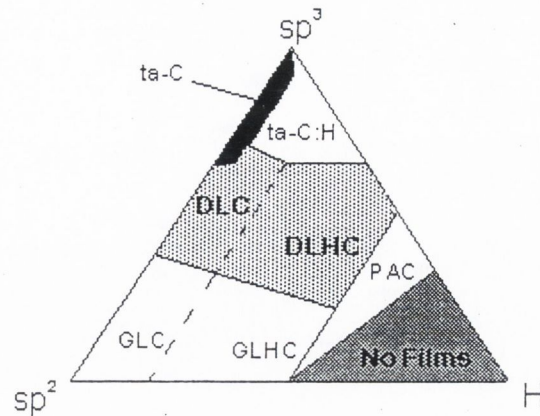


**Figure 2.2** Ternary phase diagram of types of a-C and a-C:H

defect concentration than PAC. DLC films with a very high  $sp^3$  content,  $\approx 85\%$ , are often described as tetrahedral amorphous carbon, ta-C. Films with a high  $sp^2$  content are referred to as 'graphite-like' carbon, GLC. GLC, DLC and ta-C films with a hydrogen content in the region of  $\approx 30-50\text{at.}\%$  are sometimes described as 'hydrogenated' and are denoted as GLHC, DLHC and ta-C:H, though the nomenclature in the literature is dependent on author.

### 2.2.3 a-C (:H) structure and models

Figure 2.2 shows the composition of various types of film; the corners represent 100%  $sp^3$ ,  $sp^2$  and hydrogen content, as indicated, with smaller amounts of that property at further points [1]. The shaded area in the hydrogen - rich corner marks the region in which no stable films can be formed, and is limited by long-chain polymers such as polyethylene ( $[-CH_2-CH_2]_n$ ) with 67at.% H, 33%  $sp^3$  and polyacetylene ( $[-CH=CH]_n$ ) with 50at.% H and 50%  $sp^2$ . Any further incorporation of hydrogen in such polymers

can only result from the breaking of carbon-carbon bonds, i.e. the creation of smaller chains, and eventually of volatile hydrocarbons (and finally H<sub>2</sub> gas, which will not stay on the substrate) [10]

In all cases, other than perhaps the highly tetrahedral ta-C with >90% sp<sup>3</sup> bonding, the optical band gap is determined by the  $\pi$  and  $\pi^*$  states associated with the p electron orbitals of sp<sup>2</sup> bonded carbon in the amorphous matrix; a schematic density of states is shown in figure 2.3 [3,11].

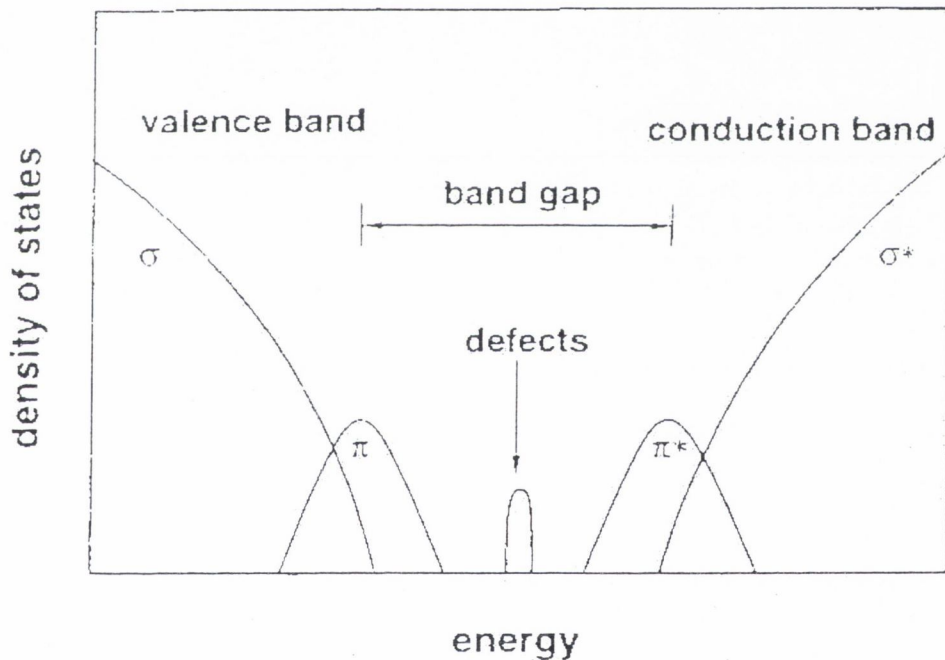


**Figure 2.3** Schematic representation of density of states in a-C:H

sp<sup>2</sup>, sp<sup>3</sup> and hydrogen content, whilst defining the short range order of a-C and a-C:H do not entirely define the structure of the material, as there may be a certain degree of medium range order, i.e. segregated regions of sp<sup>2</sup>, that affect the properties of the film. Studies by Robertson and O'Reilly [12] (later revised by Robertson [13])

suggest that  $sp^2$  sites in a-C(:H) films cluster together in the form of olefinic chains or aromatic rings, and that the size of these clusters determines the optical properties, such as Tauc gap, of the films. The room temperature conductivity is then thought to be governed by hopping between these clusters.

## 2.2.4 Defects

All methods of production result in a-C(:H)(:N) films containing defects, the full nature of which is elusive, but which affect the electrical and optical properties of the film including photoluminescence and ability to dope the material [3,14]

Electron paramagnetic resonance (EPR) techniques can detect paramagnetic defects, which could be aromatic rings of  $sp^2$  type carbon, with an odd number of sites, or single dangling bonds. The concentration of such defects is typically between  $10^{17}$  and  $10^{21}$  per cubic centimetre, depending on the type of film (PLC, DLC etc), method of production (for example IDECR or FCVA) and post-deposition treatments to which the film has been subjected, such as annealing or ion implantation [3,14,15].

Carbon is stable in both  $sp^2$  and  $sp^3$  hybridised states, unlike the extensively studied silicon, (there is little evidence for  $sp$  in unhydrogenated amorphous carbon [3]); thus the chemistry of a-C suggests that its defects are more complicated than in a-Si, where defects are created by breaking  $\sigma$  bonds, in a-C defects can be formed by breaking either a  $\sigma$  bond or a  $\pi$  bond.

Though EPR does not allow different types of carbon defect to be easily distinguished (the g-value of the resonance line is always close to 2.0028 [15,16]) Robertson [3]

defines a dangling bond as an isolated 3-fold co-ordinated carbon site, with a creation energy,  $E_d \sim 1.8\text{eV}$ , estimated from the  $\sigma$  bond energy, compared to an average  $E_d$  of  $\pi$ -defects of  $0.4\text{eV}$ . Due to their lower creation energy (which decreases with increasing size of aromatic ring clusters)  $\pi$  defects are expected to predominate.

Contrary to the case of defects in silicon, which are attributed to neutral dangling bonds [17] the defects in a-C are not passivated by hydrogenation, even though the concentration of hydrogen in a-C:H can be  $\sim 50\%$  [17]. However, it has been suggested that incorporating hydrogen in the films can reduce the number of defects by allowing stress in highly  $\text{sp}^3$  bonded carbon to be reduced [10,14].

### 2.2.5 Film conditioning

Attempts have been made by various producers to further adjust the electronic properties of the films by annealing, or by adding dopant species, either during film production or by ion implantation after deposition. This is discussed in greater detail in later sections.

## 2.3 Plasma enhanced chemical vapour deposition, PECVD

### 2.3.1 Details of apparatus

Figure 2.4 shows a schematic set-up of a typical PECVD apparatus.

For thin film deposition the system is evacuated to a pressure of  $\sim 10^{-5}$  mbar. The substrate can then be sputtered clean by use of (for example) a short ( $\sim 10$  min) argon discharge. Subsequently a hydrocarbon gas (such as methane) is leaked into the system, the hydrocarbons are then partially ionised and cracked in the rf discharge.

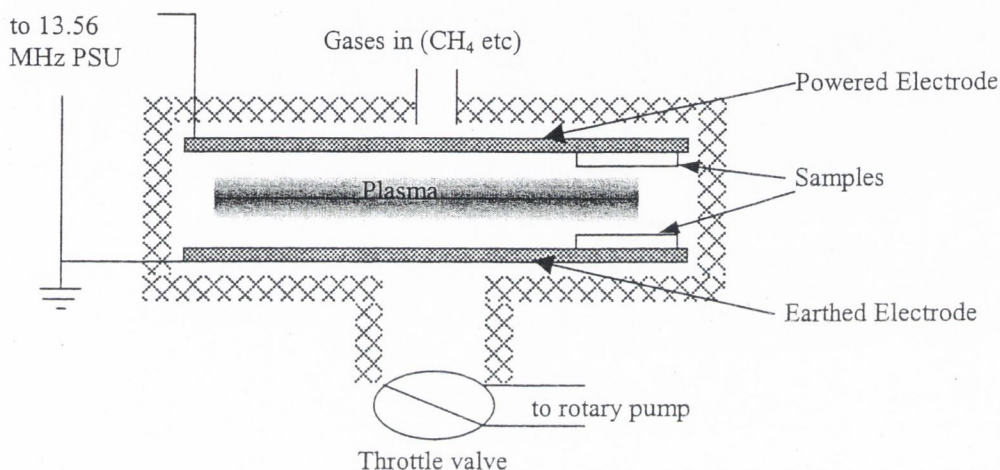


**Figure 2.4** Schematic of a PECVD apparatus

Within the ion sheath region the positively charged particles are accelerated towards the substrate. The geometry of the reactor causes a negative self-bias to arise on the small capacitively coupled powered electrode. Neglecting the small contribution from the plasma potential, the sheath potential is given by the bias voltage, which can be easily monitored, and varied by changing the rf-power. [18]

### 2.3.2 Properties of PECVD films (a-C:H)

The properties of a-C:H films grown by PECVD are strongly affected by the kinetic energy of the ions bombarding the growing film surface [19]. However, the ion energy is not directly accessible, and the varied parameters are the gas pressure, P,

giving the mean free path, and bias voltage,  $V_B$ , which gives the average potential over which the ions forming the thin film are accelerated. The average ion energy follows the empirical relation [18]:

$$2.1 \quad E_{\text{ion}} \propto V_B / P^{0.5}$$

With PECVD a range of ion species (for example  $C^+$ ,  $CH_4$ ) is deposited with various energies. At low bias voltages (i.e. low ion energies) the films deposited are “polymer-like” amorphous carbon (PAC), with wide optical gaps, a high photoluminescence (PL) efficiency and a high (~50at.%) hydrogen content, these films can possess a high  $sp^3$  fraction because hydrogen stabilises  $sp^3$  hybridised carbon and reduces the number of bond length and angle distributions, and thus the stress, in a-C:H [10,14]. With increasing incident ion energy the film becomes diamond like (DLC) harder, with a smaller gap. The hydrogen content is decreased and  $sp^2$  bonding is therefore favoured, the  $sp^3$  fraction is found to be approximately 20-30%. Such DLC films have been extensively studied [10]. The  $sp^2$  fraction increases with further increases in bias voltage, eventually resulting in graphite like carbon (GLC) [14]. The variation with bias voltage of  $sp^3$  fraction, hydrogen content and Tauc gap is shown in figure 2.5 [20]. There is an empirical relation between Tauc gap and  $sp^2$  content; as  $sp^2$  content increases the size of the  $sp^2$  clusters generally increases. Robertson [13] shows that the gap,  $E_g$ , is related to  $M$ , the number of rings in the  $sp^2$  clusters by

$$2.2 \quad E_g \approx \frac{3}{M^{1/2}} \text{ eV}$$

Note that different precursor gases can be used to give greater flexibility over film property selection.

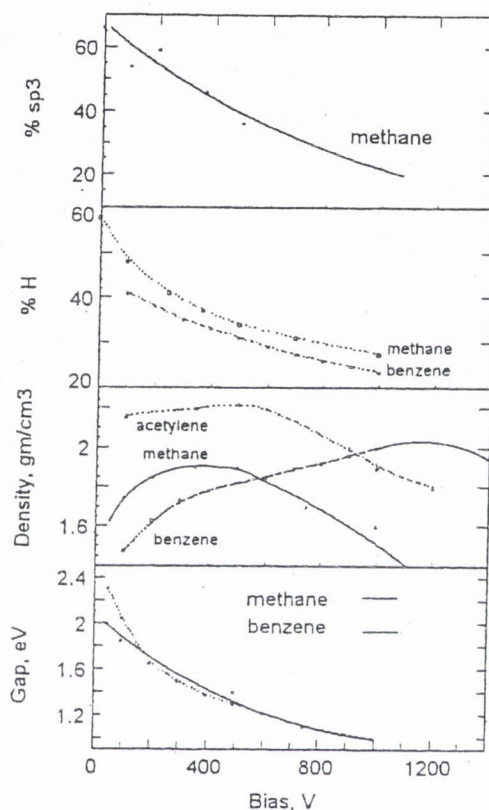


**Figure 2.5** Variation with bias voltage of properties of films deposited by PECVD using a variety of precursor gases.

## 2.4 Integrated Distributed Electron Cyclotron Resonance, IDECR

As an enhancement of plasma deposition, IDECR allows synthesis of dense and conducting carbon based films, on large area substrates, at a high growth rate using low temperature plasmas. This may help to solve problems related to the future development of carbon based electronic devices.[21]

The IDECR reactor used by Dr. Christian Godet in Ecole Polytechnique, Palaiseau, used to produce a-C:N films extensively studied as reported in chapter five, is described in detail elsewhere [22-24]. This reactor consists of four microwave antennae with permanent magnets along their lengths. The frequency and field are selected to obtain the electron cyclotron resonance (ECR) condition, which results in high ionisation and high plasma density. An ECR plasma from methane or acetylene precursor gases can be used to synthesise a-C:H and, with the addition of nitrogen to the precursor gas mix, carbon nitride, a-C<sub>1-x</sub>:N<sub>x</sub>:H, films. The concentration of nitrogen atoms (N/N+C) is restricted by ion-assisted chemical etching mechanisms and therefore limited by a vanishing film growth rate at a maximum of (N/N+C) = 0.35. The energy of the ions impinging on the film is controlled by varying the rf-power supplied to the substrate, which, as in PECVD, is one of the most important parameters determining the film structure and properties [21].

## 2.5 Filtered cathodic vacuum arc, FCVA

Filtered vacuum arc carbon evaporation has been proven as a promising technique to produce a carbon ion beam and to deposit films that are almost microparticle free for opto-electronic applications [25]. It is, however, a relatively new option for deposition of carbon films and investigation into the influence of different parameters is ongoing [25].

### 2.5.1 Description of technique

The core of all arc discharge phenomena is the arc spot, that is an ensemble of emission centres and plasma streams, perpendicular to the cathode surface. The current density at an individual spot is  $\sim 10^8 \text{ A cm}^{-2}$  and causes explosive evaporation of the localised region of the graphite surface in a time period of a few nanoseconds. The localised high temperature of the area of high pressure around the spot results in thermal shock and the consequent ejection of graphitic material, referred to as microparticles, which may be a source of defects in tetrahedral amorphous (hydrogenated) carbon grown by FCVA, but do not seem to be the main source of paramagnetic defects, as detected by EPR [26]. The incorporation of such microparticles into the film, during nucleation and growth, can adversely affect the film properties. The filtering of such microparticles, and neutral atoms, is achieved by a combination of mechanical and electromagnetic deflection, such that there is no 'line of sight' from the cathode to the substrate on which the film is deposited [25].

### 2.5.2 Properties of FCVA films (a-C and a-C:H)

With this FCVA (as opposed to PECVD) technique there is a greater degree of control over incident ion energy and species.  $\text{C}^+$  ions (for a-C, or  $\text{C}_2\text{H}_2^+$  for a-C:H) can be predominant, but there may still be some larger ("micro") particles incident [25, 27]. At low energies the ions are unable to penetrate beneath the surface of the film and this results in a film with a high  $\text{sp}^2$  content, which is the stable carbon configuration under normal temperature and pressure conditions. The optimum ion energy for  $\text{sp}^3$  formation is  $\approx 100 \text{ eV}$ ; the ions can then embed into the sample in a shallow

implantation process (“subplantation”), filling interstitial sites and producing a densified  $sp^3$  bonded network. Such a-C(:H) with a particularly high proportion of tetrahedrally bonded  $sp^3$  carbon sites (~80%) is often referred to as tetrahedral amorphous (hydrogenated) carbon ta-C(:H). At higher energies the implanting ions penetrate the sample, but create so-called ‘thermal spikes’, where all the ion energy is deposited in a very small volume. These highly excited regions allow thermal migration and may remove some of the densification (stress) allowing relaxation to the  $sp^2$  form [14, 27, 28]. The variation of film attributes with energy of carbon atom is summarised in figure 2.6 [27].

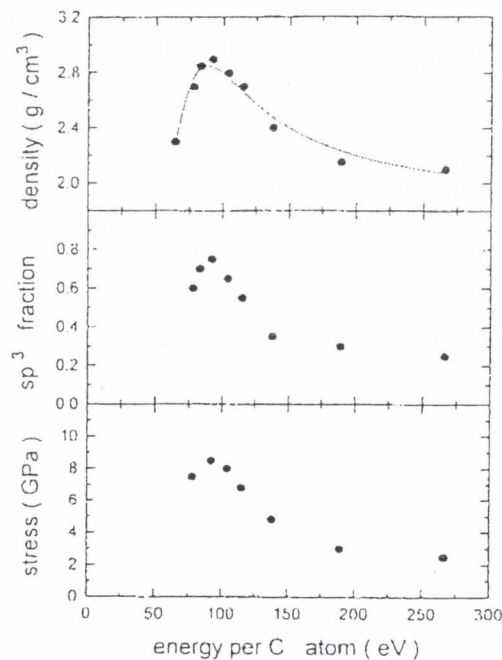


**Figure 2.6** Variation of FCVA film properties as a function of energy per carbon atom

This analysis of the effect on film structure of increasing ion energy can, of course, also be applied to the PECVD a-C:H films discussed in a previous section, the ion energy in these cases being determined by the self-bias voltage [18, 28].

## 2.6 References

- [1] J. Robertson *Phil. Mag. B* 76(1997)335
- [2] S.R.P. Silva, J. Robertson, Rusli, G.A.J. Amaratunga *Phil. Mag. B* 74(1996)369
- [3] J. Robertson *Adv. Phys.* 35(1986)317
- [4] J.B. Russell "General Chemistry" (Intl. Edn.) McGraw-Hill, Auckland (1981) p.598
- [5] B. Dischler, G. Brandt *Industrial Diamond Rev.* 3(1985)131
- [6] A.W. Moore "Physics and Chemistry of Carbon" ed. P.L. Walker, Dekker, New York(1973)
- [7] J. Fink, T. Muller-Heinzerling, J. Pfluger, B. Scheerer, B. Dischler, P. Koidl, A. Bubenzer, R.E. Sah *Phys. Rev. B* 30(1983)4713
- [8] S. Kaplan, F. Jansen, M. Machonkin *Appl. Phys. Lett.* 47(1985)750
- [9] C. Weissmantel *Thin Solid Films* 92(1982)55
- [10] W. Jacob, W. Moller *Appl. Phys. Lett.* 63(1993)1771
- [11] G.A.J. Amaratunga, M. Chhowalla, D.A.I. Munindradasa, K.G. Lim, C.J. Kiely, I. Alexandrou in "Amorphous Carbon: State of the Art" S.R.P. Silva, J. Robertson, W.I. Milne and G.A.J. Amaratunga (Eds.) pub. World Scientific (Singapore) (1998) p.311
- [12] J. Robertson, E.P. O'Reilly *Phys. Rev. B* 35(1987)2946
- [13] J. Robertson *J. Non-Cryst. Solids* 198-200(1996)615
- [14] R.C. Barklie, M. Collins, S.R.P. Silva *Phys. Rev. B* 61 (2000) 3546
- [15] B.J. Jones, R.C. Barklie, R.U.A. Khan, J.D. Carey, S.R.P. Silva *Diamond Relat. Mater.* 10(2001)993

- [16] M. Collins, R.C. Barklie, J.V. Anguita, J.D. Carey, S.R.P Silva *Diamond Relat. Mater.* 9(2000)781
- [17] A. Sadki, Y. Bounouh, M.L. Theye, J. von Bardeleben, J. Cernogora, J. L. Fave *Diamond Relat. Mater.* 5(1996)439
- [18] A. Bubenzer, B. Dischler, G. Brandt, P. Koidl *J. Appl. Phys.* 54(1983)4590
- [19] S. N. Dub, N. V. Novikov, M. A. Voronkin, I. N. Lupich, V. G. Malogolovets, B. A. Maslyuk and G. A. Podzyarey *Diamond Relat. Mater* 6(1997)574
- [20] J. Robertson in "*Amorphous Carbon: State of the Art*" as ref [11] p.32
- [21] C. Godet, N.M.J. Conway, J.E. Bouree, K. Bouamra, A. Grosman, C. Ortega, *J. Appl. Phys.* 91(2002)4154
- [22] T. Lagarde, J. Pelletier, *Proc. 11th Intl. Colloq. on Plasma Processes* (1997) p.13
- [23] P. Bulkin, N. Bertrand, B. Drévilion *Thin Solid Films* 296(1997)66
- [24] F. Piazza, Y. Arnal, D. Grambole, F. Herrmann, M. Kildemo, A. Lacoste, G. Relihan, A. Golanski *Thin Solid Films* 383(2001)196
- [25] B.F. Coll, J. Jaskie, J. Markhan, E. Menu, A. Talin in "*Amorphous Carbon: State of the Art*" as ref [11] p.91
- [26] G. Fanchini, A. Tagliaferro, D. Dasgupta, E. Laurenti, A.C. Ferrari, K.B.K. Teo, W.I. Milne, J. Robertson *J. Non-Cryst. Solids* 299-302(2002)840
- [27] M. Weiler, S. Sattel, T. Giessen, K. Jung, H. Ehrhardt *Phys. Rev. B.* 53(1996)1594
- [28] Y. Lifshitz in "*Amorphous Carbon: State of the Art*" as ref. [11] p.14

## *Chapter 3*

# *Electron Paramagnetic Resonance*

Milton, madam, was a genius that could  
cut a colossus from a rock; but could not  
carve heads upon cherry stones

Samuel Johnson

## 3. Electron Paramagnetic Resonance (EPR)

### 3.1 Basic Principles

When a molecule containing magnetic dipoles is irradiated over a wide range of spectral frequencies there would normally be no absorption attributable to magnetic interactions. If, however, the sample of interest is placed in a static magnetic field absorption due to magnetic dipole transitions may occur at one or more characteristic frequencies [figure 3.1 shows a schematic for the  $S = \frac{1}{2}$  case].

Monochromatic radiation falls on the sample, within a resonant cavity, and variations in the intensity of the transmitted (or reflected) radiation can be observed by means of an appropriate detector. Absorption will occur when the energy of a quantum of incident radiation,  $h\nu$ , matches the energy-level separation,  $g\mu_B B$ , where  $g$  is the Landé  $g$ -factor and  $\mu_B$  is the Bohr magneton. The requirement of a static magnetic field,  $B$ , is the unique aspect of magnetic dipole transitions; in the absence of the field the energy levels are coincident (degenerate). Magnetic dipoles arise from net electronic or nuclear angular momentum. The fundamental phenomenon to be understood is thus the quantization of angular momentum.

It is, in fact, more practical to use a fixed microwave radiation frequency (supplied, for example, by a klystron) and vary the magnetic field (by varying the current in the electromagnet), thus achieving absorption when the energy level separation matches the (fixed) energy of a quantum of radiation.

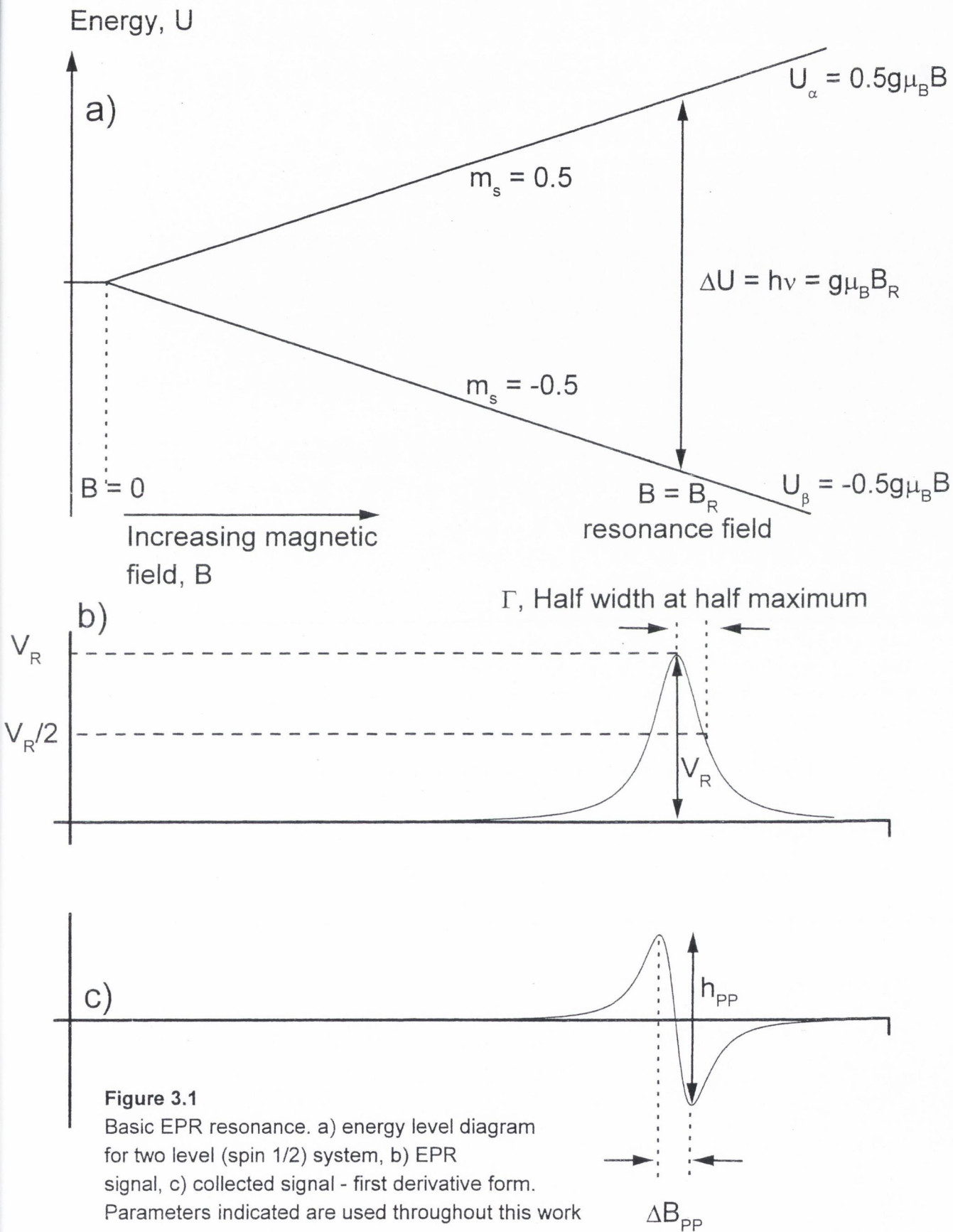


**Figure 3.1**  
 Basic EPR resonance. a) energy level diagram for two level (spin 1/2) system, b) EPR signal, c) collected signal - first derivative form. Parameters indicated are used throughout this work

In addition a sinusoidal modulation field,  $\mathbf{B}_m = B_m \cos \omega_m t$ , is applied (using coils just outside the cavity) and this enables the signal to be collected in first derivative form and processed with a lock-in amplifier, thus improving the signal-to-noise ratio of the scans. To avoid distortion of the spectrum the modulation amplitude must be kept to less than or equal to about one fifth of the peak-to-peak linewidth. A typical experimental set-up is shown in figure 3.2.

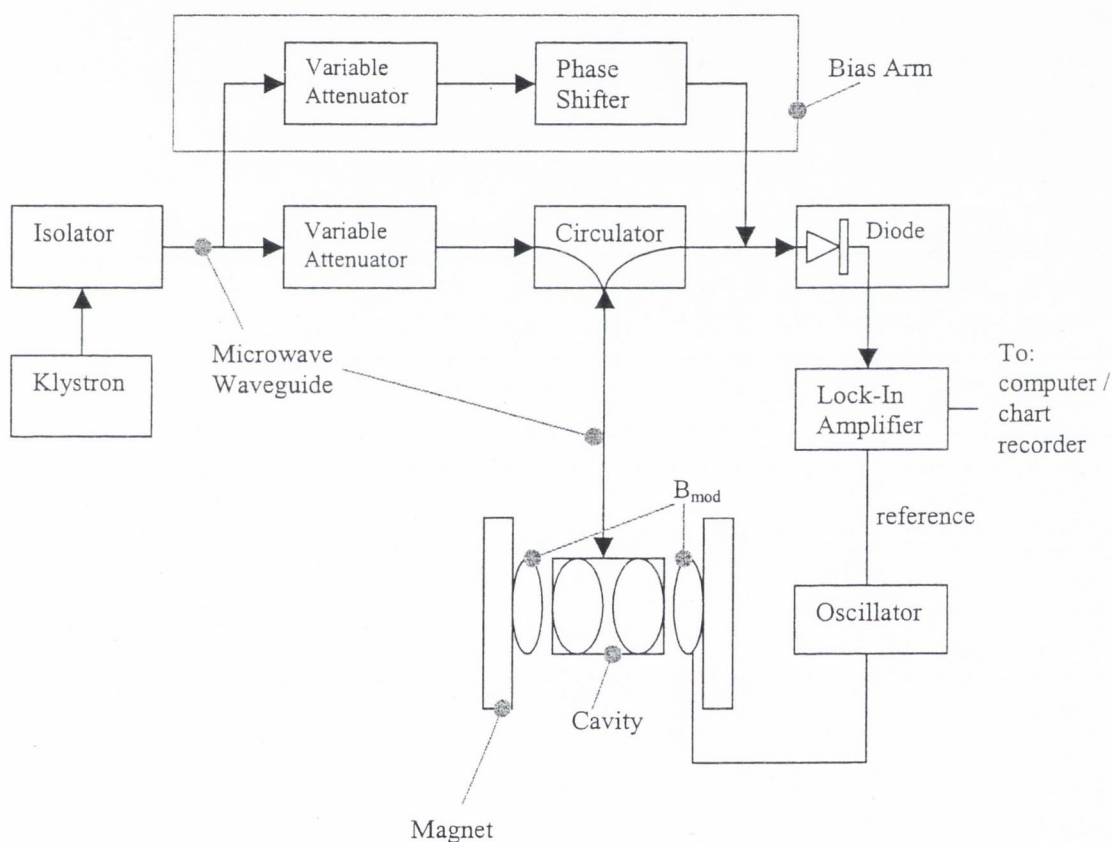


**Figure 3.2.** Block diagram of a basic EPR system

In our X-band set-up, the microwave frequency,  $\nu_K$  ( $\approx 9.5\text{GHz}$ ), must be tuned to the resonant frequency of the cavity,  $\nu_{Mode}$ , before any measurements can be made (only

at this frequency is the cavity an ideal absorber) [1]. As the frequency of the microwaves emitted by the klystron,  $\nu_K$ , has a tendency to drift and the resonant frequency of the cavity,  $\nu_{\text{Mode}}$ , may vary slightly, Automatic Frequency Control (AFC) is used to keep  $\nu_K$  equal to  $\nu_{\text{Mode}}$ . The cavity used for EPR in this work operates in  $\text{TM}_{110}$  mode, with a  $\text{TE}_{012}$  mode cavity used for low temperature work.

The detector diode functions best (i.e. is at its most sensitive) with a finite current (of about  $150\mu\text{A}$ ) flowing through it. At sufficiently high powers this 'bias current' can be taken from the microwaves reflected from the cavity with no microwave power drawn through the bias arm ("Simple Homodyne EPR"). In some cases it may be necessary or desirable to use the *bias arm* to bring the current in the diode to  $150\mu\text{A}$ . In this case it is desirable to *critically couple* the cavity, i.e. at non-resonant fields negligible microwave radiation is reflected from the cavity to the detector diode. The variable attenuator and phase shifter in the bias arm are then adjusted to bias the diode to the correct voltage. This method of operation is "Homodyne EPR (with reference arm)" [1] the side arm essentially allows low power measurements to be made, where otherwise a non-negligible proportion of microwave power incident on the cavity would be needed to be reflected to bias the diode detector.

## 3.2 g-values and spin density

In principle, if the microwave frequency is known, it is possible to calculate the g-value of a sample resonance by the nominal position of resonance in magnetic field (The peak of the resonance becomes the zero-crossing point in the 1st derivative collection). The following equation is used:

$$3.1 \quad h\nu = \Delta E = g\mu_B B$$

However, it is more accurate to compare the position of the resonance of the sample with that of a sample of a known g-value. A sample of MgO containing  $F^+$  centres is used for this, which is, in essence, a calibration of the field. The field range is calibrated using a proton NMR probe, again giving absolute values of field.

The number of spins contributing to the EPR signal,  $N$ , is proportional to the area under the resonance line. An absolute value of spin concentration can therefore be obtained by comparing the double integral of the collected (1st derivative) signal with that of a sample of known number of spins, such as Varian pitch in KCl.

Alternatively, if the shape of the resonance line can be determined, the following approximation using the peak-to-peak linewidth,  $\Delta B_{pp}$ , of the derivative and a shape dependent factor,  $\kappa$  can be used, and compared with the standard.

$$3.2 \quad N \propto \kappa \Delta B_{pp}^2 h_{pp}$$

where  $h_{pp}$  is the peak-to-peak height of the collected 1st derivative signal and  $\kappa$  is 1.815 for a Lorentzian lineshape, 0.515 for a Gaussian and 2.76 for the Pitch in KCl calibration sample.

The absolute spin populations (and average spin densities) are estimated to be correct to within a factor of 2, but their relative values are correct to within approximately  $\pm 15\%$ , dependent on the signal-to-noise ratio of the spectra.

As well as gain settings etc., a number of other factors need to be taken into account when analysing spectra. The sensitivity of the cavity, as indicated by the Q-value, which can be defined as [2]:

$$3.3 \quad Q = \frac{2\pi (\text{maximum microwave energy stored in resonator})}{\text{energy lost per cycle}}$$

also affects the detected signal. The Q-value is not a constant and may be affected by the sample within the cavity. A ratio of the strength of signal,  $h_{pp}$ , of a calibration sample (assumed not to change the Q of the cavity) with and without the sample to be experimented on present, gives an indication of the effect of the presence of the sample on the Q-value.

In addition, the microwave field and modulation field are not constant over the entirety of a finite sample. For small films and suchlike, this effect can be ignored, as the sample is inserted to the centre of the cavity where the conditions are fairly uniform. However, in the case of, for example, a powder sample traversing the entire length of the cavity (or a good proportion thereof) this non-uniformity can reduce the

apparent signal strength. For these types of samples the value recorded needs to be adjusted to give a true value of signal strength. [3]

### 3.3 Simple Models of Lineshape

In addition to the spin population and g-value of the resonance line, the width and shape of the signal can also give information about the nature of defects and exchange interactions within the film.

#### 3.3.1 Relaxation time, $T_1$ , Transition Probability

##### Derivation.

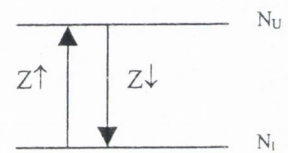


**Figure 3.3** Two level transitions

Consider a simple two-level model, as shown in figure 3.3.

Suppose that  $Z_{\downarrow}$ ,  $Z_{\uparrow}$  are transition probabilities per unit time from upper to lower, and lower to upper levels, respectively, and that  $N$  are population densities of upper and lower levels as denoted by subscript.

The difference in population of the levels is  $\Delta N = N_l - N_u$ . Each transition changes  $\Delta N$  by 2 therefore:

$$d\Delta N/dt = -2N_l Z_{\uparrow} + 2N_u Z_{\downarrow}$$

By looking at the steady state solution,  $\Delta N^{ss}$ , we can show [4] that:

$$d\Delta N/dt = (\Delta N^{ss} - \Delta N) \cdot (Z_{\downarrow} + Z_{\uparrow})$$

$(Z\downarrow + Z\uparrow)^{-1}$  has units of time and is, by definition, a relaxation time. Remembering that the magnetization in the z-direction,  $M_z$  is proportional to  $\Delta N$ ,

$$dM_z/dt = (M_z^0 - M_z)/T_1$$

thus defining the “spin-lattice relaxation time”,  $T_1$ , as indicative of lifetime broadening. In our simple model, the uncertainty relation can be used to give an indication of the linewidth.

### 3.3.2 Contributions to Transition Probabilities, Mechanisms for $T_1$

Utilizing Einstein’s A and B coefficient formalism, where A and B are the spontaneous and stimulated emission coefficients respectively, we obtain for  $Z\downarrow, Z\uparrow$ :

$$Z\uparrow = B \rho + W\uparrow$$

$$Z\downarrow = A + B \rho + W\downarrow$$

where W are the probabilities for transitions induced by the surroundings, e.g. the lattice.  $\rho$  is the time averaged radiation density (related to  $B_1$  - see later). Thus:

$$T_1 = (A + 2 B \rho + W\uparrow + W\downarrow)^{-1}$$

$(T_1)^{-1}$  can be thought of as a sum  $\sum_i (T_{1i})^{-1}$  over distinct relaxation times. The  $W\downarrow$ ,  $W\uparrow$  terms dominate over the A ( $T_{1A} \sim 10^4$  years) and B ( $10^3$  yrs) terms. Therefore  $T_1$  can accurately be described as the *Spin-Lattice Relaxation Time* [4].

The simple model also enables us to understand saturation. As the microwave power is increased the  $\rho$  term dominates in  $Z\downarrow$  and  $Z\uparrow \Rightarrow Z\uparrow = Z\downarrow \Rightarrow \Delta N \rightarrow \Delta N^{ss} \rightarrow 0$  i.e. there is no net absorption of radiation by spins and the EPR signal disappears. This “Power Saturation” shows the necessity of having adequate spin relaxation time and only applying a moderate  $B_1$  (Amplitude of fluctuating microwave field, perpendicular to applied (swept) field). Only at well below saturation can the approximation  $Z=W$  be made, this (in essence) allows the calculation of the relaxation times, see later sections.

The transitions between the spin levels can be stimulated by fluctuations in the local magnetic field arising from motion of the spin-bearing molecule or the surrounding matter. These fluctuations have a range of frequencies (i.e. a spectral density) but only fluctuations with  $\nu = \nu_{EPR}$  will flip the spins.

### 3.3.3 Spin Temperature

A useful concept is the ‘spin temperature’,  $T_s$ , which can be defined by the following expression, from Maxwell-Boltzmann statistics:

$$N_u/N_l = \exp(-\Delta U/k_B T_s)$$

The simple two level system, at a given temperature in thermal equilibrium, will have a ratio of population of the upper and lower spin states in accordance with Maxwell Boltzman statistics. As radiation at the correct frequency  $\nu_{\text{EPR}}$  is added to the system, flipping spins increases  $N_u/N_l \Rightarrow T_s$  increases and the system is 'hotter'. With no relaxation mechanism, the system would tend towards a state where the two levels were equally populated. However, the system relaxes by giving up "heat" to its surroundings via the lattice (i.e. the spins fall back to the lower energy level), the time taken for this process can be characterized by the spin-lattice relaxation time,  $T_1$  [4].

### 3.3.4 Bloch Model

The Bloch model simplifies the characterization of the complex relaxation process into two empirical parameters,  $T_1$  and  $T_2$ . This is not rigorously valid and fails to be exact, especially in solids. It does, however, provide a convenient way of visualizing the processes involved and can be altered for more complex situations.

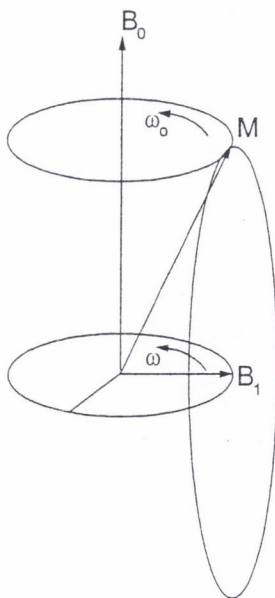


**Figure 3.4** Interactions between the microwave field,  $B_1$  and magnetic moment,  $M$ , occur when  $\omega = \omega_0$

In a classical model, the magnetization vector precesses around the applied field  $B_0$ , at the Larmor frequency,  $\omega_0$  (see figure 3.4). The basic equation is:

$$\frac{\partial \mathbf{M}}{\partial t} = \gamma \mathbf{M} \times \mathbf{B}$$

$$\frac{\partial \mathbf{M}}{\partial t} = \gamma \mathbf{M} \times \mathbf{B}$$

with an applied field  $B_0$  in the Z direction and assuming  $\gamma$  to be isotropic. We also make use of the phenomenological formulae :

$$\partial M_{x,y}/\partial t = -M_{x,y}/T_2$$

$$\partial M_z/\partial t = -(M_z - M_z^0)/T_1$$

The microwave field,  $\mathbf{B}_1 = B_1 \cos \omega t$ , is applied perpendicular to  $B_0$ . Only when  $B_1$  is stationary in the rotating frame, i.e. precessing around  $B_0$  at frequency  $\omega_0$ , will it cause the magnetic moment to be flipped from parallel to anti-parallel, and vice versa [2].

By analyzing the magnetization in the rotating frame we can obtain the following expressions [5] for the magnetization and the susceptibility,  $\chi$ , (where  $\mathbf{M} = \chi \mathbf{H}$  and  $\chi = \chi' + i\chi''$ ):

$$M_z^0 = \chi^0 B / \mu_r \mu_0$$

$$\chi' = \chi^0 \omega_0 (\omega_0 - \omega) T_2^2 / [1 + (\omega_0 - \omega) T_2^2 + \gamma^2 B_1^2 T_1 T_2]$$

$$\chi'' = \chi^0 \omega_0 T_2 / [1 + (\omega_0 - \omega) T_2^2 + \gamma^2 B_1^2 T_1 T_2]$$

$$\chi'' = \chi' / (\omega_0 - \omega) T_2$$

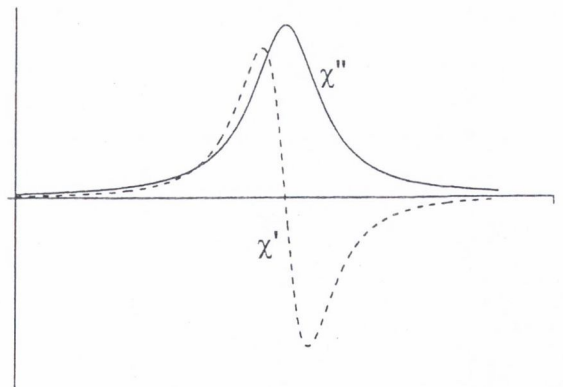


**Figure 3.5** Absorption and dispersion

where  $\chi^0$  is the static magnetic susceptibility,  $\omega_0$  is the Larmor frequency,  $\omega$  is frequency of  $B_1$  and the other symbols have their usual meanings.

$\chi'$  and  $\chi''$  respectively represent dispersion and power absorption,  $P_a$ , of the EPR transition, and are sketched in figure 3.5.

It has been shown [6] that power absorption is given by the following equation:

$$3.4 \quad P_a = \omega \chi'' B_1^2 / \mu_0 \Rightarrow P_a = (\pi / \mu_0) (B_1^2 (1 + \gamma^2 B_1^2 T_1 T_2)^{-5}) \omega B_r \chi^0 L(\omega - \omega_0)$$

where  $B_r$  is the field at which resonance occurs and  $L$  is the normalized Lorentzian function dependent on experimental conditions. Looking at field sweep conditions (as opposed to microwave sweep),  $L(B - B_r)$  is a Lorentzian with half width at half maximum (HWHM) given by the expression:

$$3.5 \quad \Gamma = (1/|\gamma|T_2)(1 + \gamma^2 B_1^2 T_1 T_2)^{0.5}$$

For non-saturating conditions  $B_1^2$  is neglected and  $\Gamma = (1/|\gamma|T_2)$ . These two expressions enable the relaxation times  $T_1$  and  $T_2$  to be calculated from experimental spectra, as explained in section 3.5, for both this simple case and for more complex lineshapes.

Appendix A shows that  $\chi_0$  is proportional to the area under the EPR signal (i.e. the double integral of the first derivative) and inversely proportional to the volume of the sample, and so can be calculated by comparison to the Pitch in KCl standard.

### 3.4 High Frequency measurements, Dispersion

For some experiments it is preferable to use a higher frequency than is obtainable with our X-band ( $\approx 9.5\text{GHz}$ ) set-up. EPR at W-band ( $\approx 94\text{GHz}$ ) was carried out at St. Andrew's University. The apparatus is described in detail elsewhere [7] and a schematic [8] is shown in figure 3.6.

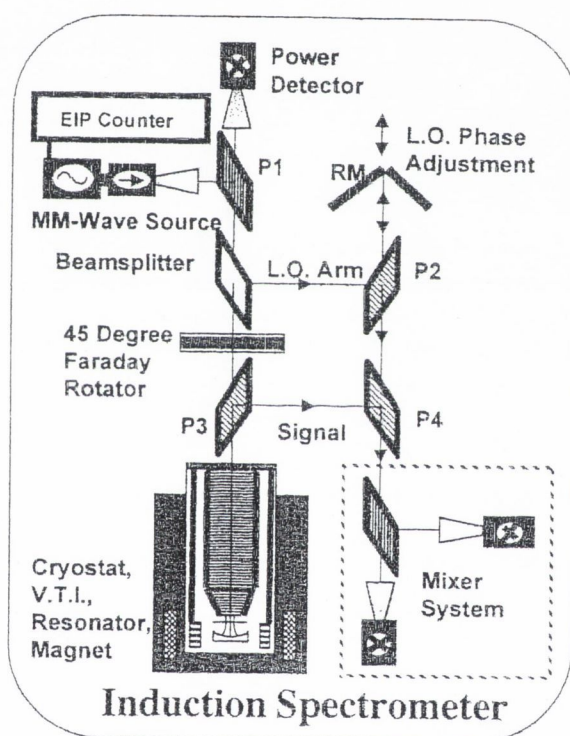


Figure 3.6 Schematic set-up of W-band EPR spectrometer

With this apparatus the sample is not placed in a cavity, in contrast to X-band, but mounted in a non-resonant 'bucket' style holder, such that the magnetic field of the superconductor solenoid magnet is perpendicular to the carbon film. The spectrometer uses quasi-optical techniques to implement a broadband homodyne bridge and the microwave frequency is fixed to an external reference source, rather

than locked to a cavity mode. Therefore, instead of the pure absorption, and thus simple line-shape, observed at 9.4GHz the spectra obtained are usually a mixture of dispersion and absorption. The phase shifter shown in the schematic of the W-band set-up (figure 3.6) [8] allows adjustments to be made until a pure absorption spectrum is obtained. However, most spectra are collected with some degree of dispersion, and in order to usefully compare these spectra, we need to include this in the equations.

Schumacher [5] shows that the EPR signal is given by:

$$3.6 \quad Y = A(\chi'' \cos \theta - \chi' \sin \theta) \quad \text{where } \theta \text{ is the phase shift}$$

Writing in terms of magnetic field, then,

$$x = \frac{B - B_0}{\Gamma} \quad \text{where the resonance at field } B_0 \text{ has a half width at half maximum}$$

of  $\Gamma$ .

$$\chi' = \alpha \frac{x}{1 + x^2}$$

$$\chi'' = \alpha \frac{1}{1 + x^2}$$

The EPR signal is then [2,5]:

$$3.7 \quad Y = \beta \left( \frac{1}{1 + x^2} \cos \theta - \frac{x}{1 + x^2} \sin \theta \right) \quad \text{where } \alpha \text{ and } \beta \text{ are scaling terms}$$

However, the signal is collected in first derivative form, therefore the expression to fit to the experimental spectrum is:

$$3.8 \quad \beta \left( \frac{-2x}{1+x^2} \cos \theta + \left[ \frac{2x^2}{(1+x^2)^2} - \frac{1}{1+x^2} \right] \sin \theta \right)$$

thus obtaining values for linewidth, resonance position (and hence  $g$ -value) as well as degree of dispersion in the spectra. A number of spectra with different degrees of dispersion, and their fits, are shown in figure 3.7.

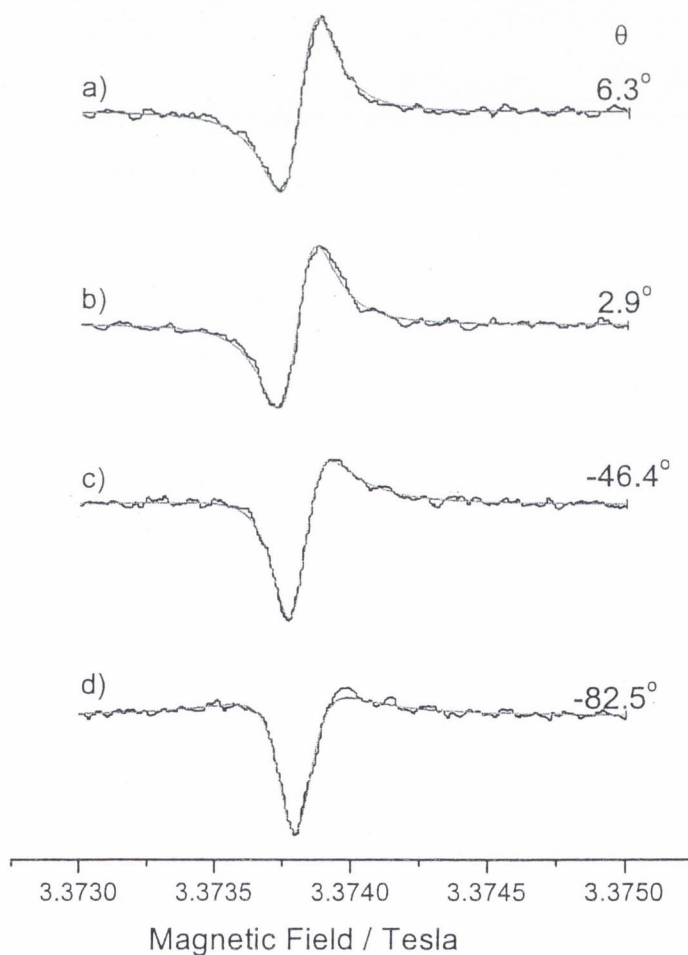


**Figure 3.7** Variation of signal shape with various degrees of dispersion, characterised by the phase angle,  $\theta$ , between almost pure absorption (b) and almost pure dispersion (d), with fits shown as smooth solid lines.

## 3.5 Line broadening mechanisms

### 3.5.1 Homogeneous Broadening

Homogeneous broadening occurs when all of a set of spins has the same spin Hamiltonian parameters and experience the same net magnetic field (i.e. local fields must give the same time averaged field over a sufficiently short period of time). This means that the lineshape (i.e. transition probability as a function of magnetic field) is the same for each dipole. This generally gives rise to an absorption lineshape with linewidth (HWHM),  $\Gamma$ , given by the Bloch equations, defining an effective spin-spin relaxation time,  $T_2$ , a measure of the interaction between spins:

$$3.9 \quad T_2 = |\kappa\gamma\Gamma|^{-1}$$

$$\begin{aligned} \kappa &= 1 \text{ for Lorentzian lines} \\ \kappa &= \sqrt{\pi \ln 2} \text{ for Gaussian lines.} \end{aligned}$$

Processes leading to homogeneous broadening include [4,6]:

- *Magnetic dipole coupling between like spins.* The mutual spin flips of paired spins cause no change in the energy of the system, but do affect the lifetime ( $T_1$ ) of each spin. The propagation of magnetization through the lattice via such flips is called spin diffusion.  $T_2$  is a measure of this rate.
- *Gaseous phase collisions* can cause the system to tend towards equilibrium.  $T_2 = T_1 =$  mean time between collisions.
- *Spin lattice relaxation*
- Interaction with *homogeneous magnetic field*

- Motion of carriers in a *microwave field*
- *Diffusion of excitation* through sample
- *Motional narrowing* from fluctuations in local field.

These mechanisms are discussed in greater detail elsewhere in this work.

### 3.5.2 Inhomogeneous Broadening

Generally the unpaired electrons in a sample are not all subject to the same B field. Therefore at any one time only a small fraction of the spins is in resonance. As the external field is swept through the 'line' the observed shape is then a superposition of a large number of components (spin packets) each slightly shifted relative to the others. This results in a Gaussian lineshape as an envelope to the spin packet lines (see figure 3.8) [4,6].

It is possible to choose the amplitude of the microwave field,  $B_1$ , to saturate a particular portion of the line, decreasing its intensity ('hole burning'). Thus the process of changing the microwave power,  $P$ , will change the lineshape of the resonance, allowing detection of inhomogeneous broadening.

The inverse width of an inhomogeneously broadened line must not be associated with any actual relaxation time. The inverse width of each component in the line, or of any homogeneously broadened line, is a measure of  $T_2$  for that line or component. Thus  $T_2$  is a measure of the spin-packet width.

Causes of inhomogeneous broadening include [4,6]:

- *Inhomogeneous external magnetic field*
- *Unresolved hyperfine structure* (this may be resolvable using ENDOR)
- *Anisotropic interactions in randomly orientated systems.* Anisotropic g-values or hyperfine interactions imply inhomogeneity and possibly asymmetric line shape
- *Dipolar interactions with other paramagnetic centres* (including spins of differing Larmor frequencies) imposing a random local field.

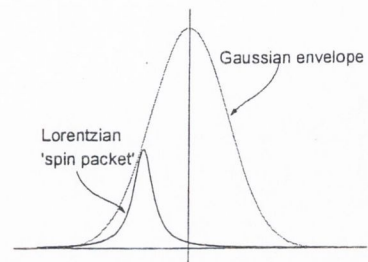


**Figure 3.8.** Inhomogeneous lines

Inhomogeneous broadening must come from interactions outside the spin system and must be slowly varying over the time required for a spin transition.

### 3.6 Motional Narrowing

In a time period of order  $T_2$  (or even, in some cases, the Larmor period) the resonant spins can move a substantial distance relative to their initial spacing. Therefore local fields are *time dependent*, most often in a random way.

Consider one radical: the internal fields caused by other radicals or paramagnetic centres are random in orientation and time dependent in the rotating ( $\omega_0$ ) frame. The z components of the local dipole fields add to or subtract from  $H_0$ , causing a precession around the z-axis more rapid or less rapid than  $\omega_0$ . In the rotating frame these components are the only cause of precession around the z-axis. These local fields contribute to a  $T_2$  process (transverse relaxation).

$T_1$  processes, involving the precession of spin away from z-axis, are caused by transverse fields that are static in the rotating frame; therefore local fields with transverse components, and frequency components at the Larmor frequency contribute to  $T_1$  [2,4,5].

In order to examine these processes further we make some simplifying assumptions. Assume each spin sees a constant local field,  $h_L \ll H_0$ , in z- direction for a period of time  $\tau_c$  (the *correlation time*) after which time it may, or may not, reverse itself (with equal probability). Applying this 'random walk' assumption to precession around z-axis: the amount of precession after  $\tau_c$  is  $\gamma h_L \tau_c$ , after a time t the number of steps,  $n=t/\tau_c$ . This implies that the mean square phase accumulated is:

$$\langle \phi(t)^2 \rangle = (t/\tau_c)(\gamma h_L \tau_c)^2 = \gamma^2 h_L^2 \tau_c t$$

If  $T_2'$  is the time for  $\langle \phi(t)^2 \rangle = 1$  then:

$$1/T_2' = (\delta\omega)^2 \tau_c \quad \text{where } \delta\omega = \gamma h_L$$

( $T_2'$  is introduced to show that we may not have included all the causes of  $T_2$  in our calculation.)

The above equation is a reasonable estimate of  $T_2$  (and line width as given by  $\Gamma = 1/|\gamma|T_2$ ), as long as  $\delta\omega\tau_c < 1$ . If  $\tau_c$  is long then  $\delta\omega/\gamma = h_L$  is itself the linewidth of the resonance line. The above argument shows that *in the presence of a changing local environment the line width is narrower than the static linewidth*  $\delta\omega$ , as long as local environment changes rapidly compared to  $1/\delta\omega$ . [5]

Generalizing to the random case [5]:

$$1/T_2 = \gamma^2 [\langle h_z^2 \rangle \tau_c + \langle h_y^2 \rangle \tau_c / (1 + \omega_B^2 \tau_c^2)]$$

$$1/T_1 = 2\gamma^2 h_L^2 \tau_c / (1 + \omega_B^2 \tau_c^2)$$

For the totally isotropic case  $\langle h_x^2 \rangle = \langle h_y^2 \rangle = \langle h_z^2 \rangle = \langle h_L^2 \rangle$

Note that these equations do not describe the breakdown of  $T_2$  to constancy as  $\tau_c$  becomes greater than  $1/\delta\omega$ , as shown in figure 3.9. In this case the local field is essentially static and the theory breaks down.

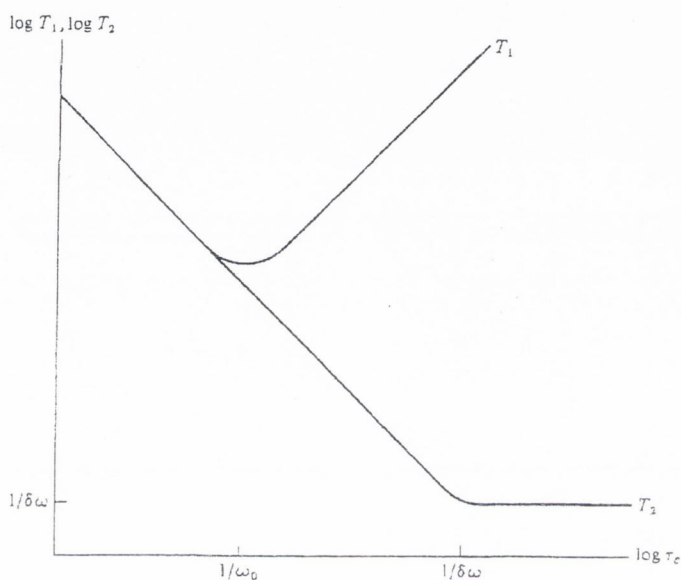


**Figure 3.9** Spin-lattice ( $T_1$ ) and spin-spin ( $T_2$ ) relaxation times as a function of correlation time,  $\tau_c$  [5].

There are many examples of motional narrowing (due to for example, hyperfine structure, movement of radicals, movement of surroundings) they can all be treated in a similar way to that for exchange narrowing, below. A simple case for hyperfine structure is dealt with in [4].

### 3.6.1 Exchange Narrowing

Consider two types of ions (for example) that give rise to two different  $g$ -values. An exchange interaction exists of the form  $\hbar J \mathbf{S}_1 \cdot \mathbf{S}_2$ , where  $J$  is the exchange constant in units of frequency, and other symbols have their usual meanings. The constant,  $J$ , is

taken to be the rate at which the resonant spin on sites one and two exchange, so that the electron spins precess at frequency  $g_1\mu_B H_0/\hbar$  for a time, then at frequency  $g_2\mu_B H_0/\hbar$ . If the rate of exchange is faster than  $|g_1-g_2|\mu_B H_0/\hbar$  then the modulation index is less than one, and the line is exchange narrowed (see figure 3.10 below).

These expressions are an approximation of the quantum mechanical ratio of the energy difference between states (diagonal elements) and the magnitude of the off-diagonal elements; a rigorous derivation is given in [9]. The transition to exchange narrowed lines is analogous to the Zeeman Effect  $\rightarrow$  Paschen Back Effect in atomic physics.

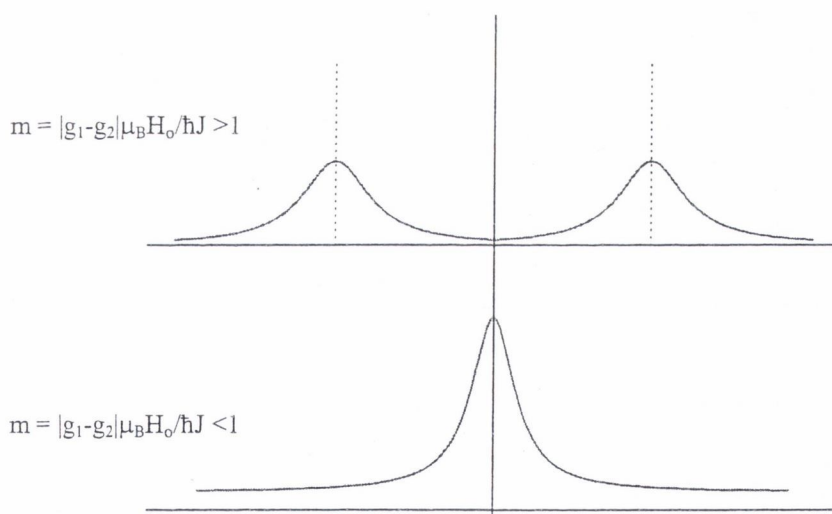


**Figure 3.10** Schematic showing exchange narrowing of an EPR line

## 3.7 Calculation of Relaxation Times from Spectra

### 3.7.1 Simple lines

For a single (homogeneous) line of either Lorentzian or Gaussian form the transverse relaxation time  $T_2$  can be calculated from the non-saturated linewidth, from the relation

$$3.9 \quad T_2 = |\kappa\gamma\Gamma|^{-1}$$

where  $\Gamma$  is calculated from  $\Delta B_{pp}$  with the simple relation  $\Gamma = \frac{2}{\sqrt{3}} \Delta B_{pp}$  [4] with the

shape of the line giving the value of  $\kappa$ , as before.

An expression for the peak-to-peak first derivative amplitude, assuming a fixed operational temperature, is:

$$3.10 \quad h_{pp} = \frac{3\sqrt{3}}{4\pi} \cdot \frac{\gamma B_1 T_2}{(1 + \gamma^2 B_1^2 T_1 T_2)^{3/2}}$$

$T_1 T_2$  (and therefore  $T_1$ ) is calculated by fitting this equation to a plot of peak-to-peak signal height versus  $B_1$  field. Such a saturation curve is linear at low microwave power but also shows the deviation from linearity as the power increase to saturate the resonance. Measurement of the linewidth (for calculation of  $T_2$ ) must be made on spectra taken at power low enough for the resonance to lie in the unsaturated, linear region. In practice, the  $B_1$  field is calibrated by recording an additional saturation curve, using a sample of  $\alpha$ - $\alpha$ -diphenyl- $\beta$ -picryl-hydrazyl (DPPH) with known

relaxation times ( $T_1=T_2=6.25 \times 10^{-8}$ s, measured in the temperature range 77-700K) [10, 11].

### 3.7.2 Voigt shape lines

Inhomogeneous lines, with a Voigt shape (i.e. a convolution of Lorentzian and Gaussian components), present a more complex problem. The spin-spin relaxation time,  $T_2$ , depends on the Lorentzian component,  $\Gamma_L$ , of the linewidth (i.e. the spin packet width of earlier in this chapter). Thus a Voigt shape must be generated and fitted to the non-saturated experimental spectrum, to obtain a value for  $\Gamma_L$  and thus  $T_2$  from:

$$T_2 = 1/\gamma\Gamma_L$$

Zamarano-Ulloa *et al.* [12] show that the spin-lattice relaxation time for inhomogeneously broadened lines can be found from the following equation

$$T_1 = \frac{1}{T_2 \gamma^2 H_{1\text{MAX}}^2} f(a)$$

where  $H_{1\text{MAX}}$  is the microwave field at which the height,  $V_R$ , of the integral of the collected signal is at a maximum (i.e. the height of the EPR resonance is at a maximum, as the signal is collected in first derivative form). 'a' is the ratio of the

Lorentzian to Gaussian component linewidths,  $\Gamma_L/\Gamma_G$ , and  $f(a)$  is a defined function,

an approximation of this is:

$$f(a) = \frac{3 + \sqrt{9 - 8a^2 + 16a^4}}{4a^2}$$

though a full definition is given in the paper [12] and used in calculations. This process for  $T_1T_2$  determination, however, relies on a best fit of the lineshape, which is often subjective, and uses a single point from the saturation curve. This produces large uncertainties (>60% for  $T_1$ ) in the calculated relaxation times.

The relaxation time values can be refined, however, using Castner's [13] equation for signal height,  $V_R$ , as a function of  $H_1$ ,  $T_1$  and  $T_2$ :

$$V_R = \frac{H_1 b}{\sqrt{1 + H_1^2 b^2}} \exp(a^2 H_1^2 b^2) \frac{1 - 2\pi \int_0^{a\sqrt{1+H_1^2 b^2}} e^{-y^2} dy}{1 - 2\pi \int_0^a e^{-y^2} dy}$$

where  $b = \gamma\sqrt{(T_1 T_2)}$  and, as before,  $a = \Gamma_L/\Gamma_G$ .

The integrals are error functions, and are evaluated in tables. Therefore, substituting values for  $T_1T_2$  and 'a' previously found into:

$$V_R = \frac{H_1 b}{\sqrt{1 + H_1^2 b^2}} \exp(a^2 H_1^2 b^2) \frac{1 - \text{erf}(a\sqrt{1 + H_1^2 b^2})}{1 - \text{erf}(a)}$$

gives a fit for the whole saturation curve, not based solely on the point at which the signal is at a maximum. The values  $T_1T_2$  and 'a' can then be adjusted to give a better fit. If 'a' has been changed,  $\Gamma_L$  will have changed from the original estimation, therefore the value of  $T_2$  previously found cannot be used.

Castner [13] also gives a method for finding  $T_2$ , but the signal height must decrease to at least half its maximum as power is increased, and this condition is often not met in the samples studied in this work, even at the highest operation power of the klystron. Stoneham, in a research note [14], gives an equation relating the peak-to-peak linewidths of the Lorentzian and Gaussian components of a line, their ratio and the total peak-to-peak linewidth (of the first derivative spectrum). From this the following equation can be derived to give the half-width at half maximum of the Lorentzian component, needed to calculate  $T_2$ .

$$\Gamma_L = \frac{\sqrt{3}}{2} \left[ \frac{a' + a'^2\beta}{1 + a'\alpha + a'^2\beta} \right] \Delta B_{pp}$$

where  $a'$  is the peak-to-peak linewidth ratio,  $a' = a \sqrt{\frac{2 \ln 2}{3}}$   $\alpha = 0.9085$  and  $\beta = 0.4621$

Therefore the value of  $a$ , found from fitting to Castner's equation (refined from the Voigt fit) combined with the experimental linewidth,  $\Delta B_{pp}$ , gives  $\Gamma_L$  and from this  $T_2$ . This value and  $T_1T_2$  from Castner, adjusted from Zamorano-Ulloa, can then be used to calculate  $T_1$ .

### 3.8 References

- [1] Bruker “*B-ER 420 EPR spectrometer System Manual*”
- [2] G.E. Pake “*Paramagnetic Resonance*” pub. W.A. Benjamin Inc, New York (1962) ch.2
- [3] R.C. Barklie, L. Sealy *J. Magnet. Res.* 97(1992)611
- [4] J. Weil, J. Bolton, J. Wertz “*Electron paramagnetic resonance: Elementary theory and practical applications*” Pub. John Wiley & Sons, New York (1994) chs.2, 10
- [5] R. T. Schumacher “*Magnetic Resonance*” Pub. W.A. Benjamin Inc, New York (1970) Ch. 3
- [6] A. M. Portis *Phys. Rev.* 91(1953)1071
- [7] G. Smith, J.C.G Lesurf, R.H. Mitchell, P.C. Riedi *Rev. Sci. Instrum.* 69(1998)3924
- [8] G. Smith, *St. Andrew’s University*, Poster presentation, 2001
- [9] P.W. Anderson and P.R. Weiss *Rev. Mod. Phys.* 25 (1953)269
- [10] N. Bloembergen, S. Wang *Phys. Rev.* 93(1954)72
- [11] J.P. Lloyd, G.E. Pake, *Phys. Rev.* 92(1953)1576
- [12] R. Zamorano-Ulloa, H. Flores-Llamas, H. Yee-Madeira *J. Phys. D: Appl. Phys.* 25 (1992) 1528
- [13] T.G. Castner Jr. *Phys. Rev* 115(1959)1506
- [14] A. M. Stoneham *J. Phys. D: Appl. Phys.* 5(1972)670

## *Chapter 4*

### *Ion Implantation*

A fly, Sir, may sting a stately horse and  
make him wince; but one is still an insect,  
and the other is a horse still.

-Samuel Johnson

## 4. Ion Implanted Polymer-like Amorphous Carbon

### 4.1 Introduction

Electron paramagnetic resonance (EPR) measurements were made of defects in amorphous carbon films implanted with a range of boron, carbon or nitrogen ions. The films were grown and implanted by Riz Khan and David Carey of the Electronic Engineering Department in the University of Surrey, Guildford, UK.

The unimplanted material under study was polymer-like amorphous carbon (PLC); this has a low concentration of paramagnetic defects, of order  $10^{17} \text{ cm}^{-3}$ ; a wide band gap, high hydrogen content ( $\sim 50 \text{ at.}\%$ ) and high  $sp^3$  content. Ion implantation is one method by which ion species can be added to the film. Utilising this method enables the controlled addition of a known number of ions; further advantages are the lack of alloying of the material and the wide range of possible ions.

In previous works [1,2] measurements were made of the optical band gap, conductivity and refractive index of the ion implanted films. In this study EPR was used to study for the first time the effect of varying implantation dose on the population and nature of defects in PLC films, including measurements of the relaxation times of the carbon defect.

## 4.2 film Characteristics

Hydrogenated amorphous carbon (a-C:H) films were deposited using a 13.56 MHz rf-powered, capacitively coupled, plasma enhanced chemical vapour deposition (PECVD) system, as described in chapter 2. Films were deposited at room temperature on silicon substrates placed on the earthed electrode with feed gases of CH<sub>4</sub> (30 sccm) and He (75 sccm) at constant pressure of 200 mTorr and with 200 W rf-power. These deposition conditions lead to polymer-like amorphous carbon films. Two series of films were prepared with thicknesses of approximately 220 nm and 100 nm.

The thicker set of films was implanted with equal doses of boron ions at energies of 20 keV and 28 keV, with a total dose in the range of  $2 \times 10^{14}$  to  $6 \times 10^{15}$  ions cm<sup>-2</sup>. The 100 nm films were implanted with N, C or B ions of energies 20 keV and 32.5 keV, with the same relative dose, in the range  $2 \times 10^{12}$  to  $2 \times 10^{16}$  ions cm<sup>-2</sup>. All implants were carried out at room temperature and the beam current was in the range 11 - 20  $\mu$ A.

Simulations using the Transport and Range of Ions in Matter code (TRIM, Version 96.01) [3], using an approximation of 1:1 C:H ratio, gave the range of the impinging boron ions to be approximately 63 nm, 86 nm or 100 nm with straggles of 17 nm, 20 nm and 21 nm for the 20 keV, 28 keV and 32.5 keV implants respectively. The simulated profiles of carbon, hydrogen and silicon ions displaced during the process of boron implantation into 100nm thick films, as well as the penetration profile of

32.5 keV boron ions, are shown in figure 4.1. The films thinned during the implantation process. For films initially at 220 nm, those subjected to the highest dose of  $6 \times 10^{15}$  boron ions  $\text{cm}^{-2}$  thinned to 69.2 nm after implantation. Films initially at 100 nm thinned to 45.2 nm following implantation of  $2 \times 10^{16}$  boron ions  $\text{cm}^{-2}$ . At doses  $\leq 2 \times 10^{14}$  ions  $\text{cm}^{-2}$  the films remained at the as-grown thickness, within errors.

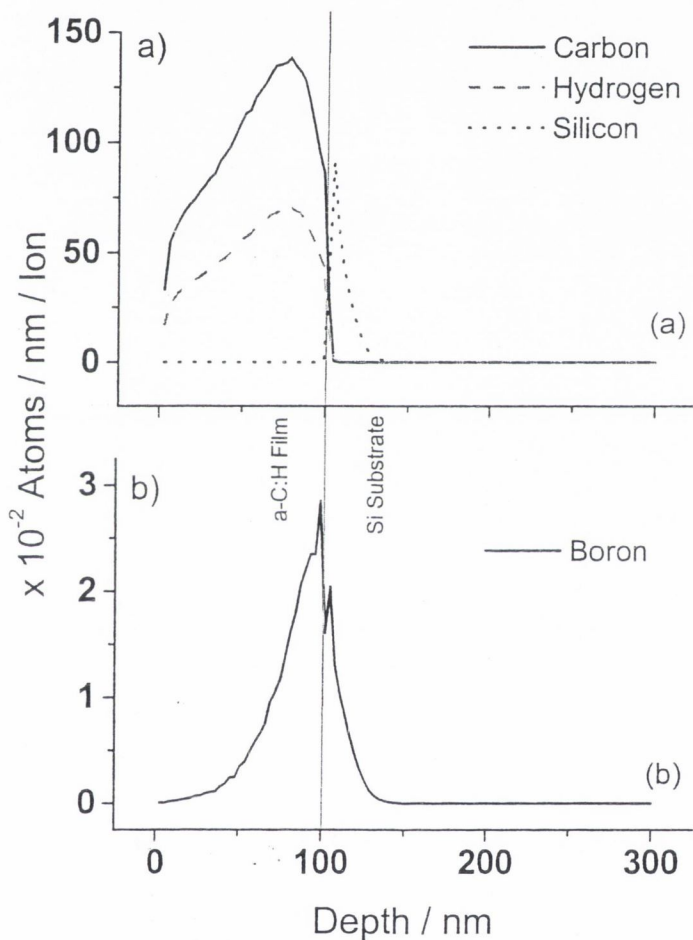


**Figure 4.1** a) Depth profile of atom displacement following ion implantation by 32.5 keV boron ions. b) Penetration profile of boron ions.

The atomic hydrogen content of the B implanted samples, measured using elastic recoil detection analysis (ERDA), is  $60 \pm 5$  at.% for samples implanted with doses  $\leq 2 \times 10^{14}$  ions  $\text{cm}^{-2}$ , decreasing to 25 at.% at the highest dose of  $2 \times 10^{16}$  ions  $\text{cm}^{-2}$ . The Tauc gap remains, within error, at the value for unimplanted films,  $2.7 \pm 0.1$  eV, for implantation doses of  $\leq 2 \times 10^{14}$  ions  $\text{cm}^{-2}$  then decreases to 1.4 eV at  $2 \times 10^{15}$  ions  $\text{cm}^{-2}$  and finally to 0.3 eV at  $6 \times 10^{15}$  ions  $\text{cm}^{-2}$ . The resistivity of the films falls from  $8 \times 10^{13}$   $\Omega\text{cm}$  at lowest implantation doses to  $9 \times 10^8$   $\Omega\text{cm}$  at  $2 \times 10^{16}$  ions  $\text{cm}^{-2}$  [1]. The film properties are summarised in figure 4.2.

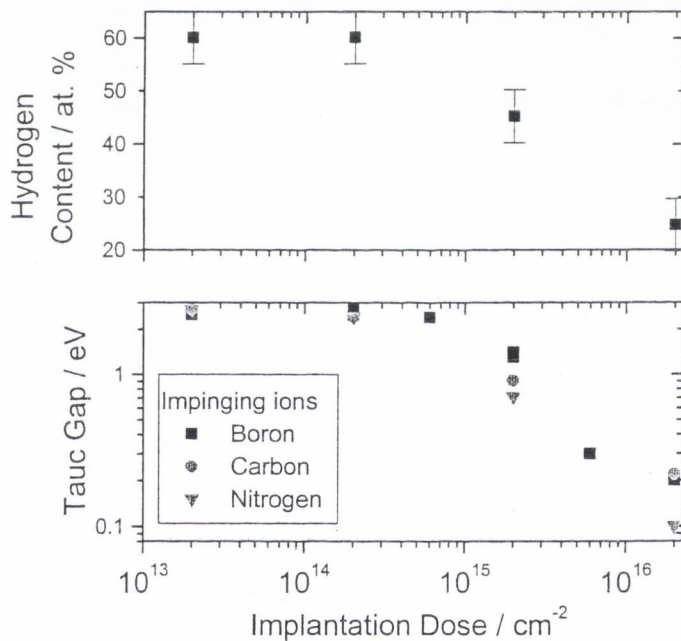


**Figure 4.2.** Decrease in hydrogen content and Tauc gap with increasing implantation dose.

### 4.3 Defect variation with implantation dose

EPR measurements were made at room temperature using the standard X-band set-up, as described in chapter 3, a microwave frequency of about 9.9 GHz and a  $TM_{011}$  mode cavity. The figure 4.3 shows the variation in EPR signal with implanting dose and implanting species.

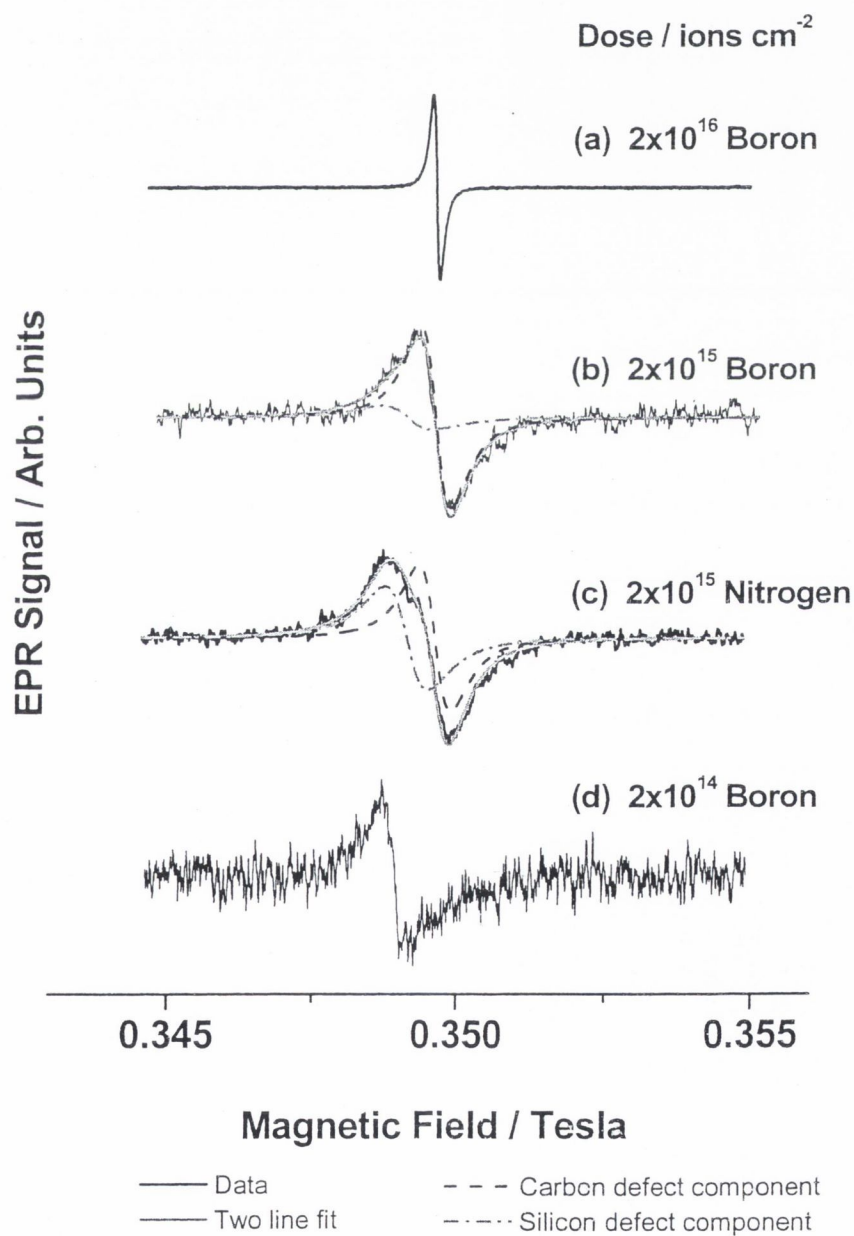


**Figure 4.3** Variation of EPR spectrum with implanting dose and species

Two paramagnetic centres were revealed. Films implanted with high doses ( $\geq 6 \times 10^{15} \text{ cm}^{-2}$ ) exhibited a single, symmetric Lorentzian line at  $g=2.0028(1)$  [fig. 4.3(a)]. Low implantation doses resulted in a symmetric resonance line at  $g=2.0058(6)$  [fig. 4.3(d)]. EPR studies of films implanted with intermediate doses revealed an asymmetric line with a  $g$ -value between 2.0028 and 2.0058 [figs. 4.3(b) and 4.3(c)]. A least squares fitting program, utilising Levenberg-Marquardt iterations, was used to fit lines to integrated spectra of the intermediate dose samples. The best fit was obtained with two Lorentzian lines, one at each of  $g \approx 2.0028$  and  $g \approx 2.006$ ; this suggests that these spectra are a superposition of the two lines seen at the extreme doses. The relative concentration of the two defects was found from the ratio of the areas of the fitted lines. The shape and  $g$  values of the observed lines suggest that the centre with  $g \approx 2.0028$  is the usual defect associated with carbon unpaired electrons in the film [4, 5] whilst the line at  $g \approx 2.006$  is similar to that previously observed [5, 6] and attributed to defects in the silicon substrate. To check the location of the defects the a-C:H film was removed from two samples, one of low implantation dose showing only the defect at  $g \approx 2.006$ , and one of intermediate implantation dose with two lines. The EPR spectrum after removal showed the intensity of the  $g \approx 2.006$  line remained the same, within errors, in both cases, whilst the spin concentration of the  $g \approx 2.0028$  centre in the intermediate dose sample dropped practically to zero. This confirms the locations suggested above; the two centres will hereafter be referred to as “silicon defect” and “carbon defect” respectively. A comparison of fitted spectra, pre- and post- film removal, for the intermediate dose sample, figure 4.4, clearly shows the dramatic decrease in the concentration of the carbon defect following the film removal. The remaining spins contributing to a line at  $g \approx 2.0028$  are attributed to incomplete removal of the film.

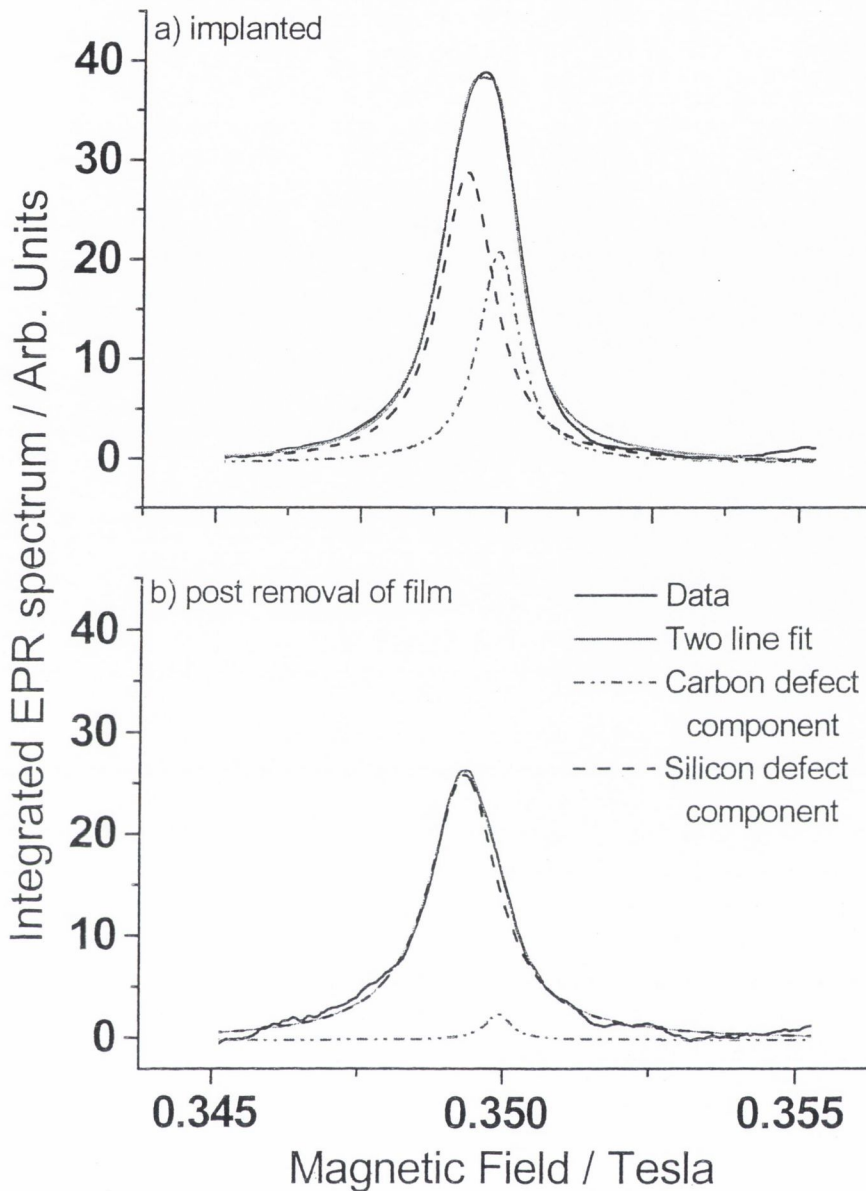


**Figure 4.4** Comparison of intensities of defects at  $g = 2.0028$  (“carbon”) and  $g = 2.0056$  (silicon), before (a) and after (b) removal of a-C:H film from the substrate

All spectra were found to consist of lines from one or other or both types of defect, as shown in figure 4.3. The boron implanted sample [figure 4.3(b)] shows fewer silicon defects than the nitrogen implanted sample [figure 4.3(c)]. This is in part because the

former is the thicker of the two, with pre-implantation thickness of 220 nm compared to 100 nm, thus fewer implanting ions or knock-ons can reach the substrate.

The areal defect density (i.e. the number of defects per unit area of one face of the sample) in the silicon substrate seems to increase with dose and saturate at about  $4 \times 10^{13} \text{ cm}^{-2}$  at a dose of  $6 \times 10^{14} \text{ ions cm}^{-2}$ . For doses of  $\geq 6 \times 10^{15} \text{ cm}^{-2}$  the silicon signal was unobservable as it was obscured by the much stronger carbon signal. As the thickness of some films is greater than the predicted range of the ions, it is presumed that the defect in these cases is produced by knock-on hydrogen atoms

From spectra of implanted samples from which a carbon signal could be extracted (doses  $2 \times 10^{15} - 2 \times 10^{16} \text{ ions cm}^{-2}$ ) an approximate volume defect concentration,  $N_V$ , was calculated by dividing the areal defect density by the film thickness after implantation, though it is important to note that this does not take into account the possibility of non-uniformity of the defect distribution. Such non-uniformity would imply the existence of regions where the spin concentration is locally greater than this average. This average volume defect density,  $N_V$ , increases approximately linearly with dose from about  $3 \times 10^{17} \text{ cm}^{-3}$  [5] in the unimplanted samples to  $2.7 \times 10^{20} \text{ cm}^{-3}$  at the highest dose of  $2 \times 10^{16} \text{ B}^+$  ions, as shown in figure 4.5(a). From this, and an approximate range of 70nm for the implanting ions, we estimate an average number of approximately 0.1 carbon defects created for every impinging ion. The increase in the number of defects can be accounted for by the loss in hydrogen, which corresponds to  $5 \times 10^{22} \text{ atoms/cm}^3$  over the same dose range, with only part of the hydrogen lost being from broken C-H bonds and with many of the carbon dangling bonds pairing up after production.

Over the entire dose range, from zero to  $2 \times 10^{16}$  ions  $\text{cm}^{-2}$ , the peak-to-peak linewidth,  $\Delta B_{pp}$  of the carbon defect line decreases from 0.83 mT [5] to 0.13 mT, and the spin-spin relaxation time,  $T_2$ , which is proportional to  $(\Delta B_{pp})^{-1}$  for Lorentzian lines, lengthens from  $6 \times 10^{-9}$  s [4] to  $5 \times 10^{-8}$  s. The spin-lattice relaxation time,  $T_1$ , calculated via the power saturation curve as detailed previously, decreases from  $3 \times 10^{-5}$  s for unimplanted samples [4] to  $6 \times 10^{-8}$  s for the highest implant dose, as shown in figure 4.5.

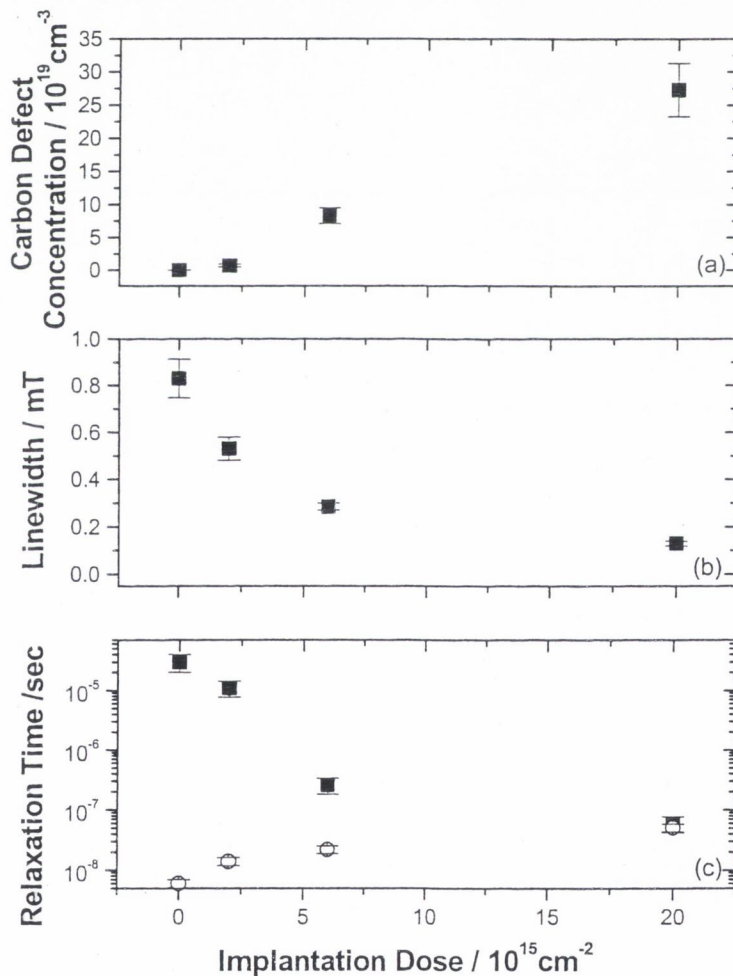


**Figure 4.5** Variation with implantation dose of carbon defect concentration (a) linewidth (b) and spin-lattice ( $T_1$ , ■) and spin-spin ( $T_2$ , ○) relaxation times (c).

When the fluctuation correlation frequency,  $\omega_c$ , becomes equal to the Larmor frequency,  $\omega_0$ ,  $T_1$  reaches a minimum, with  $T_1=1.5T_2$  [4]. At our highest dose of  $2 \times 10^{16} \text{ cm}^{-2}$   $T_1/T_2$  is within error of this ratio and thus we can estimate  $\omega_c \approx \omega_0 = 6.2 \times 10^{10} \text{ rads}^{-1}$  for this dose.

For ion doses  $\geq 6 \times 10^{15} \text{ cm}^{-2}$  the linewidth is observed to narrow to widths below that given by the equation (4.1) for dipolar broadening in a dilute system [4]:

$$4.1 \quad \Delta B_{pp} (\text{mT}) = 8.12 \times 10^{-21} N_V (\text{cm}^{-3})$$

where the peak-to-peak linewidth,  $\Delta B_{pp}$ , is in mT and defect density,  $N_V$ , in  $\text{cm}^{-3}$ .

This narrowing, to a final width of 0.13mT, was also seen by Adel *et al.* [7] and was attributed by them to motional narrowing.

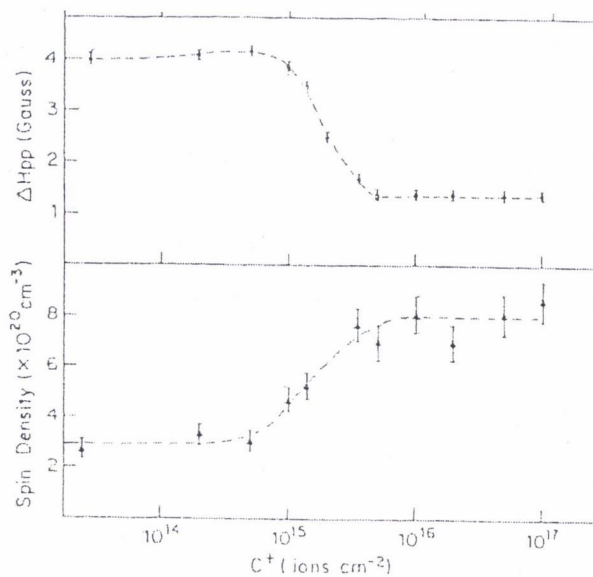


**Figure 4.6** Effect of ion implantation on spin density and EPR linewidth of DLC films [7]

Adel *et al.* [7] also show the effect of ion implantation on the spin density of their initially diamond-like films, their results are reproduced in figure 4.6. It should be noted that while the spin density of the DLC films is not affected by ion implantation of doses  $\leq 7 \times 10^{14} \text{cm}^{-2}$  these films have an initial defect density much greater than the polymer-like films in the current study. In addition my measurements do not include implantation doses  $> 2 \times 10^{16} \text{cm}^{-2}$ , which may reveal the plateau in defect density as shown by Adel *et al.* [7]

Support for the idea of motional narrowing is provided by our measurements showing that  $T_1$  decreases and  $T_2$  increases as the implantation dose is increased. A similar effect was observed as the self-bias voltage was increased by increasing the rf-power in a PECVD reactor used to grow a-C:H films on the driven electrode [4] and was also seen for polymeric materials implanted with increasing doses of boron ions [8]. In both cases this effect was shown to arise from an increasingly strong exchange interaction. The variation in  $T_{\text{auc}}$  gap as the dose is increased supports these ideas. The decrease in  $T_{\text{auc}}$  gap over this dose regime implies an increase in the  $sp^2$  cluster size [9,10], which results in greater delocalisation and hence a higher chance of wavefunction overlap.

## 4.4 Annealing

Samples implanted with doses in the range  $2 \times 10^{14}$  -  $6 \times 10^{15}$  ions  $\text{cm}^{-2}$  were annealed in argon at a pressure between  $10^{-4}$  and  $10^{-5}$  torr for five minutes, at a variety of temperatures between  $150^\circ\text{C}$  and  $550^\circ\text{C}$ . At anneal temperatures  $\leq 350^\circ\text{C}$  the EPR spectra showed no change from those for the unannealed samples. At an anneal temperature of  $550^\circ\text{C}$  the spin concentration of carbon defects is increased. The factor of increase from spin concentration in unannealed films is greater for films with lower implantation doses:  $6 \times 10^{14}$   $\text{cm}^{-2}$  and  $2 \times 10^{15}$   $\text{cm}^{-2}$  implanted films show an increase in spin concentration by factors of 3.5 and 2.9 respectively. This increase is attributed to the loss of hydrogen during annealing at this temperature, which, as in the case of hydrogen lost during the implantation process, will create more broken bonds, and reduce the  $\text{sp}^3$  fraction of the material, as described in section 2.3.2. The film implanted with  $6 \times 10^{15}$   $\text{cm}^{-2}$  shows no increase in spin concentration, within errors, for the studied anneal temperatures  $\leq 550^\circ\text{C}$ . The lack of appreciable change in this  $6 \times 10^{15}$   $\text{cm}^{-2}$  implanted sample results from the large hydrogen losses already sustained during the implantation. Previous studies on all types of a-C:H have found that the annealed film has a low hydrogen content and high  $\text{sp}^2$  content, regardless of the initial structure, which results in similar EPR signals for each of the annealed films [11,12].

## 4.5 Carbon and nitrogen implantation.

For carbon and nitrogen implantation only one implantation dosage ( $2 \times 10^{15}$  ions  $\text{cm}^{-2}$ , the highest dose for these ions) that allowed calculation of the concentration of carbon defects ( $g \approx 2.0028$ ) was available. For films with lower doses any signal from the carbon defect is obscured by the signal from defects associated with the substrate. This gives a large error on any absolute values of carbon defects per impinging ion; however, the total volume concentration of carbon defects and therefore carbon defects per impinging ion are found in the approximate ratio of 3: 4: 11 for B: C: N implantation, respectively. The concentration of silicon defects also increases with the mass of the implanting ion, reaching  $(1.7 \pm 0.6) \times 10^{14} \text{cm}^{-2}$  for the nitrogen implanted films.

Although the defects created per impinging ion increase with increasing ion mass, they do not scale linearly with either mass or vacancies per ion. These were calculated by TRIM to be 180.7, 185.7, 203.0  $\text{ion}^{-1}$  for B: C: N implantation, respectively, i.e. in the ratio 3 : 3.1 : 3.3. The nitrogen implantation appears to be significantly more effective in creating defect states, although in previous work it has been shown to passivate defects when added in a gaseous form [13].

## 4.6 Conclusion

The EPR measurements show that ion implantation creates two types of paramagnetic centres: the carbon defect with  $g=2.0028(1)$  in the film and another defect in the silicon substrate. The carbon defect has a volume spin density that increases approximately linearly with dose, from  $3 \times 10^{17} \text{ cm}^{-3}$  for unimplanted samples [5] to  $2.7 \times 10^{20} \text{ cm}^{-3}$  for implantation of  $2 \times 10^{16} \text{ ions cm}^{-2}$ . The silicon defect within the substrate has a  $g$  value of  $2.0058(6)$  and a spin concentration that saturates at about  $4 \times 10^{13} \text{ cm}^{-2}$  at a boron dose of  $6 \times 10^{14} \text{ ions cm}^{-2}$ . At high doses the carbon line narrows (to  $0.13 \text{ mT}$  at  $2 \times 10^{16} \text{ ions cm}^{-2}$ ), and the spin-lattice relaxation time decreases and approaches the spin-spin relaxation time; this is attributed to exchange (motional) narrowing of the signal, resulting from greater wavefunction overlap. This in turn may arise from increased delocalisation due to an increase in  $sp^2$  cluster size, which is revealed by the fall in Tauc gap [9, 10]. Annealing of samples at  $550^\circ\text{C}$  causes an increase in the carbon defect density, which is greater for films with lower implantation dose. This is attributed to loss of hydrogen, both creating more broken bonds and removing its stabilising influence on  $sp^3$  hybridised carbon. Annealing at temperatures  $\leq 350^\circ\text{C}$  causes no change in the EPR spectrum.

## 4.7 References

- [1] R.U.A. Khan, D. Grambole, S.R.P. Silva *Diamond Relat. Mater.* 9(2000)675
- [2] R.U.A. Khan, J.V. Anguita, S.R.P. Silva *J. Non-Cryst. Solids* 276(2000)201
- [3] J. F. Ziegler, J.P. Biersack "TRIM The stopping and range of ions in solids"  
Pergamon Press New York (1985)
- [4] R.C. Barklie, M. Collins, S.R.P. Silva *Phys. Rev. B* 61 (2000) 3546
- [5] M Collins, R.C. Barklie, J.V. Anguita, J.D. Carey, S.R.P. Silva *Diamond Relat. Mater.* 9 (2000) 781
- [6] B.P. Lemke, D. Haneman *Phys. Rev. B* 17 (1978) 1893
- [7] M.E. Adel, R. Kalish, S. Praver *J. Appl. Phys.* 62 (1987) 4096
- [8] I.V. Kozlov, V.B. Odzhaev, V.N. Popok, I.I. Azarko, E.I. Kozlova *J. Appl. Spectrosc.* 65 (1998) 583
- [9] J. Robertson, E.P. O'Reilly *Phys. Rev. B* 35(1987)2946
- [10] J. Robertson *J. Non-Cryst. Solids* 198-200(1996)615
- [11] R. T. Schumacher "Magnetic Resonance" Pub. W.A.Benjamin Inc. NY (1970)  
Ch. 3
- [12] P.W. Anderson, P.R. Weiss *Rev. Mod. Phys.* 25 (1953)269
- [13] S.R.P. Silva, J. Robertson, Rusli, G.A.J. Amaratunga *Phil. Mag. B*  
74(1996)369

## *Chapter 5*

### *Nitrogen Incorporation*

Misce stultitum consiliis brevem:

Dulce est desipere in loco.

Mix a little foolishness with your prudence:

It is good to be silly at the right moment.

- Horace

## 5. Nitrogen inclusion

### 5.1 Introduction

Amorphous carbon nitride ( $a\text{-C}_{1-x}\text{N}_x$ ) films have attracted attention recently due to their predicted mechanical and tribological properties [1]. Research into these films is motivated by a desire to characterise their properties, to examine electronic doping of a-C and to produce the hypothetical superhard compound  $\beta\text{-C}_3\text{N}_4$  [2, 3], which is expected to have a hardness greater than that of diamond [4]. There is little evidence of the  $\beta\text{-C}_3\text{N}_4$  phase so far, however, and it has been difficult to produce films with the required 57% nitrogen content [2, 5]. However, a-CN films with <57% N exhibit interesting properties such as fullerene-like microstructure, high hardness and elasticity [5]. Identifying a need for new interlayer dielectric materials, Aono and Nitta [6] have studied amorphous carbon nitride, sputtered from graphite, as a candidate for a low dielectric constant (low-k) material.

Research on hydrogenated amorphous carbon nitride,  $a\text{-C}_{1-x}\text{N}_x\text{:H}$ , shows a possible potential application as an ultra-thin thermoluminescent (TL) dosimeter [7] as well as applications as electronic materials and in electrochemical studies of water treatments [1]. The addition of nitrogen to a-C:H also significantly modifies the photoluminescent behaviour of the material [8]. Nitrogenation of hydrogenated amorphous carbon has also been studied as a way to improve the properties of the material to make it more attractive for use as a field emission cathode in flat panel displays [9].

EPR studies can determine the number of defects within the material, a crucial parameter for many of these applications, as well as providing information on the structure of the carbon film [10,11].

## 5.2 Nitrogen in a-C:H

a-C films incorporating nitrogen can be produced, for example, by the addition of nitrogen into the precursor gas mix for PECVD/IDECR films (see chapter 2), by ion implantation, or by sputtering a graphite target in an atmosphere containing nitrogen. N incorporation in a-C:H and ta-C films has been found to increase the conductivity of the material [1, 3, 9], though it has been unclear whether this increase is due to graphitisation of the carbon, i.e. an increased  $sp^2$  content leading to a narrower bandgap, or to nitrogen doping, raising the Fermi level towards the conduction band [1, 3].

Silva *et al.* [3] produce evidence to suggest that N incorporated into ta-C acts as a substitutional donor (i.e. the nitrogen replaces a carbon atom, and has a free electron) though it has a low doping efficiency. The  $sp^2$  content of their ta-C does not increase for films with less than about 10 at.% nitrogen incorporation.

Nitrogen can be accommodated in a-C(:H) in a number of configurations, as shown schematically in figure 5.1 [3]. Nitrogen has five valence electrons, so provides an extra electron wherever it replaces carbon in the material.

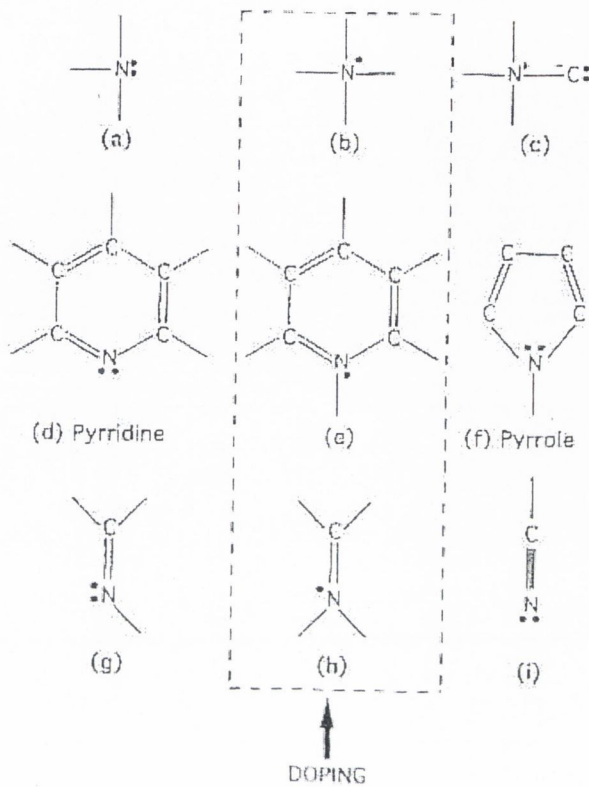


**Figure 5.1** Possible configurations of nitrogen in a-C:H. The lines represent bonds, the dots are unpaired electrons and the dot pairs are lone pairs

N can form  $\pi$  or  $\sigma$  bonds, thus can be incorporated in a single substitutional site (figure 5.1b), within a 6-fold benzene ring (e) or in a double bonded unit (h), all leaving one electron unpaired and available for doping. Non-doping arrangements (a,d,f,g,i) have nitrogen with three electrons in bonds with neighbours and the remaining two form a lone pair. [3, 9]

## 5.3 Film Properties

In this chapter I report the findings of EPR studies on  $a\text{-C}_{1-x}\text{N}_x\text{:H}$  films on crystalline silicon substrates produced by IDECR plasma deposition from a precursor gas mix of acetylene and nitrogen in various ratios.

Three sample sets were examined, named GQ, GR, GS. All films were deposited with a common microwave power of 100W, substrate temperature of  $\sim 50^\circ\text{C}$ , and pressure in the range 1-3 mTorr. Nitrogen incorporation was obtained by varying the flow rate ratio,  $\text{N}_2/\text{C}_2\text{H}_2$ , in the gas phase, from 0-1.0 for sets GQ and GR and from 0-1.2, in finer steps, for set GS, corresponding to nitrogen inclusion in the deposited film of 0.7at.% to 20 at% [12]. Set GQ is grown with zero rf-power, which results in soft polymer-like films with a low defect density and a hydrogen content of  $\sim 45\%$ , as shown in table 5.1a, below.

Name	RFpower / W	bias / V	Flow rate ratio $\text{N}_2/\text{C}_2\text{H}_2$	deposition pressure mTorr	$\text{C}_2\text{H}_2$ flow / sccm	thickness / nm
GQ1	zero	zero	0	2.1	30	347
GQ2	zero	zero	0	1.0	16.5	185
GQ3	zero	zero	0.1	1.1	15	377
GQ4	zero	zero	1.0	2.1	15	847

**Table 5.1a** Properties of carbon nitride films, GQ series

Set GR is grown with 30 W rf-power, with negative self- bias voltages of  $\approx 60\text{V}$ , leading to diamond-like carbon (DLC) films with a hydrogen content of

approximately 30 at.% [13]. The thickness and deposition parameters for each film are detailed in table 5.1b.

Name	RFpower / W	bias /V	Flow rate ratio N <sub>2</sub> /C <sub>2</sub> H <sub>2</sub>	deposition pressure mTorr	C <sub>2</sub> H <sub>2</sub> flow / sccm	thickness / nm
GR1	30	56	0	2.2	30	810
GR2	30	62	0	1.0	16.5	195
GR3	30	69	0.1	1.1	15	154
GR4	30	66	1.0	2.1	15	514

**Table 5.1b** Properties of carbon nitride films, GR series

GS films are also grown with 30 W rf-power, with a lower bias voltage of  $\approx 12$ V, leading to films with lower defect densities and a nanostructure between PLC and DLC. Again these films have a hydrogen content of approximately 30 at.%. Set out in table 5.1c are the film thicknesses and nitrogen flow ratios.

Name	Flow rate ratio N <sub>2</sub> /C <sub>2</sub> H <sub>2</sub>	thickness / nm
GS1	0	270
GS2	0.07	349
GS3	0.3	211
GS4	0.3	355
GS5	0.5	369
GS6	0.7	369
GS7	0.9	514
GS8	1.2	370

**Table 5.1c** Properties of carbon nitride films, GS series

Recent results [12] show that varying the nitrogen atomic concentrations from 0.7 to 28at.% causes the room temperature conductivity,  $\sigma_{RT}$ , to increase by about five orders of magnitude ( $10^{-9}$  -  $10^{-4} \Omega^{-1}\text{cm}^{-1}$ ).

Approximating to a simple model, the conductivity can be described by:

$$(5.1) \quad \sigma = \sigma_0 \exp\left[-\frac{E_\sigma}{kT}\right]$$

Then, the apparent activation energy,  $E_\sigma$ , decreases from 0.46 to 0.24 eV with the addition of nitrogen, saturating at this value for  $(N/N+C) \geq 5$  at.%, while the conductivity prefactor,  $\sigma_0$ , increases continuously from  $10^{-2} \Omega^{-1}\text{cm}^{-1}$  to  $1 \Omega^{-1}\text{cm}^{-1}$ .

The conductivity results have been interpreted [13, 14] as being due to a decrease in the distortion of  $sp^2$  regions, as nitrogen content is increased, resulting in greater delocalisation of  $\pi$  states.

Resonant Raman spectroscopy was conducted on the GS (intermediate properties) sample set. Whilst Lacerda *et al.* [1] warn that analysis of Raman spectra is a subjective procedure, in all cases the best fits to the spectra for these films are obtained by four Gaussian lines, corresponding to the usual G-peak ( $1515 - 1550\text{cm}^{-1}$ ) and D-peak ( $1356-1390 \text{cm}^{-1}$ ) found in DLC films, to a band around  $1594-1600\text{cm}^{-1}$  assigned to olefinic  $Csp^2$  double bonds ( $C=C$  or  $C=N$ ) and to a band around  $1180 - 1224\text{cm}^{-1}$  which, at a much lower intensity than the other three, is related to the  $Csp^3$  configurations [1]. These features are consistent with results previously obtained for a-C:N films [15, 16]. Raman measurements show that the

intensity ratio,  $I_D/I_G$ , for these films increases with nitrogen addition, from 1.2 to 2.1 when N flow rate ( $N_2/C_2H_2$ ) increases from 0 to 1.2, and there seems to be no systematic correlation between  $I_D/I_G$  and excitation wavelength [1]. The study also shows that the D-peak narrows with increasing nitrogen, and the G-peak position shifts to higher wavenumbers (from 1520 to 1550 $cm^{-1}$ ) as  $N_2/C_2H_2$  increases from 0 to 0.4-0.5 and remains at this position for higher N flow rates. Lacerda *et al.* [1] argue that these results suggest that the  $sp^2$  nanostructure becomes less distorted with nitrogen incorporation.

## 5.4 EPR Results

### 5.4.1 Polymer like Films (“GQ”)

The EPR spectra of these films exhibited a single resonance line at  $g = 2.0026(3)$  consistent with the ‘carbon’ defect reported in the previous chapter. In contrast to the defects found by ion implantation, however, these lines are not Lorentzian, but have a Voigt shape, i.e. a convolution of Lorentzian and Gaussian components. The peak-to-peak linewidths,  $\Delta B_{PP}$ , decrease with increasing nitrogen content, from 14.2 $\pm$ 1.2 G for GQ1, the film deposited with zero nitrogen flow rate (and thus only a nitrogen content of 0.7at.% [13]) to 10.7 $\pm$ 1.0G for a flow rate ratio of 1:1. This decrease in width follows the decrease in volume defect density,  $N_V$ , from (3.2 $\pm$ 0.7)  $\times 10^{19} cm^{-3}$  for GQ1 to (7.6 $\pm$ 2.0)  $\times 10^{18} cm^{-3}$  for GQ4 with the highest nitrogen : acetelyne ratio of 1:1. The linewidth, however, is much greater than that calculated from  $N_V$  assuming pure dipolar broadening, as in equation 4.1. This, coupled with

the shape of the lines and high hydrogen content suggest that there is a contribution to the linewidth due to unresolved hydrogen hyperfine structure, or possibly a spread in  $g$  values of the carbon line, though studies involving high frequency EPR suggest that there is little  $g$  value spread for non-nitrogenated a-C:H [17, 18]. The difference between linewidth predicted by dipolar broadening and measured linewidth is a factor about six for GQ1, and increases with the addition of nitrogen to a factor of  $\approx 15$  for GQ4, suggesting the possibility of nitrogen hyperfine structure making some contribution to the linewidth.

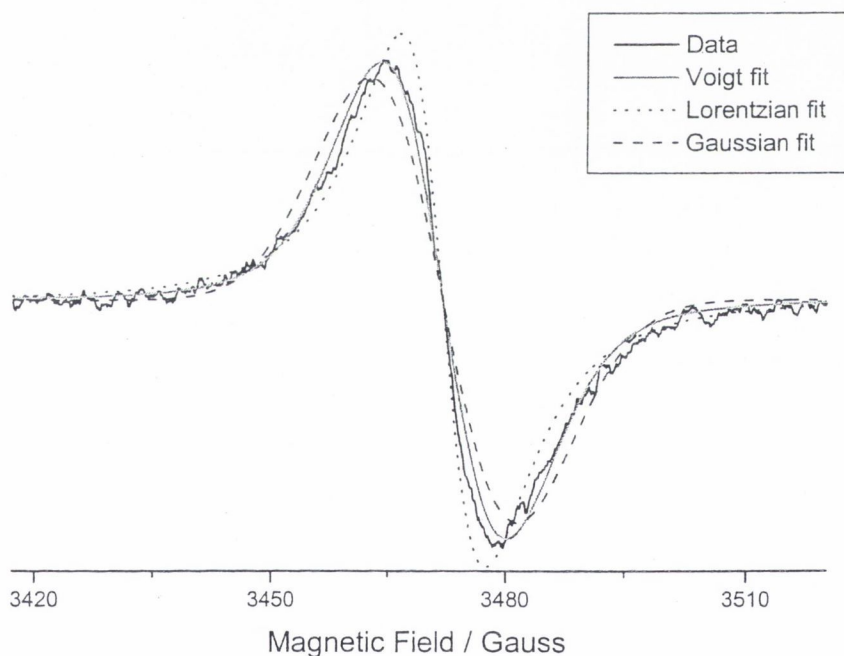


**Figure 5.2** Collected spectrum from GQ1, with Lorentzian (dotted line), Gaussian (dashed line) and Voigt (smooth solid line) best fits.

It is possible to deconvolute the EPR lines into Lorentzian and Gaussian components. However, fitting a Voigt line to the integrated spectrum using Levenberg-Marquardt iterations, as shown in figure 5.2 (differentiated to allow comparison with original data) does not always result in a reproducible linewidth

ratio ( $\Gamma_L/T_G$ ). As the lines are not purely Lorentzian, the standard technique for finding relaxation times, as detailed in chapter 3, is not applicable, and a method combining the works of Castner [19], Stoneham [20] and Zamarano-Ulloa *et al.* [21] is employed, as described in section 3.7.2. This method uses all the integrated spectra that make up the power saturation curve; thus the values obtained are not dependent on a single spectrum. Also, as a beneficial side effect, the relaxation time calculation provides a refinement of the linewidth ratio. A saturation curve and fit are shown as figure 5.3.

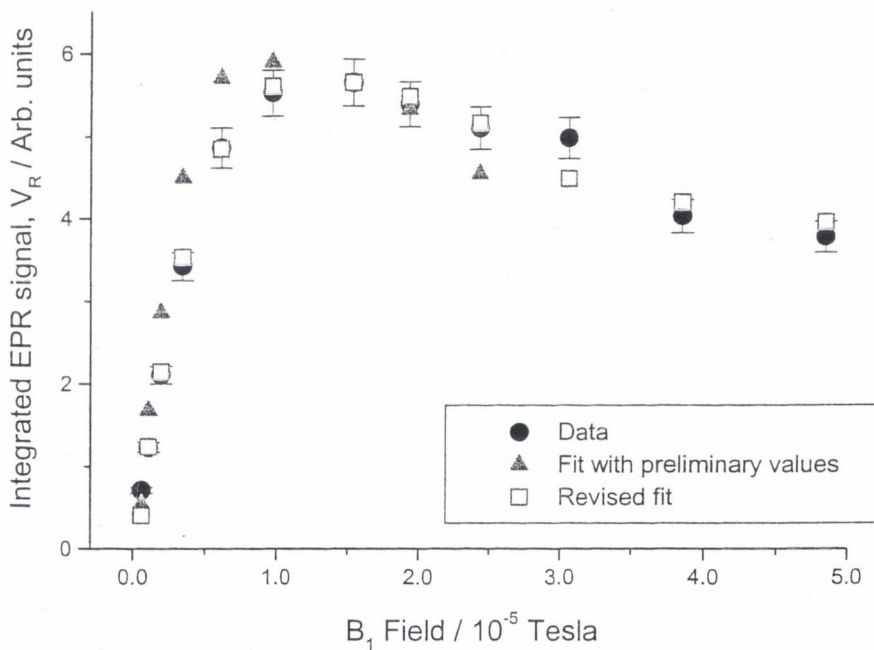


**Figure 5.3** Saturation curve, integrated EPR signal versus microwave,  $B_1$  field, for sample GQ3, showing fit from Voigt fitting and Zamarano-Ulloa relaxation time calculation [21]( $\blacktriangle$ ) and revised fit ( $\square$ ) after Castner [19].

While this method is better than simply using a Voigt fit, I estimate that the uncertainty in the spin-spin relaxation time,  $T_2$ , is approximately 25% and is about 45% for the spin-lattice relaxation time,  $T_1$ . For these films there is, with increasing

nitrogen content, a slight increase in  $T_2$  from  $\approx 1 \times 10^{-8}$  to  $\approx 2 \times 10^{-8}$  s.  $T_1$  is of similar times to those that have been previously observed in polymer-like films [10, 21, 22] and increases with nitrogen addition, from  $\approx 7 \times 10^{-6}$  s for GQ1 with no nitrogen, to  $\approx 2.2 \times 10^{-5}$  s for GQ4. Full results are shown in table 5.2, below.

sample	$N_V / 10^{19}$ $\text{cm}^{-3}$	linewidth / G	$T_1 T_2 /$ $10^{-13} \text{s}^2$	$\Gamma_L / \Gamma_G$ ("a")	$\Gamma_L /$ G	$T_2 /$ $10^{-8} \text{s}$	$T_1 /$ $10^{-5} \text{s}$
GQ1	$3.2 \pm 0.7$	$14.2 \pm 1.2$	0.80	0.80	5.1	1.1	0.72
GQ2	$8.0 \pm 1.6$	$13.9 \pm 0.8$	1.14	0.35	2.6	2.2	0.52
GQ3	$2.7 \pm 0.5$	$13.0 \pm 0.9$	1.59	0.55	3.5	1.6	0.98
GQ4	$0.76 \pm 0.20$	$10.7 \pm 1.0$	4.41	0.52	2.8	2.1	2.2

**Table 5.2** EPR results for GQ series films, with relaxation time product  $T_1 T_2$  and ratio,  $\Gamma_L / \Gamma_G$ , of linewidth components calculated from saturation curves following Castner [19]. Further analysis after Stoneham [20] providing the Lorentzian line component  $\Gamma_L$  and relaxation times  $T_1$  and  $T_2$ . Error margins are as stated in the text.

### 5.4.2 Diamond-like films ("GR")

These films, deposited with rf-power of 30 W and negative self bias of 300V, are diamond-like in nature and thus have higher defect densities than the PLC films just discussed. Each sample in this series exhibits a single symmetric Lorentzian resonance line (with high signal to noise ratio) at  $g=2.0027(2)$ . The defect densities, linewidths, and relaxation times for these films are shown below in table 5.3, where the "predicted width" is, from equation 4.1, the linewidth estimated from the volume defect density, assuming a Lorentzian line and pure dipolar broadening.

Name (N <sub>2</sub> /C <sub>2</sub> H <sub>2</sub> )	N <sub>V</sub> / 10 <sup>19</sup> cm <sup>-3</sup>	linewidth, ΔB <sub>pp</sub> / G	Predicted width / G	T <sub>1</sub> / 10 <sup>-7</sup> s	T <sub>2</sub> / 10 <sup>-8</sup> s
GR1 (0)	16±3	4.2±0.2	13.2	2.4±0.4	1.58±0.17
GR2 (0)	37±7	4.7±0.3	30.1	2.7±0.5	1.43±0.19
GR3 (0.1)	36±6	4.7±0.2	29.2	2.6±0.5	1.41±0.16
GR4 (1.0)	8.0±1.4	5.8±0.3	6.5	6.3±1.1	1.15±0.13

**Table 5.3** EPR results for GR series films.

The difference in defect density between films GR1 and GR2, both with no intentionally added nitrogen (0.7% nitrogen incorporated into the film [13]), is attributed to the increased deposition energy of the ions in film GR2, resulting from the reduced deposition pressure used during the manufacture of this film (see table 5.1b).

In both these films the signal does not saturate easily with microwave power, as quantified by spin-lattice (T<sub>1</sub>) and spin-spin (T<sub>2</sub>) relaxation times of  $\approx 2.5 \times 10^{-7}$  s and  $\approx 1.5 \times 10^{-8}$  s respectively. The short T<sub>1</sub>, a linewidth significantly less than that expected due to dipolar broadening [21] and the Lorentzian lineshape are indicative of exchange narrowing [10, 21, 23, 24]. As argued in previous works [10, 21, 25-27], this is consistent with spins in the sp<sup>2</sup> phase.

Introducing nitrogen with a flow rate ratio (N<sub>2</sub>/C<sub>2</sub>H<sub>2</sub>) of 0.1 ( $\approx 7$  at. % nitrogen in the film [13]) produces no change, within errors, in any of the measured parameters. However, increasing the flow rate ratio to 1.0 (as in film GR4, containing  $\approx 20$  at. % nitrogen [13]) produces a drop in N<sub>V</sub> to  $(8.0 \pm 1.4) \times 10^{19} \text{ cm}^{-3}$  and an increase in

linewidth to  $5.8 \pm 0.2$  G, with relaxation times  $T_1$  and  $T_2$  changing to  $(6.3 \pm 1.1) \times 10^{-7}$  s and  $(1.2 \pm 0.1) \times 10^{-8}$  s respectively. There is still likely to be exchange narrowing of this line, as  $T_1$  has lengthened by less than a factor of three.

Experiments were also conducted to try and find direct evidence of nitrogen existing in a doping configuration within the a-C:H film. EPR measurements on diamond can show a resonance spectrum from single substitutional nitrogen, the so-called P1 centre [28, 29], an isolated impurity nitrogen atom substituted for carbon in the diamond lattice. Simulations of a powder pattern with the addition of a single nitrogen nucleus were carried out using WINEPR SimFonia [30], using  $S=1/2$ ,  $I=1$  and the non-zero values of the nuclear hyperfine interaction matrix:  $A_{xx} = A_{yy} = 114$  MHz and  $A_{zz} = 81.3$  MHz. One example of a spectrum obtained from such a simulation is shown in figure 5.4. It was thought that the central N peak, at  $g \approx 2.0024$  [31], would be obscured by the main carbon defect signal. Thus EPR spectra from the GR series films were collected with the field sweep range only just extending into the region of the carbon line. Therefore the gain could be turned to maximum to allow the search for the nitrogen satellites, as indicated in the simulation, located at a separation of approximately 40 G from the central peak.

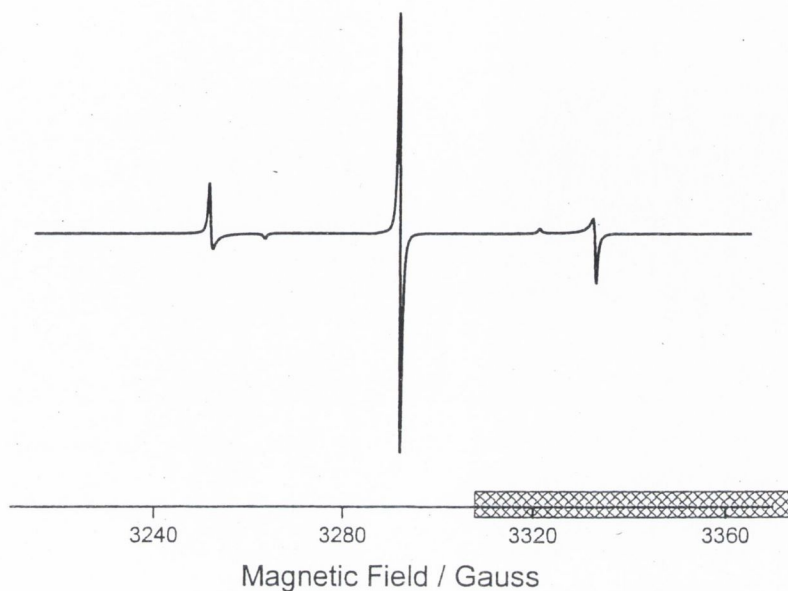


**Figure 5.4** Simulation of nitrogen inclusion, in doping configuration, in a-C:H (details on p.73). Hashed region indicates area compared with experimental spectra, avoiding main carbon peak

Using cryo-apparatus described in section 6.2, experimental spectra were taken in this region for temperatures between 300 K and 140 K. It was hoped that any shallow nitrogen donors that may have been thermally excited at room temperature could have been detected as the temperature was decreased, also low temperature measurements would mean that the susceptibility (assuming the Curie model), and thus the signal intensity, increased. However, the P1 centre saturates easily in diamond [28], and thus decreasing the temperature further may well have been a worthless exercise, considering the operation power range of the spectrometer.

Despite using a maximum gain, and examining spectra taken at various temperatures, no direct evidence of nitrogen acting as a dopant was uncovered. By comparing the experimental noise level with a simulated satellite line, and assuming that a line with signal-to-noise ratio of 2:1 is the limit of detection, an upper limit for the number of nitrogen atoms acting as donors can be determined. I estimate a maximum number of  $\approx 10^{12} \text{ cm}^{-2}$  atoms could be present in this configuration and yet remain undetected; this corresponds to approximately only one in one million of the nitrogen atoms incorporated acting as dopants.

### 5.4.3 Intermediate films (“GS”)

Each carbon film in this set exhibits a single resonance line at a  $g$  value of approximately 2.0024. The spin density,  $N_V$ , and the peak-to-peak linewidth  $\Delta B_{pp}$ , deduced from the analysis of the EPR line, are presented as a function of the N flow rate ratio ( $N_2/C_2H_2$ ) in figure 5.5 (a,b) respectively.

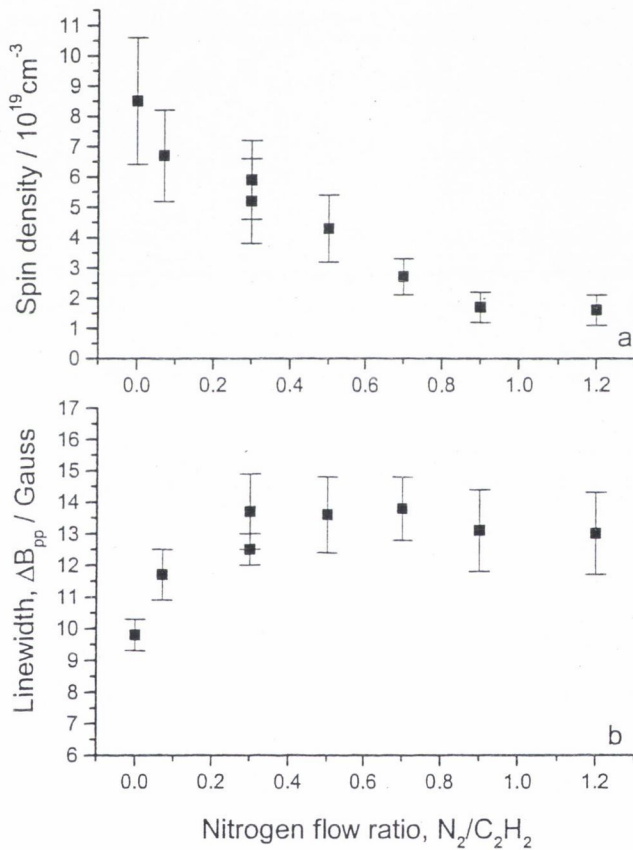


**Figure 5.5** Room temperature EPR, showing variation with nitrogen flow rate of a) volume spin density and b) peak-to-peak linewidth, in the intermediate structure “GS” films

The zero N flow rate ratio film, GS1, (corresponding to about 0.7 at.% of N in the sample) has a spin density of  $(8.5 \pm 2.1) \times 10^{19} \text{ cm}^{-3}$ , which is slightly less than the value  $\sim 10^{20} \text{ cm}^{-3}$  for the DLC films of the previous section, as would be expected

due to the lower bias [21]. This is still much greater than  $\sim 10^{17} \text{ cm}^{-3}$  which can be observed in some PLC films [21]; this reflects the intermediate nature of these films. The spin density decreases gradually to  $1.6 \times 10^{19} \text{ cm}^{-3}$  as the  $\text{N}_2/\text{C}_2\text{H}_2$  ratio increases to 1.2.

Figure 5.5b shows that the linewidth,  $\Delta B_{pp}$ , is equal to  $9.8 \pm 0.5 \text{ G}$  at zero N flow rate, a value greater than those ( $\approx 5\text{G}$ ) usually reported for the DLC films grown under high bias and also greater than the dipolar prediction of  $7 \text{ G}$  [21]. Figure 5.6b also shows that  $\Delta B_{pp}$  increases to  $13.5\text{G}$  as the flow rate ratio is increased to 0.5, and that there is no change, within error, in  $\Delta B_{pp}$  as the nitrogen content is further increased. The spin-lattice and spin-spin relaxation times,  $T_1$  and  $T_2$  respectively, were estimated to be  $(2.6 \pm 1.6) \times 10^{-6} \text{ s}$  and  $(1.1 \pm 0.2) \times 10^{-8} \text{ s}$  for the film deposited at a flow rate ratio of 0.3.

The study of this series of films is complicated by a broad asymmetric signal of unknown origin (at  $g \approx 1.98$ ) due to the substrate of some films, as shown in figure 5.6, which has to be subtracted before further processing on the sample scans. The best method of subtraction (over the  $200\text{G}$  sweep used) is by approximation to a 6th order polynomial. This method is not perfect, however, and the deviation of the resultant baseline from the linear causes unacceptable errors when performing integration. For this reason the spin density is calculated from the derivative (collected) signal using an approximation as detailed in equation 3.2, assuming a Lorentzian line shape, as suggested by fits to GS1. Further, the presence of this line

and the method of subtraction may be the cause of the g-value being slightly lower than expected for the defect associated with unpaired electrons in carbon [10, 32]

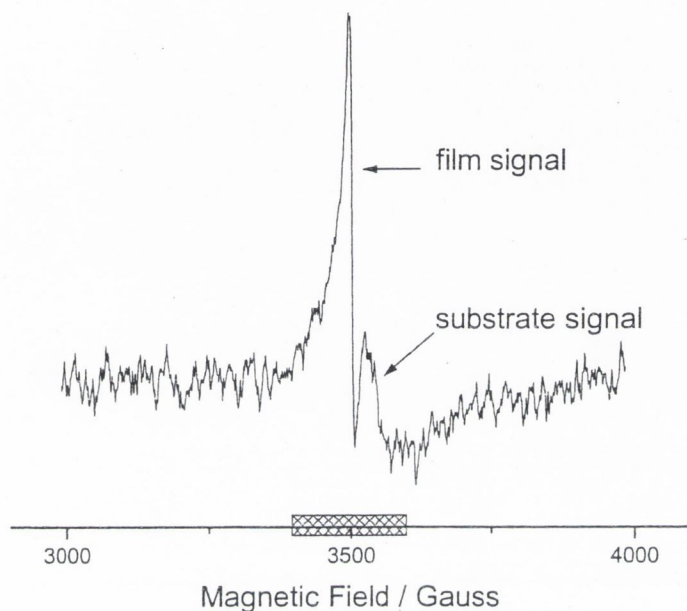


**Figure 5.6** Room temperature EPR spectrum of GS5, showing resonance peaks over a 1000G range. Scans for measurements were taken over the 200G (hashed) range shown, and the substrate signal approximated to a

The substrate also causes a reduction in the sensitivity ( $Q$ ) of the cavity by a factor of approximately five. This substrate signal and  $Q$ -factor reduction are not present in sample GS3 (0.3 nitrogen flow rate). Studies of GS3 show that the line is a Voigt shape, a convolution of Lorentzian and Gaussian, whilst GS1, with zero nitrogen flow rate, seems to be Lorentzian. This suggests the possibility that the EPR line becomes more Gaussian with increased nitrogen content. As described in equation 3.2, a Gaussian line has approximately one quarter of the spin concentration of a Lorentzian line of the same height and peak-to-peak width. Thus the calculated spin densities for films with higher nitrogen content may be over-estimated, making the fall in defect concentration more pronounced than is suggested by these figures.

## 5.5 Discussion

The decrease in volume defect density,  $N_V$ , with nitrogen incorporation, observed in all film types in this study, is consistent with previous works [3, 33, 34], and can be attributed to a decrease in disorder in the films [9, 13], i.e. with increasing nitrogen addition there is less buckling and distortion of the aromatic rings. The role of nitrogen in reducing the strain in  $sp^2$  carbon, then, is analogous to that of hydrogen incorporation in  $sp^3$  bonded carbon (as discussed in chapters 2 and 4). This decrease in disorder is in good agreement with the changes in room temperature conductivity for these IDECR films, the increases in which, with added nitrogen, have been attributed to a better overlap of the p-orbitals, thus an increase in the localisation length, as a consequence of a less constrained environment [2, 9, 13]

The observed decrease in  $N_V$  should lead to a smaller dipolar interaction and thus a narrower line (chapter 3). However, the measured linewidth decreases with nitrogen addition only in the zero-bias, GQ, series of films, where the linewidth is already several multiples of the predicted dipolar width. Considering the high hydrogen content of these films and the Gaussian component of the width, the greater than predicted linewidth is most likely due to a contribution from unresolved hydrogen hyperfine structure.

However, other factors will affect the linewidth. In the GR series of “diamond-like” films the resonance line is highly exchanged narrowed and in all the films

increasing nitrogen content causes a lengthening of the spin-lattice relaxation time,  $T_1$ , suggesting that any exchange, or motional, narrowing of the line is reduced [10, 21].

The spin-lattice relaxation time of the most nitrogenated DLC film (GR4) is, however, at  $(6.3 \pm 1.1) \times 10^{-7}$  s still sufficiently short to give a line of width less than that predicted by dipolar interaction alone, and has a Lorentzian shape, consistent with the line being exchange narrowed. Films in the GS set have fewer spins, and exchange (as characterised by  $T_1$ ) has less effect on the linewidth. The shape of the resonance line of these films seems to become increasingly Gaussian with added nitrogen. This suggests a inhomogeneous linewidth component gaining in prominence, which is likely due to unresolved nitrogen hyperfine structure, and possibly an increase in g-value spread.

The Raman spectroscopy for the GS, intermediate structure, films shows with increasing nitrogen addition an increase in the  $I_D/I_G$  ratio, a shift in the G-peak to higher wave numbers, and a narrowing of the D-peak. All of the above, Lacerda *et al.* [1] argue, are suggestive of the  $sp^2$  nanostructure becoming more ordered and less distorted with nitrogen incorporation. This is consistent with the analysis of the EPR data, given above.

## 5.6 Conclusions

Nitrogen incorporation into a-C:H films is shown to decrease the defect density in all types of films studied. This is attributed to a decrease in the disorder of the  $sp^2$  structure, the aromatic rings becoming less buckled and distorted, and thus allowing greater delocalisation. The linewidth decrease associated with this fall in spin density, as predicted by a model assuming dipolar broadening, is observed only for polymer like films.

Although measurements show that nitrogen acting as a dopant can only be within the film in concentrations of at most one in a million of the N atoms incorporated, an increase in the contribution to the linewidth due to unresolved nitrogen hyperfine structure is suggested by a Gaussian component of the lineshape, the intensity of which seems to increase with increasing nitrogen content. In addition there is a reduction in exchange narrowing for the highly nitrogenated films, as indicated by the lengthening relaxation times. These two effects could outweigh the effect of the dipolar interaction and lead to the net broadening of lines which is observed when nitrogen is added to the more diamond-like films.

## 5.7 References

- [1] M. Lacerda, M. Lejeune, B.J. Jones, R.C. Barklie, R. Bouzerar, K. Zellama, N.M.J. Conway, C. Godet *J. Non-Cryst. Solids* 299-302(2002)907
- [2] N.M.J. Conway, P. Bulkin, C. Godet *Diamond 2000 presentation chair J. Robertson* (2000)5.7.07
- [3] S.R.P. Silva, J. Robertson, G.A.J. Amaratunga, B. Rafferty, L.M. Brown, J. Schwan, D.F. Franchesini, G. Mariotto *J. Appl. Phys.* 81(1997)2626
- [4] K. Kitaguchi, H. Kiyota, M. Iida, T. Kurosu, T. Ando, I. Kusunoki *Diamond 2000 presentation chair J. Robertson* (2000)5.7.03
- [5] A. Laskarakis, S. Logothetidis, C. Charitidis, M. Gioti, Y. Panayiotatos, M. Handrea, W. Kautek *Diamond Relat. Mater.* 10(2001)1179
- [6] M. Aono, S. Nitta *Diamond Relat. Mater.* 11(2002)1219
- [7] S. Muhl, E. Camps, L. Escobar-Alarcón, O. Olea, M. Miki, N. A. Morrison *Diamond Relat. Mater.* 10(2001)915
- [8] N. Mutsukura *Diamond Relat. Mater.* 10(2001)1152
- [9] G.A.J Amaratunga, S.R.P. Silva *Appl. Phys. Lett* 68(1996)2529
- [10] B.J. Jones, R.C. Barklie, R.U.A. Khan, J.D. Carey, S.R.P Silva *Diamond Relat. Mater.* 10(2001)993
- [11] J. Robertson *Adv. Phys.* 35(1986)317
- [12] N. Conway, C. Godet, B. Equer in K.L. Jensen, W. Makie, D. Temple, J. Itoh, R. Nemanich, T. Troittier, P. Holloway (Eds.) *Mater. Res. Soc. Symp. Proc.* San Francisco, CA 621(2000)

- [13] C. Godet, N.M.J. Conway, J.E. Bouree, K. Bouamra, A. Grosman, C. Ortega  
*J. Appl. Phys.* 91(2002)4154
- [14] C. Godet *Phil. Mag. B* 81(2001)205
- [15] P. Hammer, N.M. Victoria, F. Alvarez, *J. Vac. Sci. Technol. A*  
16(1998)2941
- [16] F.R. Wixom *J. Am. Ceram. Soc.* 73(1990)1973
- [17] M. Hoinkis, E.D. Tober, R.L. White, M.S. Crowder *Appl. Phys. Lett.*  
61(1992)2653
- [18] B.J. Jones, R.C. Barklie, G. Smith, H. El Mkami, J.D. Carey, S.R.P. Silva  
*Diamond Relat. Mater.* (2002) In Press
- [19] T.G. Castner *Phys. Rev.* 115(1959)1506
- [20] A.M. Stoneham *J. Phys. D: Appl. Phys.* 5(1972)670
- [21] R. Zamorano-Ulloa, H. Flores-Llamas, H. Yee-Madeira *J. Phys. D: Appl. Phys.* 25(1992)1528
- [22] R.C. Barklie, M. Collins, S.R.P. Silva *Phys. Rev. B* 61 (2000) 3546
- [23] D.J. Miller, D.R. McKenzie *Thin Solid Films* 108(1983)257
- [24] S. Schutte, S. Will, H. Mell, W. Fuhs *Diamond Relat. Mater.* 2(1993)1360
- [25] R.U.A. Khan, J.D. Carey, S.R.P. Silva, B.J. Jones, R.C. Barklie *Phys. Rev. B*  
63(2001)121201(R)
- [26] J. Robertson *J. Non-Cryst. Solids* 198-200(1996)615
- [27] J. Robertson, E.P. O'Reilly *Phys. Rev. B* 35(1987)2946
- [28] R.C. Barklie, J. Guven *J. Phys. C: Solid State Phys.* 14(1981)3621
- [29] W.V. Smith, P.P. Sorokin, I.L. Gelles, G.J. Lasher *Phys. Rev.*  
115(1959)1546
- [30] "WINEPR SimFonia" *Bruker Analytik GmbH* v.1.25 (1996)

- [31] J.H.N. Loubser, J.A. van Wyck *Rep. Prog. Phys.* 41(1978)1201
- [32] M Collins, R.C. Barklie, J.V. Anguita, J.D. Carey, S.R.P Silva *Diamond Relat. Mater.* 9(2000)781
- [33] R.C. Barklie, M. Collins, J. Cunniffe, S.R.P. Silva *Diamond Relat. Mater.* 7(1998)864
- [34] J. Schwan, V. Batori, S. Ulrich, H. Uhrhardt, S.R.P. Silva *J. Appl. Phys.* 84(1998)2071

## *Chapter 6*

### *Nature of Defects*

Ramp up my genius, be not retrograde;

But boldly nominate a spade a spade.

-Ben Jonson

I refute it *thus*

-Samuel Johnson

## 6. Nature of Defects

### 6.1 Introduction

In this chapter I use the variation of EPR signal with temperature and frequency to examine the nature of defects within amorphous carbon.

Experiments were conducted to examine the possible deviation of the susceptibility from the generally assumed [1-3] Curie-like behaviour, which may be attributable to magnetic ordering [4]. I also examine the orientational dependence of the EPR signal at low temperature, confirming an earlier suggestion [5] that an anisotropy in the signal is due to the demagnetising field, which has recently been observed in S centres in SiO<sub>2</sub> [6], and encountered in ferromagnetic resonance [7].

The dependence on temperature of the EPR linewidth and relaxation times are discussed in terms of possible mechanisms for line broadening and narrowing, including exchange and hopping motion.

Whilst previous works [1, 2, 8], including earlier chapters of this thesis, have indicated only a single symmetric EPR line associated with the carbon defect in a-C, a recent study [9] suggested that low temperature, high frequency measurements revealed the anisotropic nature of the g tensor. Experiments were conducted in an effort to uncover evidence for this proposal. Finally, the possibility of a spread in g-

values in the carbon line is also examined by studying the change in linewidth as a function of frequency.

## 6.2 Experimental

W-band ( $\approx 94\text{GHz}$ ) EPR measurements were carried out as described in section 3.4, at St. Andrew's University, under the guidance of Drs. Smith and El Mkami. X-band ( $\approx 9.5\text{GHz}$ ) low temperature measurements were conducted using our standard spectrometer and bridge, as detailed in chapter 3, but with the usual  $\text{TM}_{011}$  cavity replaced with a rectangular  $\text{TE}_{102}$  mode cavity. This allows the use of a Oxford Instruments flow cryostat to cool the samples with helium or nitrogen gas to temperatures in the range 5-300K. The sample temperature, in the X-band set-up, was measured with a calibrated Lakeshore silicon diode sensor in contact with the sample. For orientations of this sensor / sample unit, where the plane of the sample was not perpendicular to the applied magnetic field, the temperature reading was affected by the presence of the applied field at magnitudes of  $\sim 3000\text{G}$ . For measurements where the orientation was varied, the field was reduced to between 200 G and 300 G before the temperature reading was taken, at which field the sensor was unaffected within error.

For W-Band measurements the sample was cooled by helium flowing through a heat exchanger placed just below the sample. The monitored temperature was that of this heat exchanger and thus is perhaps 2-3K below the actual sample temperature.

The samples studied in this chapter include two from the ion implanted series, described in detail in chapter 4: B1 and B2 with boron ions implanted at doses of  $6 \times 10^{15}$  and  $2 \times 10^{16} \text{ cm}^{-2}$  respectively. These have a narrow Tauc gap of 0.2-0.3eV and estimated hydrogen content of  $\approx 20 \text{ at. \%}$ . The X-Band temperature dependence of the EPR signal was also studied for films from the DLC series of IDECR carbon nitride films: GR1, GR3, GR4 with nitrogen contents of approximately 0.7, 7 and 20 at.% [10]. The film properties are fully detailed in chapter five.

Five further a-C:H samples were examined. These were all grown at the University of Surrey by Drs. Carey and Silva in a PECVD system from feed gases of 10% methane and 90% argon and deposited on the rf-driven electrode on silicon substrates. The carbon  $\text{sp}^2$  content and structure of the film were varied by altering the incident ion energy, as a result of changing the total gas pressure, P, or negative self-bias voltage,  $V_b$ , as detailed below in table 6.1. The hydrogen content is estimated to decrease slightly from 15% as the  $\text{sp}^2$  fraction increases. Full details of these films are given in [2].

Sample	Pressure, P / mTorr	Bias voltage, $V_b$ / V	$\text{sp}^2$ content / %
C100A	1000	100	56
C100B	500	100	64
C190	300	190	78
C320	300	320	80
C500	300	500	90-100

**Table 6.1** Film deposition conditions and properties

### 6.2.1 Analysis of W-band spectra

W-band ( $\approx 94\text{GHz}$ ) EPR measurements at room temperature on all these samples displayed only a symmetric Lorentzian line at  $g \approx 2.0026(2)$ , examples of which are shown in figure 6.1.

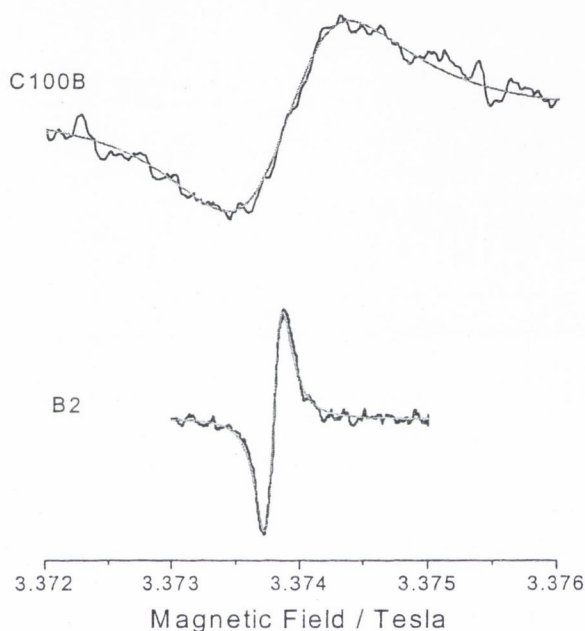


**Figure 6.1** Room temperature W-band spectra for samples C100B and B2. The smooth lines show Lorentzian fits, with degree of dispersion  $\theta = 2.9^\circ$ .

As previously discussed in chapter three, the W-band EPR system used allows collection of spectra with varying degrees of dispersion (as opposed to the pure absorption of the X-band apparatus). The spectrum can be adjusted, using the phase shift,  $\theta$ , from pure absorption (denoted as  $\theta = 0^\circ$ ) to pure dispersion with  $\theta = 90^\circ$ . As adjusting for pure absorption was a time-consuming exercise, the usual procedure

was to adjust the phase until  $\theta \approx 0^\circ$  and then fit the resultant derivative spectrum,  $Y'$ , to a mix of absorption and dispersion using the equation 6.1, as in chapter 3.

$$6.1 \quad Y' = Y_0 + A \left[ \frac{-2x}{(1+x^2)^2} \cos\theta + \left( \frac{2x^2}{(1+x^2)^2} - \frac{1}{(1+x^2)} \right) \sin\theta \right]$$

where  $x = \frac{B - B_0}{\Gamma}$ ,  $B$  is magnetic field,  $\Gamma$  is the half width at half maximum,  $B_0$  the field position of the resonance,  $Y_0$  is a linear offset, and  $A$  is the intensity scalar.

A spectrum resembling an asymmetric EPR absorption line may be observed if the absorption and dispersion components of the spectrum are of comparable magnitude. Such is the case in a spectrum from sample B1, as illustrated in figure 6.2.

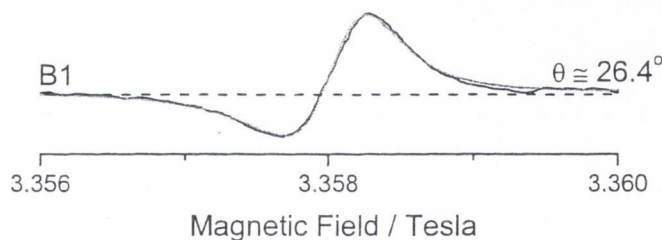


**Figure 6.2** Room temperature W-band spectrum from sample B1, with Lorentzian fit with  $\theta = 26.4^\circ$ .

A good fit from equation 6.1 (in this case with  $\theta = 26.4^\circ$ ) indicates that the absorption spectrum is a single Lorentzian line. This is confirmed by recording and fitting other spectra with  $\theta \approx 0^\circ$ . Spectra for sample B2, with a variety of degrees of dispersion, are shown with fits in figure 3.7.

## 6.3 Curie - like susceptibility

### 6.3.1 Introduction

In measurements of spin density using EPR it is often assumed that the susceptibility (which determines the intensity of the resonance line and is proportional to the number of spins) is Curie-like. Thus spectra are compared to a Curie-like standard, and the intensity of the line is expected to be inversely proportional to the temperature of the sample, and proportional to the number of spins per unit volume,  $N$ , following the equation:

$$6.2 \quad \chi_c = \frac{\mu_0 N g^2 \mu_B^2 J(J+1)}{3kT}$$

However, a number of researchers have reported possible deviations of the susceptibility from Curie-like behaviour at low temperature. Arčon *et al.* [4] show that the EPR intensity of their DLC samples exhibits a significant deviation from the Curie law at temperatures below 50K, with the intensity below that predicted, which they suggest might indicate the onset of magnetic ordering. H.J. von Bardeleben [11] indicates that preliminary results may show a deviation from the Curie law at temperatures of less than 10K. Fanchini, Ray *et al.* [12] show a signal intensity in amorphous carbon nitride films that is Curie-like above approximately 77K, then remains roughly constant below this value, as would be expected for Pauli paramagnetism [13].

### 6.3.2 Results and discussion

All samples studied (B1, B2, C100A, C190, C320, C500, GR1, GR3 and GR4) show an approximately linear relationship between  $\chi$  and  $1/T$  at temperatures from room temperature down to  $\approx 100\text{K}$ , consistent with the susceptibility being Curie-like in this temperature range, as found by other researchers [4, 12]. This section shows data collected using liquid helium as a coolant. Plots of signal intensity versus temperature, for experiments using nitrogen as a coolant, are included in appendix B.

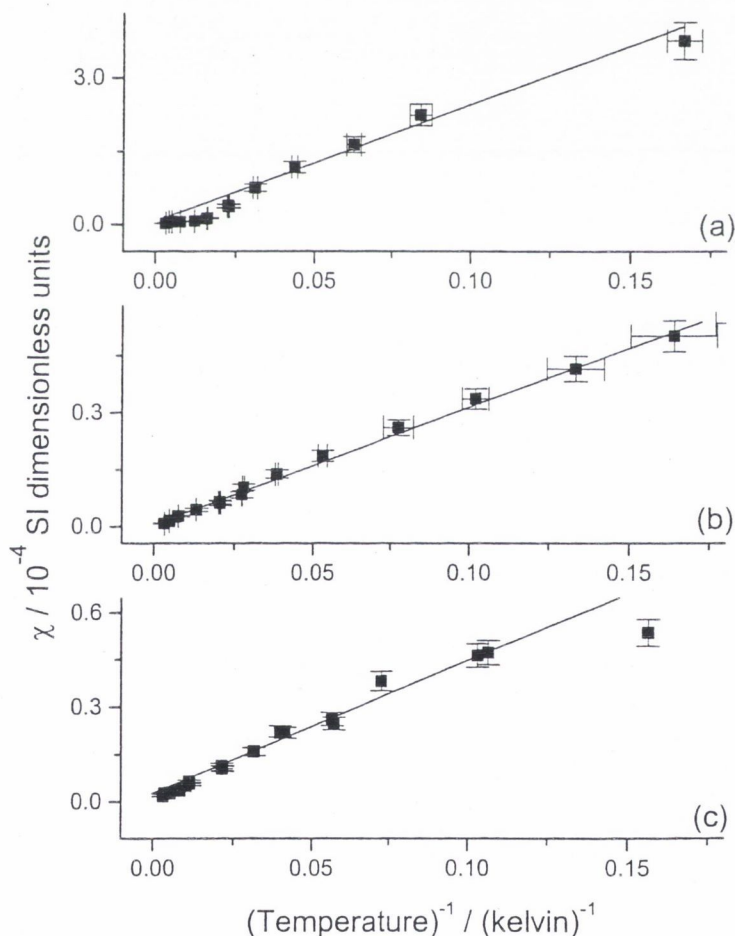


**Figure 6.3** Susceptibility, measured at X-band, plotted as a function of  $1/T$  for (a) C500 (b) C190 and (c) B1, showing little or no deviation from a linear relation. Lines are guides to the eye.

Experiments using liquid helium show that some samples, like those shown in figure 6.3, continue to show this Curie-like dependence of susceptibility at temperatures down to 5.5K. Figure 6.4 shows, however, that the measured susceptibility of other samples in this study show a deviation from the Curie law at temperatures of approximately 13 K.

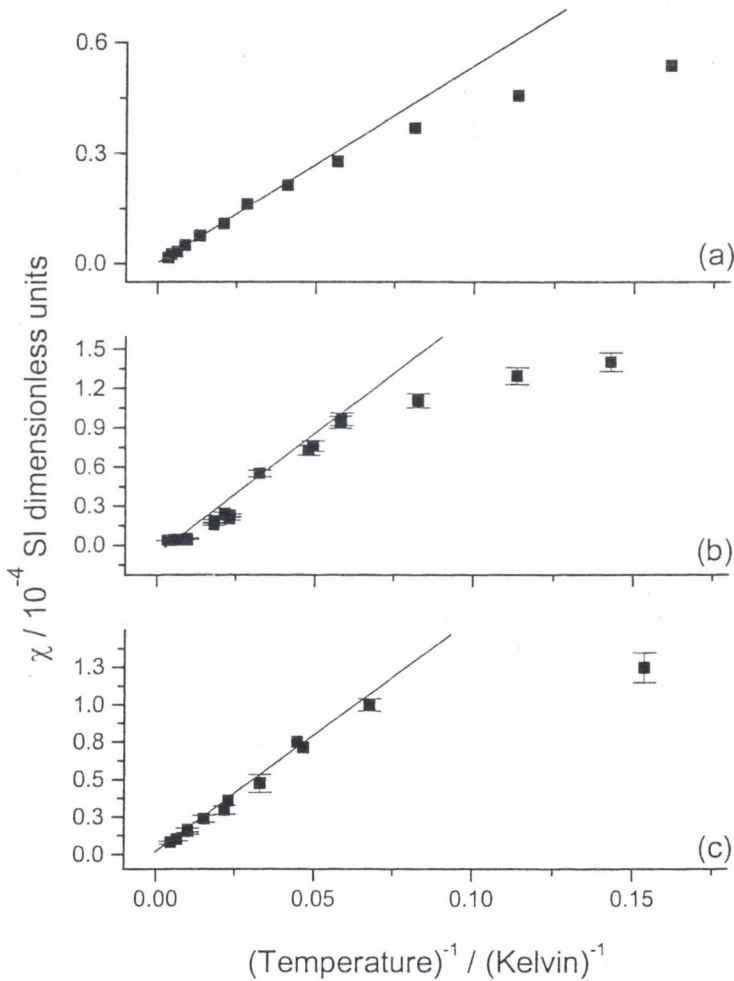


**Figure 6.4** Susceptibility, measured at X-band, plotted as a function of  $1/T$  for (a) C320 (b) C100A and (c) B2, showing deviation from linear at  $T \approx 13$  K. Lines are guides to the eye.

Somewhat surprisingly, there does not seem to be any correlation of this deviation with either the film deposition conditions or the  $sp^2$  fraction. The samples grown

with negative self-bias voltage of 500V and 190V, C500 and C190 show no deviation from the Curie law as the temperature is varied from room temperature to 5 K, whilst C320 and C100A (deposited at 320V and 100V respectively) show a susceptibility that does not change linearly with  $1/T$  below a certain temperature. The same can be said for the nitrogenated films. GR1, with no nitrogen and GR4 with  $\approx 20\text{at.}\%$  nitrogen [10] do not show Curie-like susceptibility, whereas in the film with  $\approx 7\text{at.}\%$  nitrogen the susceptibility does seem to vary linearly with  $1/T$ . Graphs of the susceptibility for these films are included in appendix B.

### 6.3.2.1 Instrumental Effects

How can I explain these results? The first thing to note is that there are instrumental or experimental factors that can affect the intensity of the observed signal. Firstly, the presence of conducting material within the cavity reduces the Q-factor, or sensitivity of the cavity. Thus, a film that is highly conducting, or on a conducting substrate, may show a signal that is somewhat less than would be otherwise seen for a given number of spins, or susceptibility – the magnitude of the reduction in height due to reduced sensitivity of the cavity is found experimentally, as described in section 3.2. All samples in this study are deposited on silicon substrates; thus, as temperature is reduced the conductivity of the substrate decreases and therefore the ‘high temperature’ intensities may be underestimated. This is the probable cause of deviation from the exact linear relation seen at temperatures  $> 40\text{K}$  (the graph of the susceptibility of C500, figure 6.3a shows this clearly), but cannot account for the deviation from the Curie law seen occurring at temperatures  $< 13\text{K}$ .

Secondly, although the measurements were all conducted at low power (20-25dB on this system), there is a probability that the signal will saturate more easily at low temperatures due to an increase in the spin lattice relaxation time (see following section). However, the decrease in signal height,  $h_{pp}$ , caused by saturation is accompanied by increase in linewidth,  $\Delta B_{pp}$ . Thus, as the double integral of the collected signal, the line intensity, is approximately proportional to  $h_{pp}(\Delta B_{pp})^2$ , the line intensity is reduced only by the cube-root of the factor of reduction of the signal height [14], not enough to produce the changes observed. Analysis of spectra at various powers (35dB – 20dB) at the lowest temperature studied, show that the normalised double integral is not reduced (within error) over this power range, for all samples studied. Further, samples such as C320 and B2 that exhibit a deviation from Curie-like susceptibility, do not show saturation at 20dB at the lowest temperature studied.

Finally, there is a possibility of an error in the temperature reading. To minimise error in this respect, a measurement is only taken once the temperature has stabilised following adjustment of the gas flow. However, for the W-band measurements the temperature sensor is located below the sample and the reading may be  $\approx 3K$  less than the actual sample temperature. This could cause an erroneous suggestion of a deviation from the linear relation between  $\chi$  and  $1/T$ . Further, the approximation used in deriving the Curie law, that  $k_B T \gg g\mu_B B$ , is not valid for  $B \sim 3T$  and  $T \sim 5K$  of the low temperature W-band measurements. For X-band measurements the sensor is in direct contact with the sample, thus there should not be any discrepancy between sample and sensor temperature. However, the sensor used is only unaffected by the magnetic field if the plane of the sample is perpendicular to the direction of the

applied field. Therefore, whilst every care was taken to ensure the orientation of the sample was correctly adjusted, a slight misalignment could mean that the measured temperature was lower than the true temperature, thus causing a slight deviation from the linear relation propounded in this section. This may be the cause of the deviation (and somewhat lower than expected temperatures) observed in samples C500 and C190 at temperatures  $\approx 4\text{K}$ , as shown in figure 6.5 (showing a greater temperature range than figure 6.3), but is probably not the root of the stronger deviation as shown in figure 6.4.

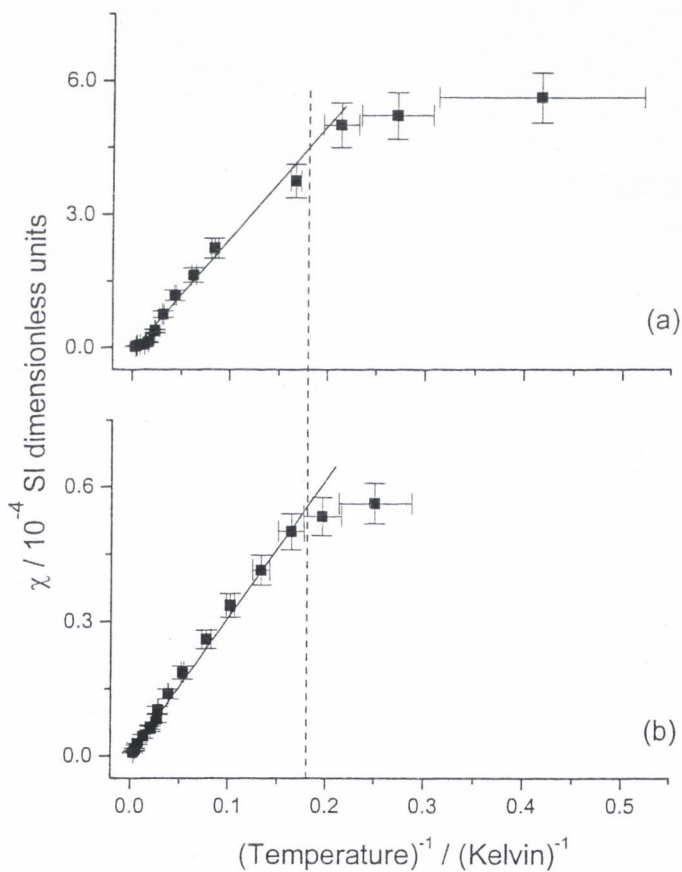


**Figure 6.5** Susceptibility plotted as a function of  $1/T$  for (a) C500 and (b) C190, showing a possible deviation from a linear relation only below  $T \approx 4\text{K}$ . The dashed line marks limit of the range of figure 6.3, solid lines are guides to the eye. X-axis error bars indicate the range of nominal temperature over the course of the measurement

### 6.3.2.2 Real effects

If instrumental effects do not cause the deviation of the susceptibility from the Curie law at temperatures of  $\approx 13\text{K}$ , what is the origin of this deviation?

One possibility, proposed by Arčon *et al.* [4] is that the deviation of the susceptibility from the Curie law indicates the onset of magnetic ordering. Arčon and co-workers argue that this magnetic transition requires the spins to be much more closely spaced than if they were homogeneously spaced throughout the material – thus is evidence for the paramagnetic defects being concentrated in the  $sp^2$ -bonded clusters proposed by Robertson and O'Reilly [15, 16] and indicative of local magnetic ordering below a certain transition temperature. The samples studied by Arčon *et al.* [4] exhibit a distinct magnetic hysteresis loop, as measured by a SQUID magnetometer at 4.2K. This is argued as additional evidence of magnetic ordering at low temperatures.

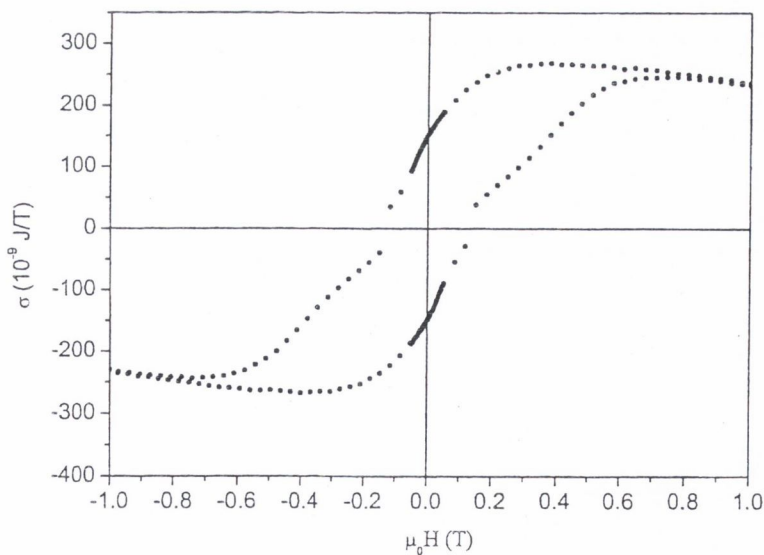


**Figure 6.6** Magnetic hysteresis loop of sample B2, measured by SQUID magnetometer at 5 K.

Magnetisation measurements on samples B2, C500 and C100A were carried out at Trinity College by Dr. M Venkatesan, using a SQUID magnetometer operating at 5K.

Each sample exhibits a hysteresis loop, with that of B2 being the most pronounced, as illustrated in figure 6.6.

Whilst the results of these measurements can be interpreted as additional evidence for magnetic ordering, the hysteresis observed could also be due to impurities within the sample or substrate [17].

Matthews *et al.* [18] show the variation of EPR intensity with temperature of their carbonised polyparaphenylene fits well to a modified Curie-Weiss law, given as:

$$6.3 \quad \chi = \frac{C}{T + \theta} + \chi_0$$

The Weiss temperature,  $\theta$ , of all samples studied by Matthews *et al.* [18] was approximately zero, and the temperature independent susceptibility component,  $\chi_0$ , was positive, suggesting the presence of a Pauli-like component of the susceptibility.

The temperature dependence of the susceptibility of the samples under study here fit to equation 6.3 with varying degrees of accuracy, as shown in figure 6.7. Table 6.2 shows the Weiss temperature derived from such fits.

Sample	$\theta$ , Weiss temperature / K
C500	$4.4 \pm 0.9$
C320	$6.3 \pm 0.4$
C190	$3.8 \pm 0.7$
C100A	$5 \pm 4$
B1	$11 \pm 6$
B2	$5 \pm 1$

**Table 6.2** Weiss temperature derived from fits

to variation in  $\chi$  with temperature.

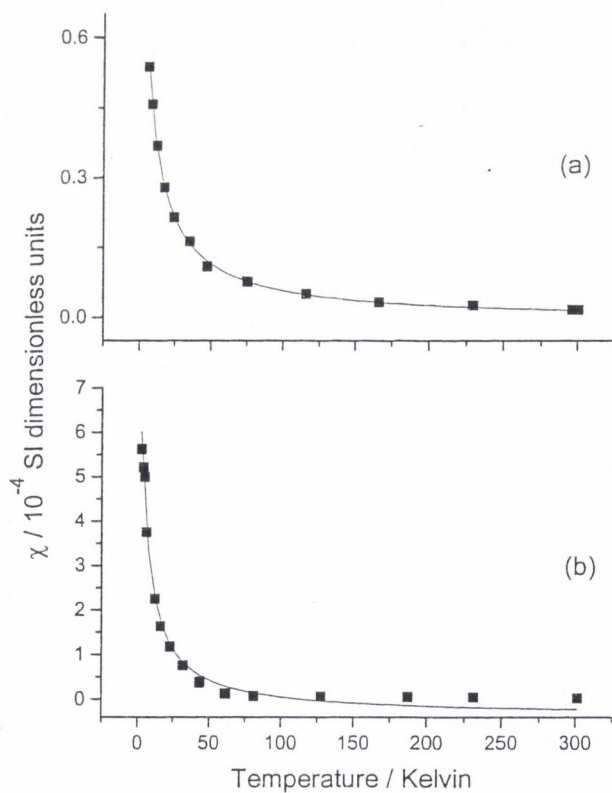


**Figure 6.7** Variation of susceptibility with T for (a) C320 and (b) C500. These samples show the (a) best and (b) worst fits to a modified Curie-Weiss law, as indicated by the solid line.

As can be seen from the table 6.2, the samples studied exhibit Weiss temperatures of  $\approx 10\text{K}$ , much greater than those of Matthews' [18] samples, and that predicted by exchange [19]; however, it should be noted that some of these temperatures are derived from somewhat dubious fits, as can be seen by the indicated errors, and the fit for C500, shown in figure 6.7(b).

Fanchini *et al.* [12] observed in sputtered amorphous carbon nitride a susceptibility that was Curie-like at 'high' temperatures and Pauli-like (i.e. independent of temperature) at 'low' temperature – they placed the transition between these states at a temperature between 77K and 295K. This group supposed that the unpaired spins in the film, being close to free-electron conditions, acted as a Fermi gas. The energy of the Fermi gas at 0K,  $U$ , is purely kinetic. Ashcroft and Mermin [20] give this energy as:

$$6.4 \quad U = \left( \frac{\hbar^2}{2m} \right) (3\pi^2 N_s)^{2/3}$$

Two extreme cases are then shown to occur: at high temperatures  $U \ll k_B T$  a Curie-like susceptibility is expected, and at low temperatures  $U \gg k_B T$  most electrons are paired in the ground state and a Pauli-like behaviour is expected [20]. Fanchini *et al.* [12] showed that the value for  $U$  for their samples would be  $\sim 240\text{K}$ . For the samples studied here, however, with a higher spin concentration,  $U \sim 1000\text{K}$ ; thus this model cannot account for the observed transition at  $\approx 13\text{K}$ .

### 6.3.3 Conclusions

Measurements of the intensity of the EPR line as a function of temperature (5-300K), at both X- and W-band, show that for some samples the susceptibility is essentially Curie-like, whereas for other samples the susceptibility deviates from the Curie law and becomes less dependent on temperature at  $T \approx 13\text{K}$ .

Experimental and instrumental errors are discussed, and various models are proposed to account for the deviation. It is suggested that the most plausible explanation is that amorphous carbon contains clusters of spins that locally order at  $T \approx 13\text{K}$ , and this is further supported by SQUID magnetometer measurements that show a hysteresis loop at 5K. However, further work could be done to ascertain the level of ferromagnetic impurities in the films and substrates.

## 6.4 Line Broadening and Narrowing Mechanisms

### 6.4.1 Introduction

EPR has been used to provide detailed insight into the nature of defects in a-Si:H [21]. With the advent of a-C as an electronic material, it is crucial that the defects in the material and the full nature of the paramagnetic centres are addressed [22]. An important aspect of this is the nature of line-broadening and narrowing mechanisms and relaxation times. A number of groups [3, 18, 22-24] have shown that linewidths and relaxation times of the EPR detected resonance may be related to spin hopping and/or exchange.

In this section I investigate the relaxation times and linewidths of EPR centre in a-C films with a range of structures and amorphous carbon nitride films with a variety of nitrogen concentrations. Particularly, I examine how these parameters change with temperature and microwave frequency, and present various models to explain these trends.

## 6.4.2 Experimental

Relaxation time measurements were carried out at X-band at room temperature (290K),  $\approx 100\text{K}$  and  $\approx 30\text{K}$  (not less than this, to avoid the region where spin ordering may be present, see sections on susceptibility and anisotropy). All samples studied (B1, B2, C100A, C190, C320, C500, GR1, GR3 and GR4) seem to exhibit Lorentzian lineshapes, at least at these temperatures, so the standard method utilising the peak-to-peak height of the collected derivative can be used, in all cases, to calculate the relaxation time product  $T_1T_2$ , as detailed in chapter three.  $T_2$  is derived from the linewidth as shown in section 3.7.1 and thus  $T_1$  can be calculated. As microwave power is increased to saturate the signal, the incident microwaves may cause the sample temperature to increase. A sensor attached to the sample monitors the temperature, and any increase is counterbalanced by increasing the gas flow rate until the temperature once again stabilises at the required value.

For X-band the linewidths recorded are the measured peak-to-peak widths,  $\Delta B_{pp}$ , of the collected signal. For W-band, the lines are fitted to a mixture of dispersion and absorption; thus the half width at half maximum of the integrated signal,  $\Gamma$ , is found by the fit from equation 6.1. The equivalent peak-to-peak linewidth,  $\Delta B_{pp}$ , can then be derived from this width,  $\Gamma$ , using the relation [25] for Lorentzian lines

$$\Delta B_{pp} = \frac{2}{\sqrt{3}}\Gamma. \text{ The width of some of the more polymeric films is subject to}$$

increased uncertainties due to the presence of a line at  $g \approx 1.999$  related to phosphorus impurities in the silicon [26]. This is, in these films with the lowest defect densities, of comparable magnitude to the line related to the carbon defect.

## 6.4.3 Results

### 6.4.3.1 X-Band linewidths

The room temperature linewidths, both from X-band and W-band measurements, are summarised in table 6.3, below. (The values of EPR parameters used in this chapter may differ slightly from previously quoted figures for linewidth etc. as room temperature experiments were repeated on samples studied previously, to ensure continuity within the temperature dependence analysis). All films are described in greater detail in section 6.2. It is worth noting, however, that for the B- and C-series, the films are listed in order of increasing  $sp^2$  fraction, and for the GR-series in order of increasing nitrogen content.

Sample	Film type	Peak-to-peak linewidth $\Delta B_{PP}$ /G			Defect density, $N_V/10^{26} m^{-3}$
		X-band	W-band	Dipolar	
C100A	PLHC	10.6±0.4	11.6±1.0	17.2	2.1
C100B	PLHC	8.9±0.5	9.1±1.2	18.9	2.3
C190	DLHC	7.4±0.8	-	9.9	1.2
C320	DLHC	4.8±0.4	4.8±0.2	15.6	1.9
C500	DLHC/GLHC	3.8±0.3	3.6±0.1	37.8	4.6
B1	DLHC/GLHC	3.4±0.4	5.9±0.2	6.8	0.83
B2	GLHC	1.3±0.1	1.6±0.1	21.3	2.7
GR1	a-C:H	4.2±0.2	-	13.2	1.6
GR3	a-C:N:H	4.7±0.2	-	29.2	3.6
GR4	a-C:N:H	5.8±0.2	-	6.5	0.8

**Table 6.3** Room temperature EPR linewidths from X- and W-band measurements, and linewidth predicted from spin density assuming dipolar broadening alone

As can be seen, for the non-nitrogenated films the linewidth decreases as the fraction of  $sp^2$  bonded carbon increases. For all films there is only a slight increase in the width of the resonance line when the frequency of microwaves is increased by a factor of approximately ten, from X-band ( $\approx 9.5\text{GHz}$ ) to W-band ( $\approx 94\text{GHz}$ ).

$$4.1 \quad \Delta B_{pp}(\text{mT}) = 8.12 \times 10^{-21} N_V (\text{cm}^{-3})$$

From earlier chapters, equation 4.1 gives the linewidth predicted from the spin density assuming dipolar broadening alone. It should be noted that in all cases the linewidth remains lower than that predicted by this equation

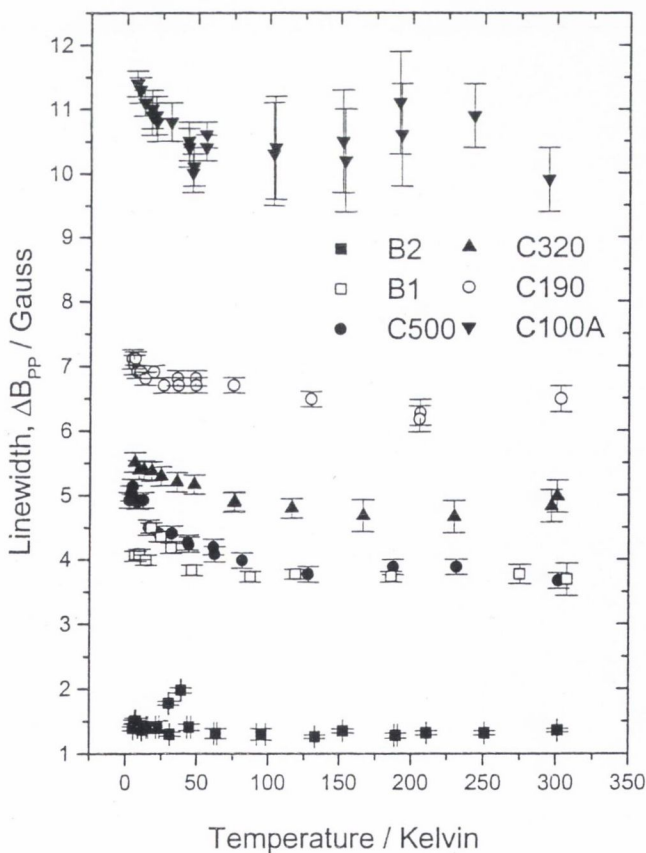


**Figure 6.8** X-band measurements of linewidth as a function of temperature.

Figure 6.8 shows the variation with temperature of the linewidth of the non-nitrogenated films. As is common in hydrogenated amorphous carbon [23] the linewidth increases with decreasing temperature, as opposed to the linewidth decreases seen by some researchers [22] in a-C. More specifically, the linewidth of the heavily ion implanted B2 sample increases only by  $<0.1\text{G}$ , except for a peak in width at about 30K, which possibly may be attributed to the superposition of another unresolved line. Most of the other lines show width increases of 1 to 2 G over the temperature range 5 – 300K, with the rate of increase more rapidly increasing at temperatures below  $\approx 100\text{K}$ .

#### 6.4.3.2 Relaxation times

Staying with X-band measurements, figure 6.9 shows spin – lattice relaxation times,  $T_1$ , for the a-C:H films. For purposes of clarity not all samples are plotted, full results are shown in table 6.4.

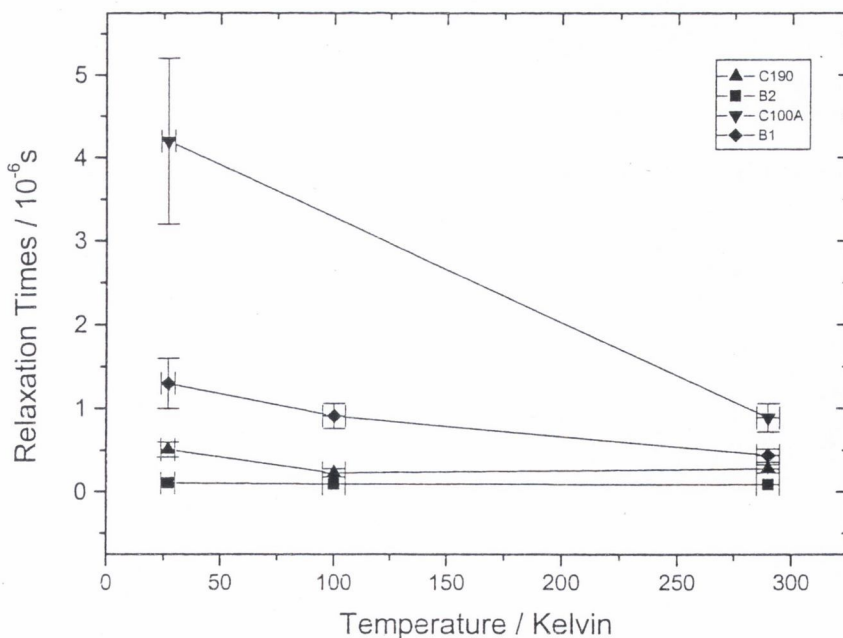


**Figure 6.9** Spin-lattice relaxation times,  $T_1$ , of selected samples, showing trend of slower relaxation at lower temperature dependent on film structure. C100A ( $\blacktriangledown$ ), B1 ( $\blacklozenge$ ), C190( $\blacktriangle$ ), B2( $\blacksquare$ ).

However, the figure 6.9 shows the general trends in the spin-lattice relaxation time.

The more polymer-like film C100A has the greatest lengthening in  $T_1$  over the decrease in temperature, from 300K to 30K, whilst the film, B1, with high  $sp^2$  content, has no change in  $T_1$ , within errors. Other samples show change in spin-lattice relaxation time over the temperature range within these extremes.

Sample	Relaxation times					
	$\approx 290\text{K}$		$\approx 100\text{K}$		$\approx 30\text{K}$	
	$T_1 / 10^{-7}\text{s}$	$T_2 / 10^{-8}\text{s}$	$T_1 / 10^{-7}\text{s}$	$T_2 / 10^{-8}\text{s}$	$T_1 / 10^{-7}\text{s}$	$T_2 / 10^{-8}\text{s}$
C100A	8.9±1.7	0.63±0.04	-	-	42±10	0.6±0.1
C190	2.8±0.5	1.0±0.1	2.3±0.5	1.1±0.1	5.1±0.9	1.0±0.1
C320	1.9±0.4	1.4±0.1	1.5±0.3	1.4±0.1	5.4±1.1	1.3±0.1
C500	1.6±0.3	1.7±0.1	0.79±0.22	1.6±0.1	3.2±0.6	1.6±0.1
B1	4.4±0.8	1.9±0.2	9.1±1.5	1.8±0.2	13±3	1.7±0.2
B2	0.90±0.19	4.9±0.5	0.96±0.25	5.4±0.5	1.08±0.28	3.8±0.3
GR1	2.4±0.4	1.4±0.1	3.6±0.6	1.3±0.1	5.9±1.1	1.1±0.1
GR3	2.6±0.5	1.1±0.1	7.2±1.1	1.1±0.1	12±2	1.0±0.1
GR4	6.3±1.1	1.0±0.1	20±3	1.0±0.1	71±13	0.9±0.1

**Table 6.4** Spin-lattice ( $T_1$ ) and spin-spin ( $T_2$ ) relaxation times, measured at X-band at approximately 30K and 100K and at room temperature.

The effect of film structure on the temperature dependence of relaxation times is more clearly pronounced in the nitrogenated samples, shown in table 6.4 and figure 6.10. The heavily nitrogenated GR4 (with 20at.% nitrogen incorporation [10]) has  $T_1$  lengthen by approximately an order of magnitude following the reduction in temperature, as shown in figure 6.10 – note the logarithmic scale on the Y-axis.

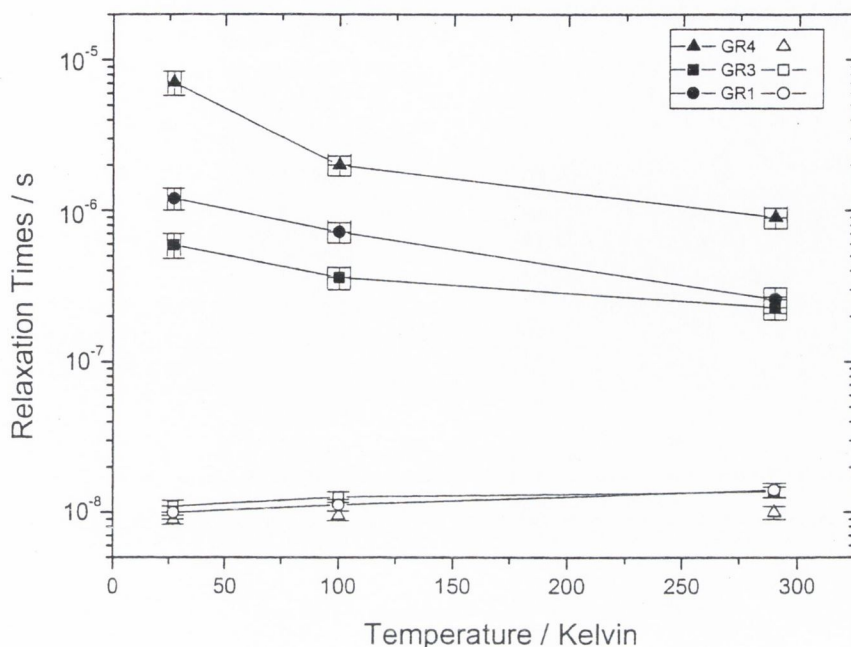


**Figure 6.10** Relaxation times of the nitrogenated series of samples as a function of temperature. Solid symbols indicate  $T_1$  values of GR1 (●), GR3(■), and GR4(▲) the spin-spin relaxation time,  $T_2$ , is indicated by the appropriate open symbols.

The figure also shows the spin-spin relaxation time,  $T_2$ , of each of the samples, which can be seen to decrease slightly with reduction in temperature. But, as with the C-series,  $T_2$  always remains at approximately  $1 \times 10^{-8}$  s.

#### 6.4.3.3 W-Band linewidths

Peak-to-peak linewidths can also be derived from W-band spectra. Polymer-like samples C100A and C100B, and B1, ion implanted with  $6 \times 10^{15}$  ions /cm<sup>3</sup>, with the broadest lines at room temperature, are indicated with open symbols in figure 6.11. As can be seen from the figure, the linewidths of these samples show only a slight

increase as the temperature is reduced from 295K to 5K, similar to the trends observed at X-band.

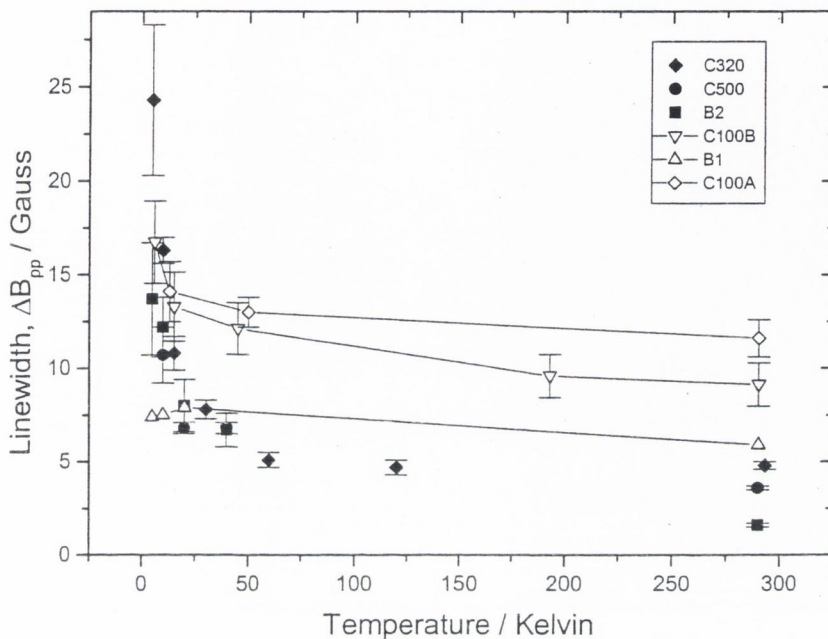


**Figure 6.11** Variation with temperature of W-band EPR linewidth. The open symbols indicate the more polymer-like films, and the film with lower dose ion implantation.

However, films grown with higher bias, C320 and C500, and implanted, B2, with  $2 \times 10^{16}$  ions/cm<sup>3</sup> (solid symbols in figure 6.11) exhibit, in contrast to X-band, strong temperature dependence of linewidth. The linewidth of C320 shows an increase from 4.8G at room temperature to 24.3G at 5K. Samples C500 and B2 show similar trends, the EPR lines increasing in width from 3.6G (290K) to 10.7G (10K) and 1.6G (290K) to 13.7G (5K) respectively (for sample C500 the linewidth could not be determined at 5K due to the presence of impurity signals as described in section 6.6).

## 6.4.4 Discussion

### 6.4.4.1 *g* value spread

By comparing data for X- and W-band EPR room temperature measurements, it can be seen that there is only a slight increase (if any) in the linewidths of all the films studied. Increasing the frequency from  $\approx 9.5\text{GHz}$  to  $\approx 94\text{GHz}$  would magnify ten-fold any contribution to the linewidth caused by a spread in *g* values of the carbon defect. The Lorentzian nature of the lineshape is consistent with homogeneous broadening, rather than a line that is made up of a number of constituent lines. This and the presence of only a slight change in width show that the carbon line, at  $g=2.0027(2)$ , has little or no linewidth component due to a spread in *g* values, as supported by a previous work [27].

### 6.4.4.2 *Exchange narrowing*

All the films studied, even the polymer-like amorphous carbons, show a linewidth that is less than that,  $\Delta B_{pp}^{\text{dip}}$ , predicted by dipolar broadening alone [2]. This suggests that the lines are narrowed by a form of motional narrowing, hopping or exchange [28, 29], as has been discussed in chapter 4 for the ion implanted films.

In the C-series of films, the degree of narrowing from the  $\Delta B_{pp}^{\text{dip}}$  becomes greater as the negative self-bias voltage of deposition is increased; the linewidth of the polymer-like C100A is narrowed from the predicted 17.2G to 10.6G (at X-band) whilst C500

has a predicted width of 37.8G which is more significantly narrowed to  $3.8 \pm 0.3$  G. In addition to the data on linewidths, spin-lattice relaxation is faster for films with higher bias. Remembering that the higher bias films have higher  $sp^2$  content, it is suggested that the narrowing in these samples, and the ion implanted and a-C:N films, occurs due to motional narrowing which increases as the  $sp^2$  cluster size and/or spin density increases, leading to a greater delocalisation and thus an increase in overlap of electron wavefunction, leading to greater exchange interaction [15, 16, 28, 29]. The fast relaxation times support this [28-31].

Goldsborough *et al.* [30], using a model proposed by Bloembergen and Wang [32] and measurements on DPPH and other radicals, show that where exchange is the dominant interaction the spin-lattice relaxation time,  $T_1$ , is independent of temperature. Lines where relaxation is dominated by phonon-induced processes of course show temperature dependence of relaxation times. Alger [31] shows that  $T_1$  is shorter and increases less with decreasing temperature for lines where relaxation is governed by exchange.

My measurements show a spin-lattice relaxation time independent of temperature for the highly narrowed line of sample B2, with the temperature dependence of  $T_1$  increasing for films with less narrowing. All of this supports the theory that exchange interaction becomes dominant in determining the EPR line width as the  $sp^2$  fraction is increased.

Measurements on the nitrogenated films show that addition of nitrogen reduces the line narrowing and increases the dependence of relaxation times on temperature. This

suggests that exchange becomes less important as the nitrogen content of carbon nitride films is increased. Investigations into nitrogenation of films described earlier imply that there is less disorder and buckling of  $sp^2$  regions as the nitrogen content is increased. This should lead to greater delocalisation [10]; however, this nitrogenation also reduces the defect concentration, therefore there is less wavefunction overlap and thus exchange plays a smaller part in relaxation processes.

#### 6.4.4.3 Hopping

Various groups [18, 23] have suggested that the EPR linewidth and its temperature dependence can be explained by hopping motion of electrons in the lattice.

I examine a model of variable range hopping of electrons between the isolated  $sp^2$  sites, odd-fold rings or clusters, assumed to be responsible for the EPR signal.

In the presence of pure dipolar broadening [2] and  $\omega_{\mu w} \tau_c \gg 1$  (where  $\omega_{\mu w}$  is the microwave frequency) the linewidth of the Lorentzian line can be expressed as:

$$6.5 \quad \Delta B_{pp} = \frac{2\Gamma}{\sqrt{3}} = \frac{2}{\sqrt{3}\gamma T_2} \approx \frac{2\gamma \bar{B}^2 \tau_c(T)}{\sqrt{3}}$$

where the spins experience a fluctuating field of average value  $\bar{B}$  in addition to the applied static field. The correlation time,  $\tau_c$ , is the reciprocal of the correlation frequency, which for variable range hopping (VRH) has a characteristic relation given by equation 6.6 [19].

$$6.6 \quad \frac{1}{\tau_c} = \omega_{\text{hop}} \approx \omega^0 \exp\left[-\frac{A}{T^{1/4}}\right]$$

where

$$6.7 \quad A \approx 1.7 \left[ \frac{\alpha^3}{k_B N(E_F)} \right]^{1/4}$$

Here  $N(E_F)$  is the density of states per unit volume per unit energy and  $\alpha$  is the inverse localisation length that characterises the exponential decay of the electron wavefunction at large distances [33, 34]. The most probable hopping distance,  $R$ , is then:

$$6.8 \quad R \approx [\alpha k_B T N(E_F)]^{-1/4}$$

Combining 6.5 and 6.6 then, gives:

$$6.9 \quad \ln(\Delta B_{\text{pp}}) = \ln\left(\frac{2\gamma\bar{B}^2}{\sqrt{3}\omega^0}\right) + \frac{A}{T^{1/4}}$$

The first term on the right hand side of 6.9 is independent of temperature; therefore the parameter  $A$  can be determined by the gradient of a linear fit to data on a plot of

$\ln(\Delta B_{\text{pp}})$  versus  $\frac{1}{T^{1/4}}$ .

Figure 6.12 (a) shows linewidth variation with temperature of sample GR1. Figure 6.12 (b-d) show  $\ln(\Delta B_{pp})$  plotted versus the inverse temperature to various powers. As can be immediately seen from the figure, the best linear fit is obtained with a plot of  $\ln(\Delta B_{pp})$  versus  $1/T^{1/4}$ , thus hinting at VRH processes.

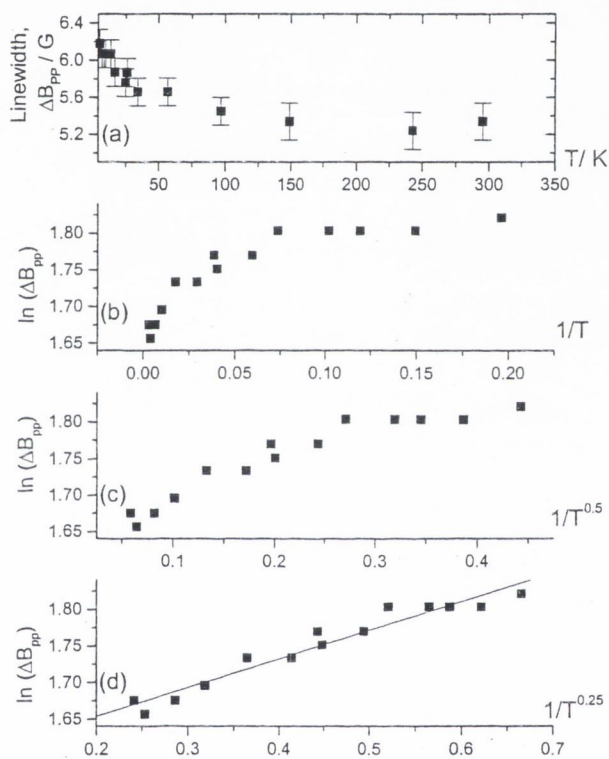


**Figure 6.12** Temperature dependence of X-band linewidth of GR1 (a) and variation of  $\ln(\Delta B_{pp})$  with (b)  $1/T$  (c)  $1/T^{1/2}$  and (d)  $1/T^{1/4}$ . A linear dependence of  $\ln(\Delta B_{pp})$  would suggest (b) floating bond migration (c) nearest neighbour hopping and (d) variable range hopping. The line in (d) is a linear fit with gradient  $0.39 \text{ K}^{0.25}$

Before examining this in closer detail, it is worth noting that  $\ln(\Delta B_{pp})$  does not vary linearly with  $1/T$  or  $1/T^{1/2}$ . The former suggests that neither floating bond migration [23] nor the one-dimensional hopping motion of a polaron defect, suggested by Matthews *et al.* [18], is appropriate. The latter shows that a modified nearest neighbour hopping process [35] is not a possible explanation for the temperature dependence of the EPR linewidth.

Equation 6.9, from the variable-range hopping model, gave a reasonable fit for the dependence of the linewidth on temperature for all the samples. Table 6.5 summarises values of parameter A from the fits, and the values for the localisation length,  $(\alpha)^{-1}$ , calculated from equation 6.7, taking the defect density as the density of states per eV.

Sample	Fit parameter, A		Localisation length, $(\alpha)^{-1}$ /nm	
	X-band	W-band	X-band	W-band
C100A	0.74±0.16	0.69±0.09	120±50	130±40
C100B	-	1.5±0.1	-	44±13
C190	0.24±0.03	-	750±220	-
C320	0.40±0.05	4.2±0.4	270±80	12±4
C500	0.60±0.05	3.2±0.5	120±40	13±5
B1	0.25±0.03	0.59±0.29	670±200	210±90
B2	0.27±0.06	5.2±0.9	410±120	8±3
GR1	0.39±0.03	-	300±90	-
GR3	0.46±0.04		180±60	-
GR4	0.79±0.09		150±40	-

**Table 6.5** Calculated values of the variable-range hopping parameter, A, and localisation length  $(\alpha)^{-1}$ , from X- and W-band temperature dependence of EPR linewidth.

From this table it can be seen that, for some of the samples, there is a frequency dependence of the parameter  $A$ . This parameter depends on the density of states and the localisation length, assuming that the hopping model can account for both X- and W-band linewidth variation with temperature. Whilst  $A$  for C100A is the same, within error, for both X- and W-band, the value of  $A$  for B2 increases by a factor of approximately twenty when the EPR frequency is increased from  $\approx 9.5\text{GHz}$  to  $\approx 94\text{GHz}$ . Neither the density nor the localisation length of the defects in a given sample, on which  $A$  depends, should be affected by the frequency of the microwaves to which they are subjected during EPR experiments. Further, these measurements show unphysical values, of the order of the film thickness, for the localisation length ( $\alpha^{-1}$ ). Fanchini *et al.* [23] show that the values for the average hopping distance,  $R$ , obtained from their similar experiment on one sample, are, at  $<0.1\text{\AA}$ , unphysical, too small to be related to the  $\approx 10\text{\AA}$  distance between defect sites.

### 6.4.5 Conclusions

Measurements of the EPR linewidth as a function of frequency, conducted on a variety of samples, show that at room temperature there is little or no increase in the width as the frequency is increased, thus supporting previous work [27] indicating that there is no contribution to the linewidth from a distribution of  $g$  values of the carbon line.

In the samples studied the width of the EPR line is less than expected for dipolar broadening alone, suggesting motional narrowing. The line is narrowed more substantially as the bias or ion implantation levels are increased, or as nitrogen content decreases. The motional narrowing then becomes more dominant with increasing  $sp^2$  content, and less prominent with increasing nitrogen.

Analysis of the temperature dependence of the resonance line, at both X- and W-band, superficially shows evidence of motional narrowing due to variable range hopping. However, closer examination shows that the parameters obtained are unphysical [23]. The X-band linewidth and relaxation times are independent of temperature for the ion implanted sample with highest  $sp^2$  content, which is indicative of exchange dominating the relaxation processes [30]. For films with lower  $sp^2$  content the X-band linewidth and relaxation times show a greater dependence on temperature, suggesting that exchange is less important in determining these properties. It is suggested that the dependence on temperature of the W-band linewidths, of which the highly narrowed films show a large increase with decrease in

temperature, can be explained in terms of the demagnetising field, which is discussed in greater detail in the following section.

In summary, there is no spread in  $g$  values in the carbon line. As the  $sp^2$  fraction increases, exchange becomes of greater prominence in determining the EPR linewidths and relaxation times. This is consistent with the model proposed by Robertson and O'Reilly [15, 16], where  $sp^2$  sites form clusters. As the  $sp^2$  content is increased, the cluster size increases; thus the electron becomes more delocalised, there is a greater wavefunction overlap, and therefore there is increased exchange.

## 6.5 Anisotropy and demagnetising factor

### 6.5.1 Introduction

A number of authors [5, 36] have observed that the  $g$  value of the resonance line in a-C(:H) has an angular dependence on applied field at low temperature. Druz *et al.* [5] suggest that the anisotropy in the  $g$  value observed in their ta-C and DLC films can be attributed to the demagnetising factor in the quasi-two-dimensional thin films. In this section I study films with a wide range of structures, at both X- and W-band, at a variety of temperatures, to search for and understand this phenomenon.

### 6.5.2 Resonance position versus orientation

Samples studied are the ion implanted B-series and PECVD C-series, as detailed in section 6.2. Some of the samples develop an anisotropy in the resonance position as the temperature is decreased. Although the resonance line retains a symmetric shape, on lowering temperature its position is shifted to higher fields when the external magnetic field,  $\mathbf{B}$ , is perpendicular to the film, and to lower fields when  $\mathbf{B}$  is parallel to the film.

Samples were rotated about an axis in the plane of the film. Figure 6.13 shows the resonance field,  $B_0$ , for sample B2, at a temperature of 9K, as a function of the recorded rotation angle,  $\phi'$ . Due to a slight misalignment  $\phi'$  differs slightly from the

angle,  $\phi$ , between the plane of the sample and the applied field (at  $\phi = 0^\circ$   $\mathbf{B}$  lies in the plane of the sample, and is perpendicular to this when  $\phi = 90^\circ$ ).

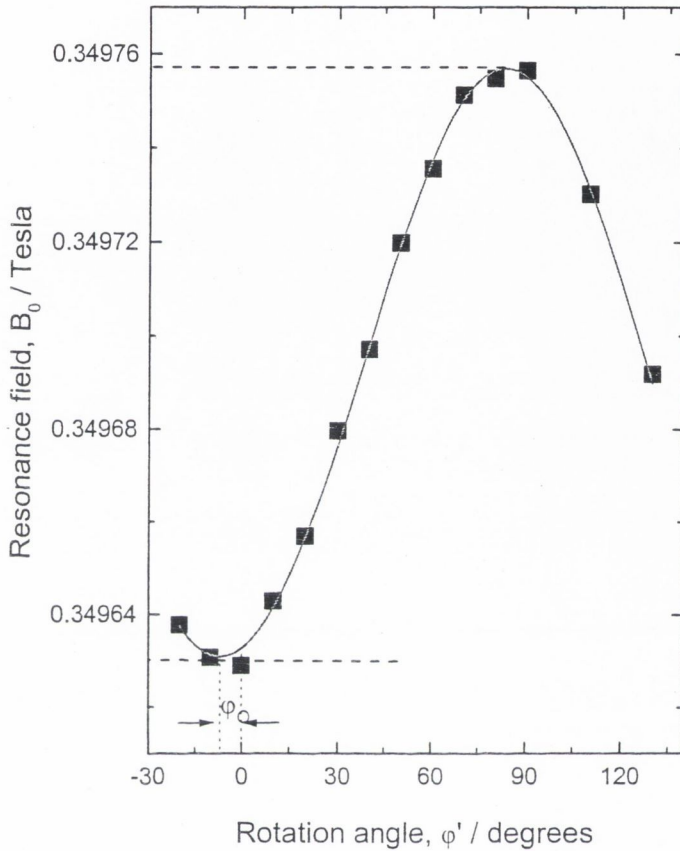


**Figure 6.13** Orientation dependence of resonance position of sample B2 at  $T \approx 9\text{K}$ . Smooth line shows fit from equation 6.11 with  $\phi' = (\phi + \phi_0)$ .

At X-band the changes in the applied field are only a few gauss or less. Due to slight instabilities in the field, the difference between the applied field,  $B_0(\phi)$ , at  $\phi = 0^\circ$  and  $\phi = 90^\circ$ ,  $\Delta B_{\text{ori}} = B_0(90) - B_0(0)$ , can be determined more accurately than  $B_0(90)$  or  $B_0(0)$  individually. For the orientation dependence shown in figure 6.13, to reduce the effects of this instability, a rapid scan rate and small range were used. The orientation of the sample was frequently returned to a previous value to check the repeatability of the measurement, and to ensure there was no drift in the measured value of the field.

### 6.5.3 Resonance shift versus temperature and spin concentration

Measurements were made of the X-band orientation dependence of resonance position as a function of temperature. Samples B2, C500 and C320 show that the shift in position  $\Delta B_{\text{ori}}$  increases as the temperature is reduced, as shown in figure 6.14. For samples B2 and C500 this shift is approximately proportional to  $1/T$ ; for C320 this proportionality is not clearly shown but the shifts are smaller and certainly still increase with decreasing temperature. The figure also shows the values of  $\Delta B_{\text{ori}}$  calculated from the data obtained by Druz *et al.* [5] for three of their samples, which also show  $\Delta B_{\text{ori}}$  to be proportional to  $1/T$ .

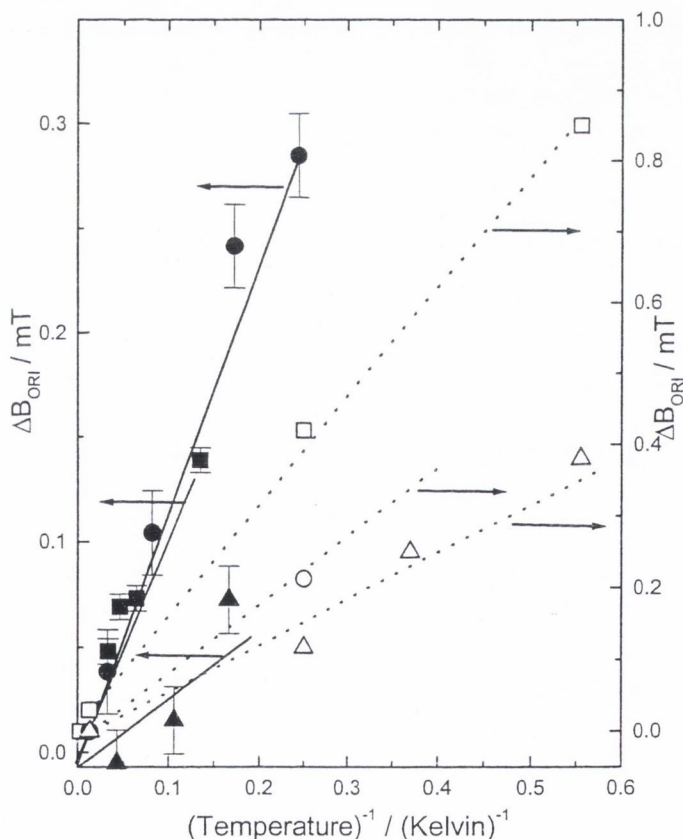


**Figure 6.14** X-band measurements of shift in resonance position for samples B2 (■), C500 (●) and C320 (▲) as a function of  $T^{-1}$ . Open symbols show data from Druz *et al.* [5]. Lines are guides to the eye.

The shifts, if any, for samples B1, C100A and C190 are small, and because of the larger linewidth are difficult to measure accurately. For all of these films the upper limit of the shift in resonance position,  $\Delta B_{\text{ori}}$ , is estimated as 0.12mT at 5K.

The W-band apparatus does not allow the rotation of the sample, which is fixed with the plane perpendicular to the applied magnetic field. As previously mentioned the system allows collection of spectra that are not just pure absorption, but contain some element of dispersion. For this reason the linewidth,  $\Gamma$ , and resonance field,  $B_0$ , are calculated from a fit to the spectra, given by equation 6.1. Samples B2, C500 and C320 again showed an increase in the value of the resonance field as the temperature was reduced. These shifts are larger than at X-band for the same temperature and are also approximately proportional to  $1/T$ , as shown in figure 6.15.

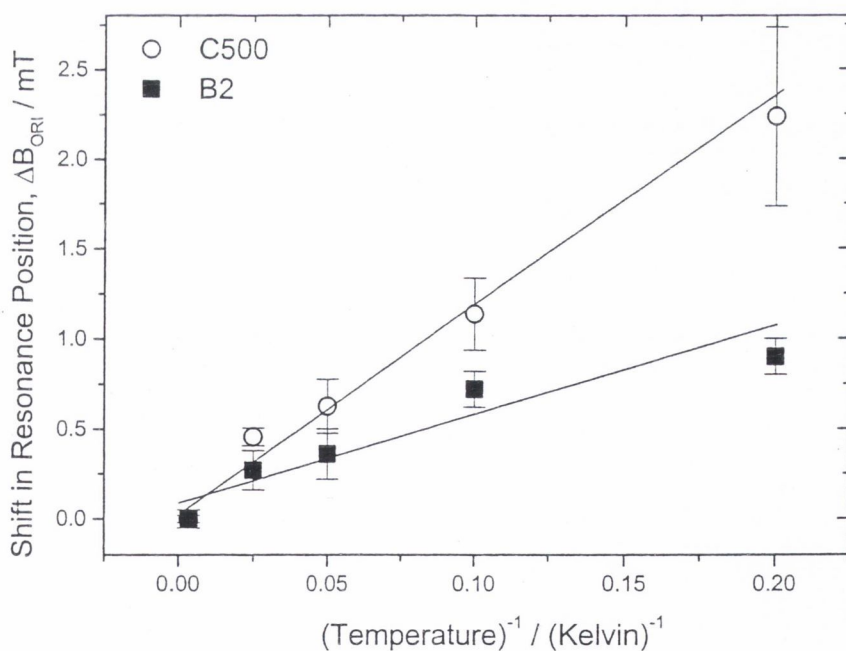


**Figure 6.15** W-band measurements of shift in resonance position for samples B2 (■) and C500 (○) as a function of  $T^{-1}$ . Lines are a guide to the eye. Zero shift for both samples is taken as the room temperature (290K) field position

No shift could be detected for samples C100A, C100B or B1. Upper limits of  $\Delta B_{\text{ori}}$  for these samples, as well as a summary of results are recorded in table 6.6

sample	Resonance Shift, $\Delta B_{\text{ORI}} / \text{mT}$		$N_{\text{v}} / 10^{26} \text{ m}^{-3}$
	X-band (5K)	W-band (10K)	
B1	$\leq 0.12$	$\leq 0.3$	0.83
B2	$0.19 \pm 0.03$	$1.1 \pm 0.3$	2.6
C100A	$\leq 0.12$	$\leq 0.6$	2.1
C100B	-	$\leq 0.5$	2.3
C190	$\leq 0.1$	-	1.2
C320	$\leq 0.06$	$1.3 \pm 0.4$	1.9
C500	$0.25 \pm 0.4$	$1.8 \pm 0.3$	4.6
*ta-C#2	0.45	-	28
*ta-C#4	0.40	-	26
*ta-C#9	0.17	-	18
*DLHC#1	0.13	-	11

**Table 6.6** Shift in resonance, with respect to room temperature value,

at X- and W-band, at 5K and 10K respectively.

\* indicates data from Druz *et al.* [5].

Druz *et al.* [5], in their measurements to 1.75K, observed a correlation between the resonance position anisotropy and spin density: as density increases so does  $\Delta B_{\text{ORI}}$  (expressed in their paper in terms of g-value). In the current work this correlation is less clear, but it is certain that the samples with the highest spin concentration (B2 and C500) exhibit the greatest shift in resonance as temperature is decreased.

The samples, B2, C320 and C500, which exhibit this shift in resonance position at W-band, also have a linewidth that increases with falling temperature. The peak-to-peak

width increases from 0.16 mT at 290K to 1.37 mT at 5K for sample B2, and from 0.36 mT at room temperature to 1.07 mT at 10K for C500. Whilst the linewidth of all samples studied increases with decreasing temperature, none of the other samples exhibits such a dramatic increase in width.

In summary, these measurements show a clear anisotropy in the resonance position occurring as the temperature is decreased. The resonant field is shifted to higher values when the plane of the film is perpendicular to the applied field, and to values lower than that at 290K when the field is parallel to the plane, following the angular dependence as shown in figure 6.13. This anisotropy is found to be approximately proportional to the EPR frequency (i.e.  $B_0$ ) and inversely proportional to temperature. Samples with the highest spin densities exhibit the greatest  $g$  value anisotropy, and also a large increase in linewidth with decrease in temperature.

#### 6.5.4 Discussion

In 1964 Svare and Seidel's [37] observations of the EPR lines of various paramagnetic salt crystals, showed, at low temperatures, an orientation dependence of the field position of resonance. This they attributed to shape-dependent demagnetising fields, and showed that a sample, treated as a system of spins, can become magnetised when aligned in a strong magnetic field at low temperature. Thus paramagnetic resonance can qualitatively behave in a similar manner to ferromagnetic resonance, where demagnetising fields are more usually encountered.

#### 6.5.4.1 Mathematical analysis of demagnetising factor

I now examine the demagnetising factor in detail to see whether this theory can explain the observed effects.

Assuming that the magnetisation,  $\mathbf{M}$ , of the film is uniform and is parallel to the external field,  $\mathbf{B}$ , - a good approximation in the present case since the film is amorphous and the demagnetising field is much less than  $\mathbf{B}$  - then with  $\mathbf{B}$  at an angle  $\varphi$  to the plane of the film the expression [7] for the ferromagnetic resonance frequency  $\omega$  becomes (in SI units)

$$6.10 \quad \omega = \gamma \left[ (B_0 - \mu_0 M \sin^2 \varphi)(B_0 + \mu_0 M \cos(2\varphi)) \right]^{\frac{1}{2}}$$

$B_0$  is the external field at resonance and  $\gamma$  is the gyromagnetic ratio. In our experiments  $\omega$  is fixed while the field is swept. Putting  $\omega = \gamma B_{00}$  where  $B_{00}$  is the resonance field in the limit  $M \rightarrow 0$  and assuming, as is the case of our experiments, that  $\mu_0 M \ll B_0$ , equation 6.10 gives

$$6.11 \quad B_0(\varphi) - B_{00} = \frac{1}{2} \mu_0 M (\sin^2 \varphi - \cos(2\varphi))$$

Equation 6.11 implies that

$$6.12 \quad B_0(90) - B_{00} = \mu_0 M \quad \text{and} \quad B_0(0) - B_{00} = -\frac{1}{2} \mu_0 M$$

so that

$$6.13 \quad \Delta B_{\text{ORI}} \equiv B_0(90) - B_0(0) = \frac{3}{2} \mu_0 M$$

In the case of the carbon films the anisotropy at room temperature is far too small to be observed, so  $B_{00}$  may be taken as the resonant field at room temperature. Of course one can define an effective  $g$  value,  $g_e$ , given by  $h\nu = g_e \mu_B B_0$  even though the actual  $g$  value of the paramagnetic centre is obtained from the local field which differs from  $B_0$  because of the demagnetising field. Therefore, from equation 6.12

$$6.14 \quad \frac{B_0(90) - B_{00}}{B_0(0) - B_{00}} = \frac{g_{e0} - g_e(90)}{g_{e0} - g_e(0)} \cdot \frac{g_e(0)}{g_e(90)} = -2$$

where  $g_{e0}$  is the  $g$  value obtained at temperatures where anisotropy is negligible.

In the present case, we assume that the magnetization is that of the carbon unpaired spins with  $S = 1/2$  and concentration  $N$  then:

$$6.15 \quad M = \frac{1}{2} N g \mu_B \tanh\left(\frac{g \mu_B B}{2kT}\right)$$

Since  $\tanh x \approx x$  for  $x \ll 1$  then in this limit

$$6.16 \quad \Delta B_{\text{ORI}} = \frac{3 \mu_0 N g^2 \mu_B^2 B}{2kT}$$

In the following sections I show that the model described mathematically here provides a good explanation of the data.

#### 6.5.4.2 Orientation dependence of resonance position

Equation 6.12 shows that the demagnetising field model predicts  $B_0(90) > B_{00}$  and  $B_0(0) < B_{00}$  (or equivalently for  $g$  values, with the inequalities reversed). This is observed by Druz *et al.* [5] and is consistent with the results described here. Further, equation 6.14 shows that the ratio  $\frac{B_o(90) - B_{oo}}{B_o(0) - B_{oo}}$  should be  $-2$ , if demagnetisation accounts for the observed effects. From the  $g$  values found by Druz *et al.* [5] this ratio was found to be in reasonable agreement, at  $-2.1$ ,  $-2.3$ ,  $-1.6$  for their samples as shown in figure 6.14.

The orientation dependence of the resonance field as predicted by equation 6.11 fits very well to the experimental angular dependence of  $B_2$ , as shown in figure 6.13. It should be noted in passing that a theory assuming an anisotropic  $g$  tensor also gives a good fit to the orientation dependence, but not to the other features discussed in this sub-section 6.5.4.

#### 6.5.4.3 Resonance shift versus temperature and spin concentration

As shown in figure 6.14 for X-band, and 6.15 for W-band, the shift in the magnetic field of the resonance position is approximately proportional to  $T^{-1}$ , as predicted by equation 6.16

Further, the resonance shift is approximately proportional to the magnetic field (multiplying the W-band measured  $[B_0(90)-B_{00}]$  by 1.5 to obtain  $\Delta B_{ORI}$ , according to

equations 6.12 and 6.13); again, this is in agreement with the predictions of equation 6.16.

This equation also shows that the shift in resonance position, if caused by a demagnetising field, should be linearly dependent on the spin concentration  $N$ . A predicted value of  $N$ , therefore, can be deduced from equation 6.16 and the resonance shift.

Sample	Spin concentration / $10^{26} \text{ m}^{-3}$		
	Calculated from X-band $\Delta B_{\text{ORI}}$	Calculated from W-band $\Delta B_{\text{ORI}}$	Measured, X-Band 290K
B1	$\leq 1.4$	$\leq 0.8$	0.83
B2	$2.3 \pm 0.4$	$2.8 \pm 0.8$	2.6
C100A	$\leq 1.4$	$\leq 1.5$	2.1
C100B	-	$\leq 1.3$	2.3
C190	$\leq 1.2$	-	1.2
C320	$\leq 0.73$	$3.4 \pm 1.0$	1.9
C500	$3.0 \pm 0.4$	$4.7 \pm 0.8$	4.6
*ta-C#2	5.5	-	28
*ta-C#4	4.8	-	26
*ta-C#9	2.1	-	18
*DLHC#1	1.6	-	11

**Table 6.7** Spin densities, measured and calculated from  $\Delta B_{\text{ORI}}$

\* indicates data from Druz *et al.* [5].

Table 6.7 shows the value of spin density calculated in this fashion, both for X- and W-band measurements, as well as the spin concentration calculated by comparing the room temperature X-band spectrum to that of a standard sample, as described earlier.

The table also gives  $\Delta B_{\text{ORI}}$  and  $N$  calculated from the work of Druz *et al.* [5]. For several samples no definite shifts could be detected, in which case only an upper limit is given.

From the table it can be seen that the calculated values of  $N$  from  $\Delta B_{\text{ORI}}$  observed in samples with a definite shift (B2, C500 and C320) agree reasonably well with the measured concentration. (Note that the absolute values of concentration are estimated to be accurate within  $\sim\pm 50\%$ , an increase from the experimental error due to uncertainty in the spin concentration of the standard used and in measurement of the same.) Also for sample B1 the upper limit of the calculated  $N$  is in agreement with the measured value. All the calculated  $N$  values for the samples of Druz *et al.* [5] are much smaller than the measured concentrations. However, their measured  $N$  values are unusually large – more often  $N$  values for ta-C are in the range  $(1-8) \times 10^{26} \text{ m}^{-3}$  [17, 38-40] in line with the calculated values; even the measured  $N$  value of  $11 \times 10^{26} \text{ m}^{-3}$  for the DLHC film is larger than the values of  $(1-5) \times 10^{26} \text{ m}^{-3}$  usually recorded [40]. Also, no definite shift could be measured for the more polymer-like films C100 A and C100 B, and the upper limit of the calculated spin concentration is in each case less than the measured  $N$ .

Finally, the spin concentration can be estimated from the fit to the orientation dependence of the sample, as shown in figure 6.13, using equations 6.11 and 6.15.

From this fit I calculate, for sample B2,  $N=2.6 \times 10^{26} \text{ m}^{-3}$ , in fortuitously good agreement with the measured  $N=2.6 \times 10^{26} \text{ m}^{-3}$ .

#### 6.5.4.4 Linewidth versus Temperature

For W-band measurements, the linewidths of samples B2 and C500 (with large shifts in resonance position) increase dramatically with decreasing temperature.

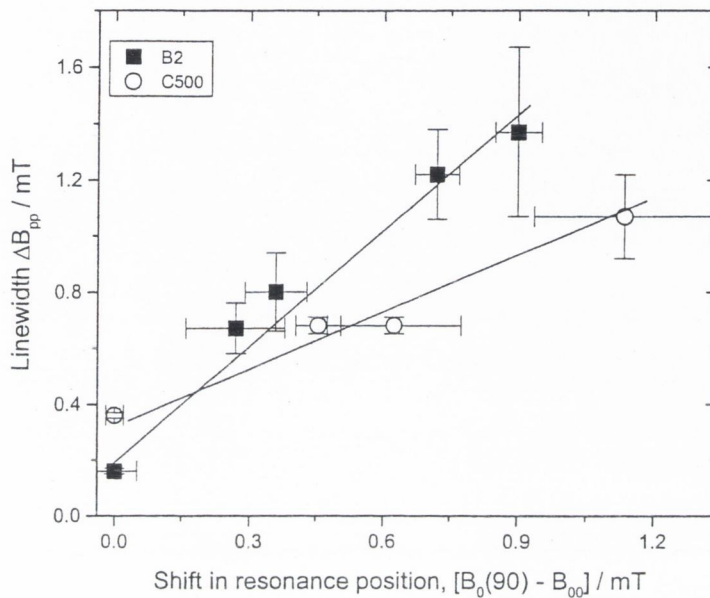


**Figure 6.16** Peak-to-peak linewidth versus shift in resonance position, from W-band measurements, for samples B2 (■) and C500 (○). Lines are guides to the eye.

Figure 6.16 shows a plot of linewidth versus the resonance shift  $\Delta B_{\text{ORI}}$ . From the figure it can be seen that the increase in linewidth may be linearly dependent on the resonant shift. This can be explained in terms of the demagnetising field varying in intensity throughout the sample, as noted by Svare and Seidel [37]; thus different regions of spins will come into resonance at various applied magnetic fields, effectively broadening the line. It can be seen that the increase in width is of comparable magnitude to the resonance shift.

### 6.5.5 Conclusions

Measurements on films of structure varying from DLHC to GLHC confirm the occurrence of anisotropy in the field position of the resonance at sufficiently low temperatures. A similar effect was previously observed by Druz *et al.* [5] and detailed analysis confirms their suggestion that this shift in resonance position is due to shape effects associated with the anisotropy in the demagnetising field.

Where the effect is observed, the magnitude can be explained in terms of the magnetization of the unpaired carbon electrons, although there could be contributions from spin ordering and/or magnetic impurities. However, for the PLHC samples no resonance shift is observed and the upper error limit is smaller than expected from the spin concentration of these films.

The increase in linewidth with decreasing temperature of the more graphite-like films can be attributed to variations of the demagnetising field throughout the sample.

## 6.6 Low temperature line shape

### 6.6.1 Introduction

H.J. von Bardeleben *et al.* [9] examined the EPR spectra of diamond-like and polymer-like a-C:H films at X, Q, and W-band ( $\approx 9, 30$  and  $94\text{GHz}$  respectively). Whilst detecting the commonly observed [1, 2, 29, 41] single Lorentzian line at X-band, von Bardeleben (vB) found anisotropic powder-like spectra at Q-band. Von Bardeleben claims that when the frequency was again increased, to  $94\text{GHz}$ , the total EPR spectrum for polymer-like and intermediate a-C:H, became fully resolved as a sum of two powder spectra. vB further argues that the diamond-like films exhibited a spectrum that could be deconstructed as a powder spectrum and a single Lorentzian line. The principal values of the g-tensors for these patterns are summarised in table 6.8, below. Von Bardeleben's experimental spectrum and powder pattern simulations are shown in figure 6.17 [9].

Sample (bias voltage)	Centre 1			Centre 2		
	$g_{\parallel}$	$g_{\perp}$	$g_{\text{avg}}$	$g_{\parallel}$	$g_{\perp}$	$g_{\text{avg}}$
DLC (-280)	2.0050	2.0025	2.0033	Isotropic $g=2.0025$		
Intermediate (-200)	2.0047	2.0028	2.0034	2.0100	2.0028	2.0052
PLC (-30)	2.0045	2.0028	2.0034	2.0092	2.0028	2.0049
Graphite	2.040	2.0028	2.0182	n/a		

**Table 6.8** Principal values of g-tensors for graphite [42] and for powder pattern fits

for the carbon defect in a-C, as proposed by von Bardeleben *et al.* [9].

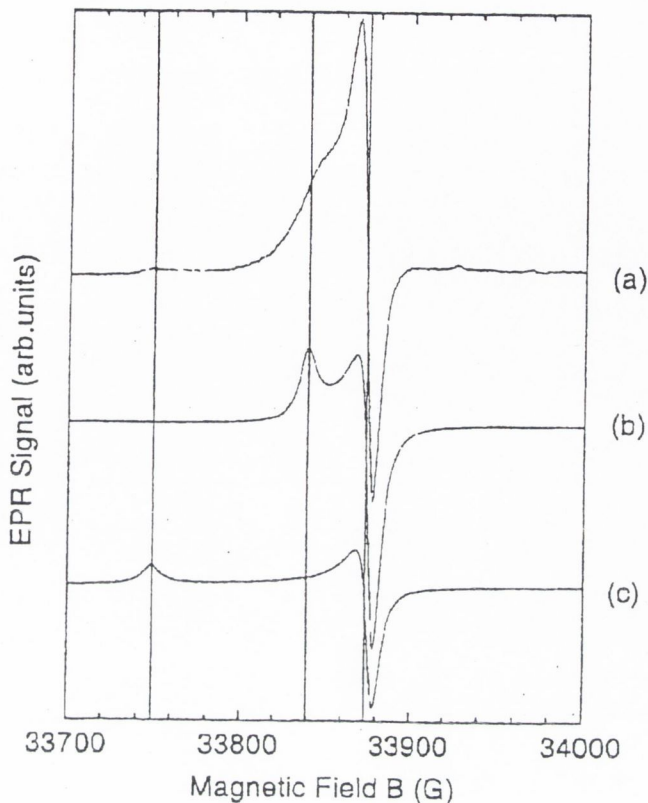


**Figure 6.17** Powder pattern simulations (b and c) and W-band resonance signal detected (a) by von Bardeleben *et al.* [9]. The g-tensor values are listed in table 6.8.

Von Bardeleben attributes the observed g-tensor values to localized  $\pi$  states in nanosized graphitic clusters, the sizes of which are correlated to the  $g_{\parallel}$  value of the g-tensor. It is also suggested that the single isotropic EPR line observed at X-band is due to strong exchange narrowing; the field anisotropy at W-band, ten times bigger than for measurements at X-band, would be too large to be averaged out by this effect. Work recently presented by von Bardeleben [43] suggests, however, that the interpretation given in reference [9] maybe incorrect for the diamond-like and intermediate samples.

## 6.6.2 Results and Discussion

The samples B1, B2, C100A, C100B, C320 and C500 studied at high frequency (W-band,  $\approx 94\text{GHz}$ ) cover a wide range of structures from the polymer-like C100A to diamond-like C320 to the highly graphitic, ion implanted B2. At room temperature all these samples displayed only a symmetric Lorentzian line at  $g \approx 2.0026(2)$ , examples of which are shown in figure 6.1. Whilst a spectrum resembling a powder pattern can be obtained, as discussed in section 6.2, this is due to the line being a combination of absorption and dispersion, as can be seen when the experimental line is fitted to equation 6.1. This is illustrated in figure 6.2.

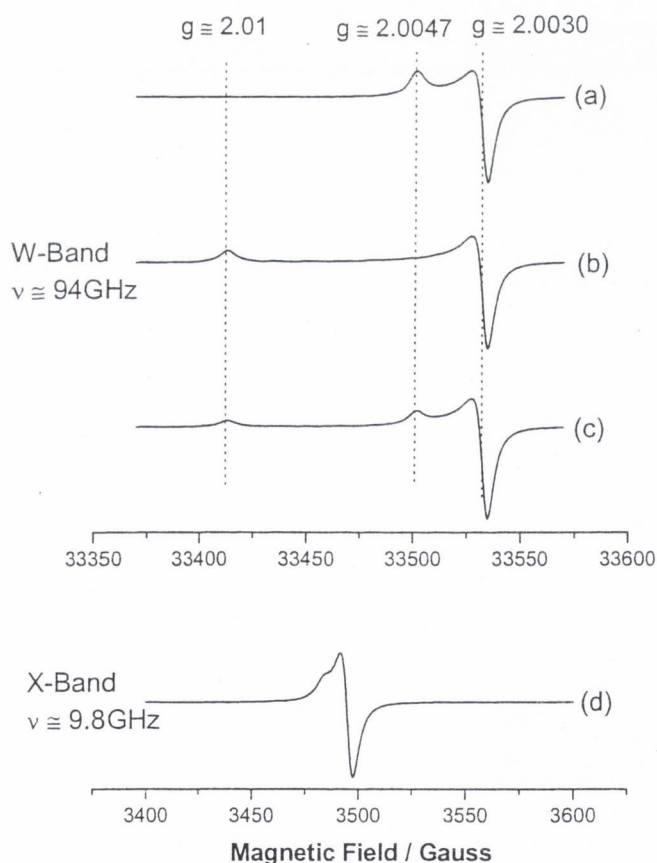


**Figure 6.18** Simulations of powder patterns for intermediate sample.

(a) W-band pattern with  $g_{\parallel} = 2.0047$  and  $g_{\perp} = 2.0028$  (b) W-band pattern with  $g_{\parallel} = 2.01$  and  $g_{\perp} = 2.0028$  with sums of these patterns at (c) W-band and (d) X-band

Figure 6.18 shows simulations of the powder patterns proposed by von Bardeleben *et al.* [9] and summarised in table 6.8. The sum of the spectra from these powder patterns at X-band is also shown in the figure. Whilst the X-band spectrum does not exhibit additional resolved peaks, it is easy to see that it is not a single Lorentzian line. Further analysis of these simulations shows that it is not possible to reproduce the experimental spectrum observed by vB using solely these two patterns. To provide a reasonable fit an additional symmetric line at  $g \approx 2.0028$  is needed. Indeed, von Bardeleben *et al.* [43] have recently reported measurements carried out on larger samples of the same films where the powder pattern spectra was *not* observed for the diamond-like or intermediate a-C:H.

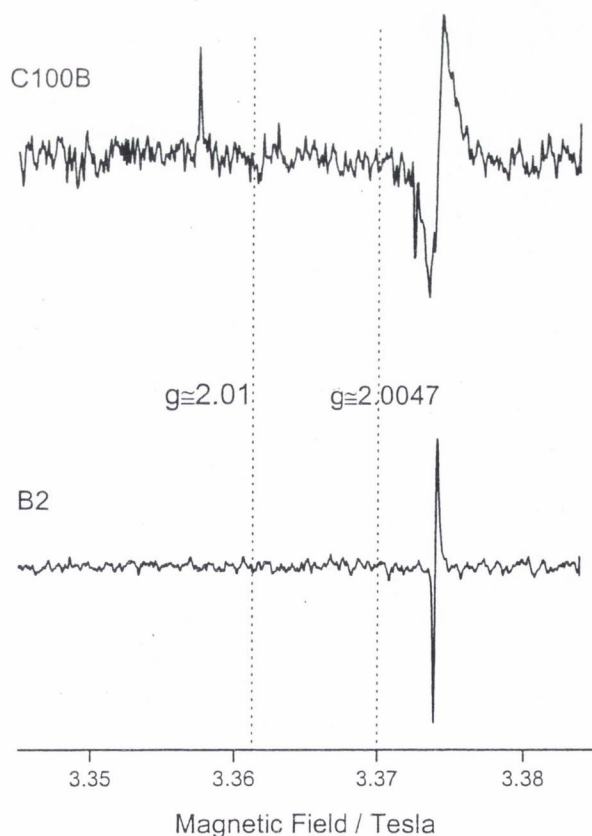


**Figure 6.19** Room temperature W-band spectra. 40mT sweep range shows flat baseline.

Figure 6.19 shows experimental room temperature spectra from samples C100B and B2, recorded over a range of 40 mT. It is clear that neither spectrum exhibits the additional features (a small peak at  $g \approx 2.01$  and the shoulder at  $g \approx 2.0047$  merging with the line at  $g \approx 2.0026$ ) that were observed by vB and simulated from powder patterns, as shown in the simulations in figure 6.18. No other features were seen: each of our samples exhibited only the single line at  $g \approx 2.0026(2)$ .

vB's W-band measurements were made at 4K, and it is conceivable that low temperature as well as high frequency is required to observe the powder patterns. Spectra for all the samples were therefore recorded at temperatures in the range 5-300K. None of the powder patterns reported by von Bardeleben were observed for any type of film at any temperature.

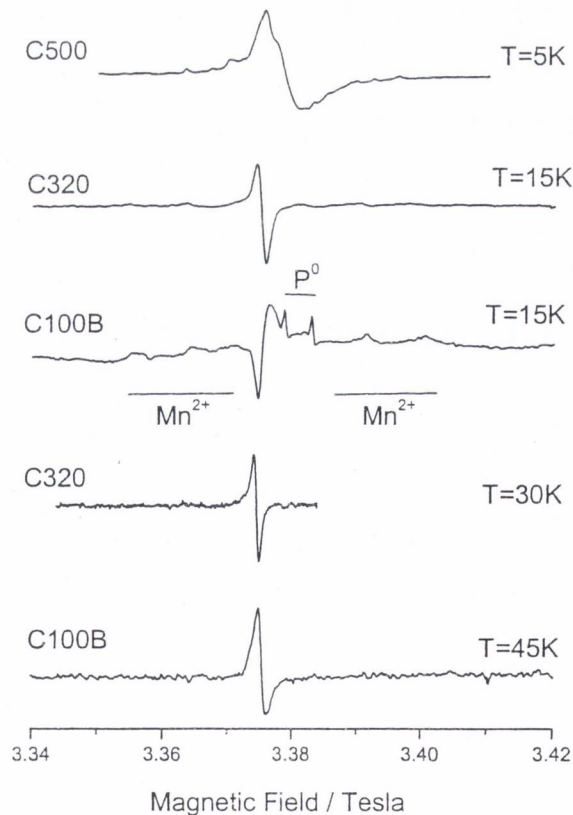


**Figure 6.20** Low Temperature W-band spectra for various samples. Impurity signals attributed to manganese and phosphorus, visible for  $T \leq 15K$ , do not appear at higher temperatures, as shown by spectra recorded at 30K and 45K.

It is possible that the presence of additional lines from impurities such as  $\text{Mn}^{2+}$ , visible at 5K, as shown in figure 6.20, may have obscured or distorted the signal. However, the impurity signal disappears as the temperature is increased to 45K, and once again a clean flat baseline is observed, with a single symmetric absorption line from carbon unpaired spins.

### 6.6.3 Conclusion

EPR measurements conducted at temperatures from 5K to 300K at both X-band ( $\approx 9.5\text{GHz}$ ) and W-band ( $\approx 94\text{GHz}$ ) showed only a single line from carbon unpaired spins, with no evidence of the additional features reported by von Bardeleben *et al.* [9].

## 6.7 Conclusions on the nature of defects

I have measured the EPR spectra of amorphous carbon films with a variety of structures, at a range of temperatures between 5K and 300K and at  $\approx 9.5$ GHz (X-band) and  $\approx 94$ GHz (W-band).

Room temperature EPR shows that there is little or no increase in the width of the resonance line, of any sample, when the microwave frequency is increased by a factor of ten from X- to W-band. This confirms earlier work [27] and shows that the resonance observed consists of one single symmetric line at  $g = 2.0026(2)$  and that there is no linewidth component due to a spread in  $g$ -values.

The temperature dependence of the susceptibility shows adherence to the Curie law at temperatures above  $\approx 13$ K. Below this temperature some deviation from this dependence may occur, possibly due to the onset of local magnetic ordering [4] of spin clusters [15, 16]. Further evidence of magnetic ordering comes from the presence of a magnetic hysteresis loop at 5K, although analysis of impurities within the film or substrate could show that this hysteresis is not due to carbon unpaired spins.

Measurements of the temperature dependence of the X-band EPR linewidth and relaxation times show that exchange interaction, rather than variable range hopping, becomes increasingly dominant as the  $sp^2$  content of the films is increased. Strong evidence for this comes from the highly “graphite-like” sample, B2, which shows no

variation of linewidth or relaxation time, within error, over the entire temperature range studied [30].

Measurements on DLHC and GLHC show that the position of resonance at low temperature displays a dependence on the orientation of the sample within the field. Detailed analysis shows that this anisotropy can be attributed to shape effects associated with the anisotropy of the demagnetising field, as suggested in a previous work [5]. In these films the effect can be explained in terms of magnetization of unpaired carbon electrons, though there could be contributions from spin ordering and /or impurities. The maximum effect in the more polymer-like samples is, however, less than would be expected from this analysis.

In contrast to the X-band measurements, at W-band the linewidths of the films with high  $sp^2$  content increase substantially as the temperature is lowered from room temperature to 5K (the strongest increase, from 4.8G to 24.3G, is seen in sample C320). This increase in width is correlated with, and is of approximately the same magnitude as, the shift in resonance position. Thus the broadening of the line is attributed to variation in the demagnetising field over the sample, causing a spread in effective  $g$  value and therefore an increase in the linewidth.

Finally, for all films at all temperatures and frequencies studied, the EPR signal due to unpaired carbon spins is observed to be a single symmetric line. No evidence was found of the powder patterns observed by von Bardeleben *et al.* [9].

## 6.8 References

- [1] M. Collins, R.C. Barklie, J.V. Anguita, J.D. Carey, S.R.P. Silva *Diamond Relat. Mater.* 9(2000)781
- [2] R.C. Barklie, M. Collins, S.R.P. Silva *Phys. Rev. B* 61(2000)3546
- [3] G. Fanchini, A. Tagliaferro, B. Popescu, E.A. Davis *J. Non-Cryst. Solids* 299-302(2002)846
- [4] D. Arčon, P. Cevc, R. Blinc, I. Pocsik, M. Koos, Z. Trontlj, Z. Jagličič in "*Molecular Nanostructures*" H. Kuzmany, J. Fink, M. Mehring, S. Roth Eds. Pub. World Scientific, Singapore (1998)533
- [5] B. Druz, I. Zaritskiy, Y. Yevtukhov, A. Konchits, M. Valakh, S. Kolesnik, B. Shanina and V. Visotski, *Materials Research Society Symposium Proceedings* 593(2000)249
- [6] A. Stesmans, B. Nouwen, D. Pierreux, V.V. Afanas'ev *Appl. Phys. Lett.* 80(2002)4753
- [7] C.J. Oates, F.Y. Ogrin, S.L. Lee, P.C. Riedi, G.M. Smith, T. Thomson *J. Appl. Phys.* 91(2002)1417
- [8] J. Robertson *Adv. Phys.* 35(1986)317
- [9] H.J. von Bardeleben, J.L. Cantin, A. Zeinert, B. Racine, K.Zellama, P.N. Hai *Appl. Phys. Lett.* 78(2001)2843
- [10] C. Godet, N.M.J. Conway, J.E. Bouree, K. Bouamra, A. Grosman, C. Ortega *J. Appl. Phys.* 91(2002)4154
- [11] H.J. von Bardeleben *Personal Communication to R.C. Barklie* (2002)
- [12] G. Fanchini, S.C. Ray, A. Tagliaferro, E. Laurenti *Diamond Relat. Mater.* 11(2002)1143

- [13] F. Giorgis, A. Tagliaferro, M. Fanciulli in *"Amorphous Carbon: State of the Art"* S.R.P.Silva, J. Robertson, W.I. Milne and G. Amaratunga eds. Pub. World Scientific, Singapore (1998)143
- [14] R. Czoch, A. Francik *"Instrumental Effects in Homodyne Electron Paramagnetic Resonance Spectrometers"* Pub. Ellis Horwood Ltd., Chichester (1989) Ch. 4
- [15] J. Robertson, E.P. O'Reilly *Phys. Rev. B* 35(1987)2946
- [16] J. Robertson *J. Non-Cryst. Solids* 198-200(1996)615
- [17] M.M. Golzan, D.R. McKenzie, D.J. Miller, S.J.Collocott and G.A.J.Amaratunga, *Diamond Relat. Mater.* 4(1995)912
- [18] M.J. Matthews, M.S. Dresselhaus, N. Kobayashi, T. Enoki, M. Endo, K. Nishimura *Phys. Rev. B* 60(1999)4749
- [19] N.F. Mott, E.A. Davis *"Electronic processes in Non-Crystalline Materials"* Pub. Clarendon Press, Oxford (1979)
- [20] N.W. Ashcroft, N.D. Mermin *"Solid State Physics"* Saunders, Philadelphia (1976)
- [21] M. Stutzmann *Philos. Mag. B* 60(1989)531
- [22] G. Fusco, A. Tagliaferro, W.I. Milne, J. Robertson *Diamond Relat. Mater.* 6(1997)783
- [23] G. Fanchini, A. Tagliaferro, D. Dasgupta, E. Laurenti, A.C. Ferrari, K.B.K. Teo, W.I. Milne, J. Robertson *J. Non-Cryst. Solids* 299-302(2002)840
- [24] C. Godet *Phil. Mag. B* 81(2001)205
- [25] J. Weil, J. Bolton, J. Wertz *"Electron paramagnetic resonance: Elementary theory and practical applications"* Pub. John Wiley & Sons, New York (1994)

- [26] A. Stesmans, *J. Magnetic Resonance* 76(1988)14
- [27] M. Hoinkis, E.D. Tober, R.L. White, M.S. Crowder *Appl. Phys. Lett*  
61(1992)2653
- [28] R.C. Barklie, M. Collins, J. Cunniffe, S.R.P. Silva *Diamond Relat. Mater.* 7  
(1998) 864
- [29] B. J. Jones, R.C. Barklie, R.U.A. Khan, J.D. Carey, S.R.P. Silva *Diamond  
Relat. Mater.* 10(2001)993
- [30] J.P. Goldborough, M. Mandel, G.E. Pake *Phys. Rev. Lett.* 4(1960)13
- [31] R.S. Alger “*Electron Paramagnetic Resonance Techniques and Applications*”  
Pub. John Wiley & Sons, New York (1968)
- [32] N. Bloembergen, S. Wang *Phys. Rev.* 74(1954)72
- [33] R.A. Street “*Hydrogenated Amorphous Silicon*” Pub. Cambridge University  
Press (1991)
- [34] R. Zallen “*The Physics of Amorphous Solids*” Pub. John Wiley & Sons, New  
York (1983)
- [35] H. Yokomichi, K. Morigaki *J. Non-Cryst. Solids* 266-269(2000)797
- [36] V.V. Afanas'ev, A. Stesmans, M.O. Andersson *Phys. Rev. B* 54(1996)10820
- [37] I. Svare, G. Seidel *Phys. Rev.* 134(1964)A172
- [38] E.G. Gerstner, P.B. Lukins, D.R. McKenzie, D.G. McCulloch *Phys. Rev. B*  
54(1996)1450
- [39] M. Chhowalla, J. Robertson, C.W. Chen, S.R.P. Silva, C.A. Davis, G.A.J.  
Amaratunga *J. Appl. Phys.* 81(1997)139
- [40] K.B.K. Teo, A.C. Ferrari, G. Fanchini, S.E. Rodil, J. Yuan, J.T.H. Tsai, E.  
Laurenti, A. Tagliaferro, J. Robertson, W.I. Milne *Diamond Relat. Mater.*  
11(2002)1086

- [41] R. C. Barklie *Diamond Relat. Mater.* 10(2001)174
- [42] G. Wagoner *Phys. Rev.* 118(1960)647
- [43] H.J. von Bardeleben, J.L. Cantin, K. Zellama, A. Zeinert *Diamond Relat. Mater.* Submitted (2002)

## *Chapter 7*

### *Other Experiments*

Scribimus indocti doctique poemata passim.

Atque inter silvas Academi quaerere verum.

Skilled or unskilled, we all scribble poems.

And search for truth in the groves of Academe.

-Horace

## 7. Other Experiments

This chapter describes a number of sets of experiments that do not fit under the categories of the previous three chapters. Here I examine nitrogen inclusion in tetrahedral amorphous carbon (ta-C), and the possibility of defects in such films being concentrated in an  $sp^2$ -rich surface layer. FCVA grown ta-C is studied, concentrating on the EPR characteristics as a function of substrate temperature, to determine whether defect signal exhibits the same sharp transition observed in the  $sp^2$  content.

Also examined are the EPR signals from PECVD a-C:H films as a function of rf-power, to assess continuity of manufacture, and as a preliminary characterisation for field emission studies. Diamond-like carbon films of different thicknesses are studied to examine the depth profile of defects in amorphous carbon thin films, with the aim of assessing the validity of the often-used assumption of a uniform distribution of defects throughout the film.

## 7.1 Defect location and concentration in ta-C and ta-C:N

### 7.1.1 Introduction

The material under study in this section is tetrahedral amorphous carbon, in both its nitrogenated (ta-C:N) and un-nitrogenated (ta-C) forms, grown by filtered cathodic vacuum arc (FCVA) under the supervision of Prof. J. Robertson of the Department of Engineering at the University of Cambridge. This highly tetrahedral form of amorphous carbon contains up to 85%  $sp^3$  bonded carbon and is distinguished from other diamond-like carbon (DLC) films by the absence of hydrogen. ta-C has a number of technologically valuable features such as high hardness, low friction coefficient and chemical inertness. [1]

In this section I use EPR to examine the effect of varying the bias voltage and nitrogen content on the population and nature of defects in the ta-C(:N) films. This work and previous studies [2] show that ta-C films exhibit narrow EPR lines, with width much less than that from pure dipolar interaction alone. This narrowing has been propounded in previous chapters as motional or exchange narrowing due to delocalisation caused by clustering of  $sp^2$  defect sites. However, these films contain a high proportion of  $sp^3$  bonded carbon, so this explanation of narrowing cannot be applied here. Recent studies [3, 4], though, have shown that FCVA grown ta-C has an  $sp^2$ -rich surface layer; thus if defects are concentrated in this region, then the narrow EPR lines exhibited would be expected from the theory outlined. Films

were studied as-grown and with the surface layer removed to examine the relative concentration of defects within the bulk and at the surface.

### 7.1.2 Experimental

ta-C films were grown with a background pressure of  $7 \times 10^{-7}$  mBar to a thickness of approximately 900Å. The incident ion energy was changed by varying the bias voltage. Films were deposited with bias voltages of 0, -100 and -300V; samples are labelled as 1/1, 1/2 and 1/3 respectively.

ta-C:N films were grown with a bias voltage of -80V. The nitrogen content was changed from approximately 0.06 at.% to 28 at.% by varying the nitrogen pressure (see table 1), and is calculated from a formula taken from a previous work [5] assuming an ion energy of 100eV (taken from the bias voltage and the initial ion energy of 20eV [5]). Substrates of p-type silicon with resistivity between 4.7 kΩ cm and 6.6 kΩ cm were used for all films.

Sample	N <sub>2</sub> Pressure / mBar	Deposition time	Nitrogen Content / at. %
2/1	$4 \times 10^{-6}$	5'	0.062
2/2	$4 \times 10^{-5}$	5'40"	0.50
2/3	$4 \times 10^{-4}$	6'10"	3.9
2/4	$3.5 \times 10^{-3}$	7'	28

**Table 7.1** Details of experimental conditions of studied ta-C(:N) films grown by FCVA method

A previous study [3] has shown that a surface layer of  $sp^2$  bonded carbon, related to the interaction of bombarding ions with the growing film, is present in tetrahedral amorphous carbon films grown by FCVA. EELS studies [4] show this layer to be of order 1nm thick.

Following initial EPR measurements, the films were plasma-etched in oxygen with a flow rate of 100sccm for eight seconds, thus removing the top layer of approximately 1 - 2nm of film, allowing the study of the bulk film with high proportion of  $sp^3$  bonded carbon, with and without the presence of the  $sp^2$  rich surface layer.

Electron paramagnetic resonance (EPR) measurements were carried out, pre- and post- etching, at room temperature, using our standard X-Band experimental set-up, with calibrations and analysis as previously described.

The coverage of these films on the substrates is not total and for some samples is estimated to be as low as 70%. The figures given in this section take account of this factor, and the inherent uncertainty within, as is necessary for comparing data from different samples. However, when comparing etched and as-grown films this coverage factor does not need to be included, thus the error range of the data is likely to be considerably reduced.

### 7.1.3 Results and discussion

All samples exhibited a single Lorentzian EPR line at  $g=2.0027(1)$ , with no visible fine or hyperfine structure present. Results for areal spin density,  $N_A$ , that is the total defect density divided by the area of one face of the sample that is covered by film, and linewidths are given in table 7.2, below.

Series/ sample	$\Delta B_{pp} / G$	$N_A / 10^{15} \text{cm}^{-2}$
1/1	2.7 (1)	4.8±1.0
1/2	3.8 (1)	4.1±1.0
1/3	3.7 (1)	4.8±1.1
2/1	3.8 (2)	5.4±1.9
2/2	3.7 (1)	4.4±1.0
2/3	3.6 (1)	3.9±0.9
2/4	3.0 (1)	2.0±0.6

**Table 7.2** EPR linewidth and spin density for as-grown films of studied ta-C(:N) films grown by FCVA method

#### 7.1.3.1 Un-etched ta-C films

The areal defect density,  $N_A$ , changed little (within errors) with the varying deposition ion energy of the three ta-C films. As the films are assumed to be approximately equal in thickness at around 900Å, they each have a volume defect density of  $N_V \approx 5.1 \times 10^{20} \text{cm}^{-3}$ .

The peak-to-peak linewidth,  $\Delta B_{pp}$ , of the resonance from the zero volt bias sample is, at 0.27(1) mT, slightly lower than the 0.37(1) mT of the higher incident ion energy films. This may be attributable to motional narrowing due to a greater  $sp^2$  content ( $sp^3$  content is at a maximum at an incident ion energy of order 100eV [6]) or due to deviation of the thickness of the film from the assumed value. For a given  $N_A$ , a thicker film would have a smaller volume defect density, implying that the linewidth due to dipolar interactions alone (from equation 4.1) would be narrower than for the other films, without the need to invoke exchange or motional narrowing.

### 7.1.3.2 Un-etched ta-C:N films

The areal defect density of the ta-C:N films, as shown in figure 7.1(a) decreases gradually with increasing nitrogen content from  $(5.4 \pm 1.9) \times 10^{15} \text{ cm}^{-2}$  for 0.06 at.% N content to  $(2.0 \pm 0.6) \times 10^{15} \text{ cm}^{-2}$  for 28 at.%. This reduction of defect concentration with increasing nitrogen content has been previously recorded [7] and shown in chapter five and may be due to a donor electron from the nitrogen pairing up with the initially unpaired electron of the paramagnetic defect, making it unobservable by EPR. It should be noted, however, that the increase in g-value with increasing nitrogen content reported by Barklie *et al.* [7] in their work on a-C:H was not observed here. The linewidth of the resonance also decreases: from 0.38 mT for 0.06 at.% N to 0.36 mT for 3.9 at.% and finally to 0.30 mT for the film containing 28 at.% N. This may be related to the decrease in defect density, or may be partially due to the dramatic decrease in  $sp^3$  fraction (from ~80% to <40%) observed for films with nitrogen content above 9 – 12 % [9, 10]. This may result in more, or

larger,  $sp^2$  clusters thus leading to motional narrowing of the EPR line, as described in previous sections and other studies [11].

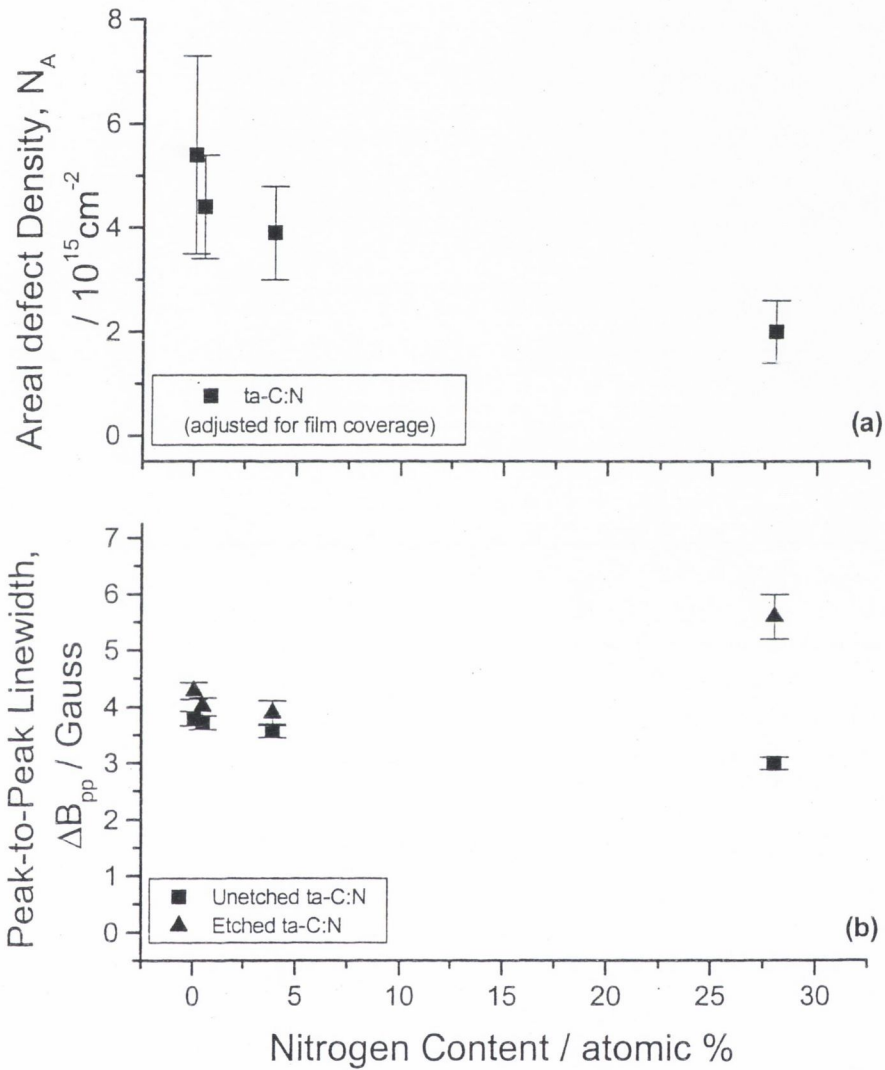


**Figure 7.1** Variation with nitrogen content of (a) areal defect density and (b) peak-to-peak linewidth, showing data for as-grown and oxygen etched films.

It is, however, thought that the increased  $sp^2$  fraction of a film due to increased nitrogen content leads to a wide range of  $sp^2$  cluster sizes [5] which may, therefore, be less effective in causing the wavefunction overlap, and thus motional narrowing, seen in previous studies [11].

### 7.1.3.3 $sp^2$ surface layer, etched samples

It was thought that the lack of anything but a small variation in EPR signal between the samples might have been due to the formation in each sample of an  $sp^2$  bonded surface layer, as has been previously proposed [3]. This hypothesis was supported by the fast spin-lattice relaxation times ( $T_1 \sim 5 \times 10^{-8}$  s) measured for each of the samples, which may imply  $sp^2$  clustering [11].

Series / Sample	$\Delta B_{pp} / G$		$N_A / 10^{15} \text{cm}^{-2}$	
	As - Grown	Etched	As - Grown	Etched
1/1	2.7 (1)	3.3 (1)	$4.8 \pm 1.0$	$5.0 \pm 1.0$
1/2	3.8 (1)	4.0 (2)	$4.1 \pm 1.0$	$4.0 \pm 0.9$
1/3	3.7 (1)	3.7 (3)	$4.8 \pm 1.1$	$4.9 \pm 1.1$
2/1	3.8 (2)	4.3 (2)	$5.4 \pm 1.9$	$4.6 \pm 1.0$
2/2	3.7 (1)	4.0 (2)	$4.4 \pm 1.0$	$4.0 \pm 0.8$
2/3	3.6 (1)	3.9 (2)	$3.9 \pm 0.9$	$3.7 \pm 0.8$
2/4	3.0 (1)	5.6 (4)	$2.0 \pm 0.6$	$1.8 \pm 0.4$

**Table 7.3** EPR linewidth and spin densities for as-grown and etched films. Sample 1/3 is not etched; experimentation on the as-grown film is repeated as a control.

The top 1-2 nm of each of the films (except that of the un-nitrogenated film deposited with bias voltage of 300V, which was kept as a control) was removed by etching in an oxygen plasma, as described earlier. EPR studies were also conducted

after the etching process was completed. There seems to be a slight decrease in the areal defect density of the films (understandable as some of the film has been removed). The values are, however, within errors of the EPR measurements taken from the as-grown samples, as shown in table 7.3. This shows that the  $sp^2$  surface layer does not contain a number of defects disproportionate to its thickness, despite the narrow EPR lines that suggest unpaired spins located in  $sp^2$  rich regions.

In each of the films etched there is an increase in the peak-to-peak linewidth of the resonance signal, as shown in figure 7.1(b) and table 7.3. In the un-nitrogenated films, and films with nitrogen content  $\leq 3.9\text{at.}\%$  this increase is of the order 10%, and may be attributable to incorporation of the oxygen (which has a magnetic moment) within the film. Hoinkis *et al.* [12] have observed, for amorphous hydrogenated carbon, an increase in linewidth with no change in defect density when the films were exposed to oxygen. For the film with a calculated 29at.% nitrogen the increase in linewidth is much more dramatic, from 0.30(1) mT to 0.56(4) mT. This broadening may also be due to incorporation of oxygen, the greater  $sp^2$  content of the film causing the effects to be different from the other films studied.

### 7.1.4 Conclusions

The EPR measurements confirm that increasing the nitrogen content of the ta-C:N films causes a decrease in defect density (from  $(5.4 \pm 1.9) \times 10^{15} \text{cm}^{-2}$  for 0.06 at.% N to  $(2.0 \pm 0.6) \times 10^{15} \text{cm}^{-2}$  for 28 at.% N for as-grown samples) with an accompanying narrowing of the resonant peak-to-peak linewidth (from  $0.38 \pm 0.1$  mT to  $0.30 \pm 0.1$  mT for the respective nitrogen contents detailed above). Etching the films in an oxygen plasma resulted in a decrease in defect density consistent with the amount of material removed assuming uniform distribution of defects. Thus, although narrow EPR lines and fast relaxation times suggest that defects are located in regions of  $\text{sp}^2$  bonded carbon, the  $\text{sp}^2$  rich surface layer does not contain a number of defects disproportionate to its thickness. The peak-to-peak linewidth of the resonant signal increased following this oxygen etching. For films with zero to 3.9 at.% nitrogen the increase was approximately 10%, however, the linewidth of the film with a calculated 28 at.% N increased by  $87 \pm 9$  %. The broadening of the resonance line is attributed to the incorporation of oxygen into the film; the difference in incremental factors may be due to the difference in structure caused by the quantity of nitrogen incorporated within the film.

## 7.2 Influence of substrate temperature on defects in tetrahedral amorphous carbon (ta-C) films

### 7.2.1 Introduction

This section also concentrates on tetrahedral amorphous carbon (ta-C) - characterized by a high percentage (~85%) of diamond-like  $sp^3$  bonding. ta-C films can be deposited from carbon ions with energies ranging from 30 to 600eV.

Previous studies [1, 2, 13] on the variation of film characteristics as a function of ion energy and substrate temperature have shown that the mechanical properties of the films are governed by the  $sp^3$  fraction, while the  $sp^2$  sites primarily control the optical and electrical properties [1, 14].

Recently, Chhowalla *et al.* [13] in their study of ta-C characteristics as a function of deposition temperature, show that the  $sp^3$  fraction exhibits a “sharp” transition, changing from ~ 80% to ~ 0% at a deposition temperature,  $T_d$ ,  $\approx 250^\circ\text{C}$ , as shown in figure 7.2. The optical gap and film resistivity, however, do not follow the  $sp^2$  content, but decrease gradually with increasing deposition temperature [13]. This behaviour is explained by the theory that the optical and electrical properties are not governed by the overall  $sp^2$  content, but by the size of the clusters of  $sp^2$  bonded carbon, which may vary even though the  $sp^2$  fraction remains constant. It is therefore of interest to examine the EPR signals from these films, and its dependence on deposition temperature, i.e.  $sp^2$  content and cluster size. This section therefore concentrates on five ta-C films grown by Manish Chhowalla in the

Department of Engineering at Cambridge University. The films were grown by filtered cathodic vacuum arc, FCVA, at substrate temperatures of 30, 50, 125, 210 and 325°C, with characteristics as shown in the figure below.

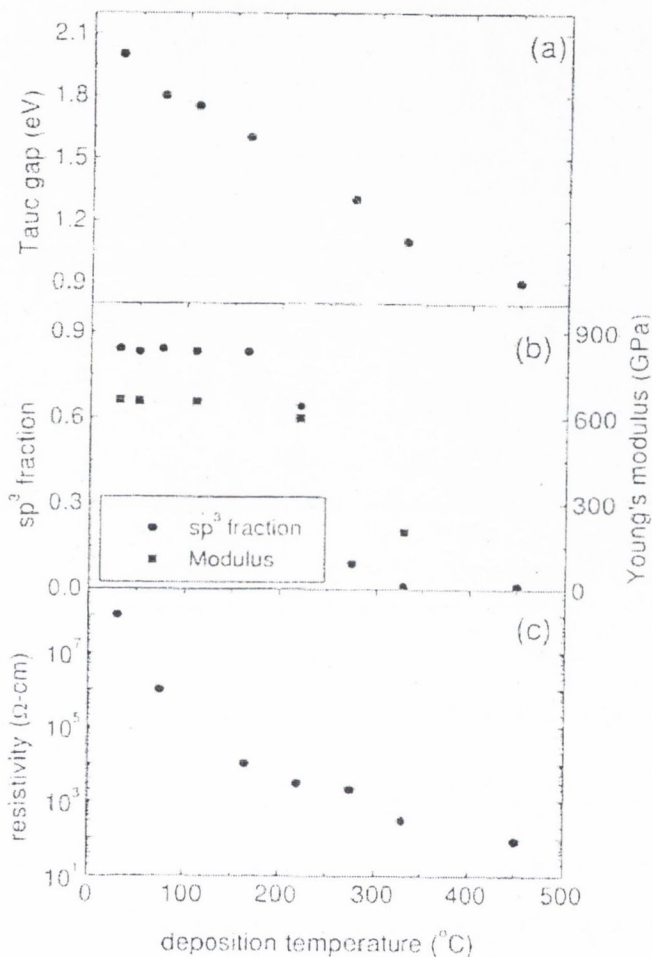


**Figure 7.2** Dependence on deposition temperature of (a) optical band gap (b)  $sp^3$  fraction and Young's modulus and (c) resistivity. The band gap and resistivity fall gradually, while the  $sp^3$  fraction shows a sharp transition [13].

## 7.2.2 Results and discussion

Room temperature X-band electron paramagnetic resonance (EPR) studies revealed symmetric Lorentzian lines with a peak-to-peak linewidth that remained constant at approximately  $(4.3 \pm 0.3)$  G for films deposited at a substrate temperature  $\leq 210^\circ\text{C}$ , but increased to  $37 \pm 7$  G for the film deposited at  $325^\circ\text{C}$ , as shown in figure 7.3(a).

For all films, the areal spin density remained approximately constant at  $(2.3 \pm 0.3) \times 10^{15} \text{cm}^{-2}$  as shown in figure 7.3(b).

Studies [1, 2, 13] of characteristics of a-C films as a function of deposition temperature have shown that there is a transition temperature of  $200\text{-}250^\circ\text{C}$  at which the  $\text{sp}^3$  fraction of the films decreases sharply from the  $\sim 85\%$  of tetrahedral amorphous carbon to 'near zero' [13]. The lack of variation in linewidth below  $210^\circ\text{C}$  has been previously observed in a-C:H [15]. However, other EPR studies, both of ta-C [1] and ta-C:H [2] have shown a sharp decrease in spin density at a temperature around the  $\text{sp}^3$  fraction transition temperature. In addition the linewidth of the resonance line has been seen to gradually decrease with increasing deposition temperature [1, 2].

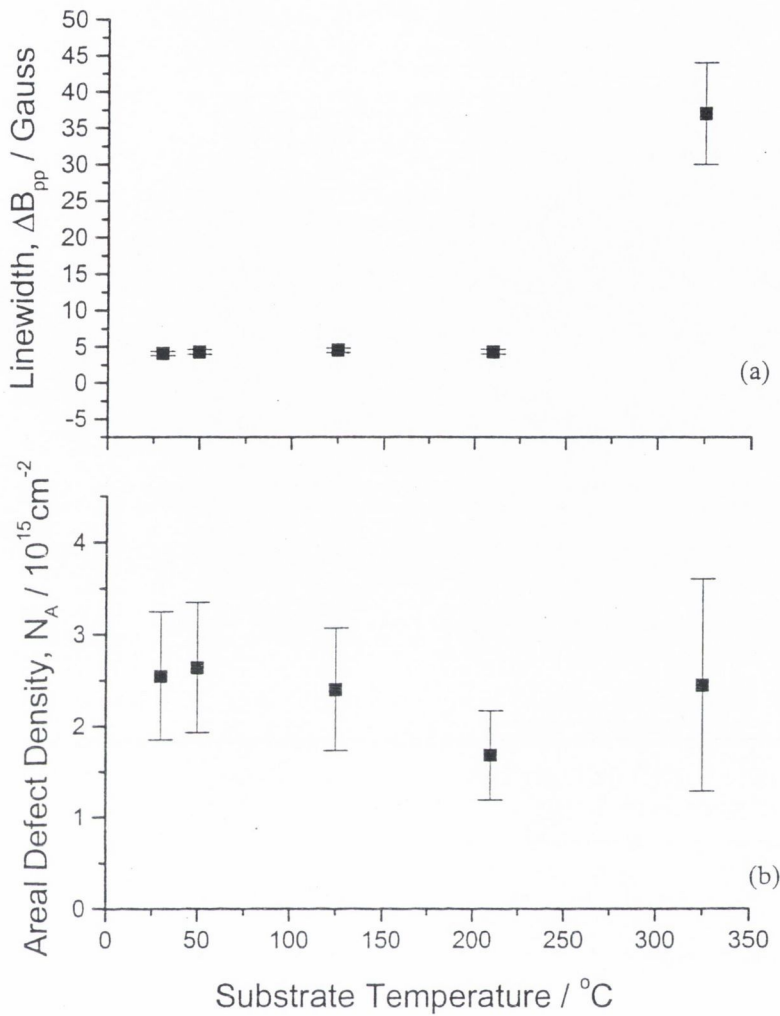


**Figure 7.3** Variation of film properties with substrate temperature

In general, the EPR linewidth can be attributed to dipolar broadening, exchange narrowing or the presence of numerous subsidiary lines, as further detailed in chapter 2. The Lorentzian nature of the lines eliminates inhomogeneous broadening as the main factor determining the linewidth [1]. Other studies show that the linewidth varies in a similar way with  $sp^3$  content in ta-C [1], ta-C:H or a-C:H [2], even though the ta-C contained no hydrogen, suggesting that dipolar broadening due

to interaction with hydrogen nuclei can also be eliminated as a factor. The linewidth of a-C does not vary substantially with microwave excitation frequency, at room temperature, which shows that the line does not consist of unresolved components of differing  $g$  values [12].

The change in linewidth in the above studies [1, 2] has been attributed to exchange narrowing resulting from greater delocalization of the unpaired spins due to the variation with deposition temperature of  $sp^2$  cluster size, which varies inversely with band gap, rather than with the  $sp^2$  fraction [2, 14, 16].

The current study shows an approximately constant areal defect density and a large increase in linewidth above the transition temperature. Assuming nominal thickness, the volume defect density can be calculated and used to ascertain an estimation for the EPR linewidth assuming only dipolar broadening (as in Chapter 4). For all films the predicted width is  $\approx 30\text{G}$ , much greater than the  $4.3 \pm 0.3\text{ G}$  measured for films deposited at  $T_d \leq 10^\circ\text{C}$  and of a similar magnitude to the  $\approx 37\text{G}$  of the  $T_d = 325^\circ\text{C}$  film. Spectroscopic ellipsometry conducted by Chris Smith in Trinity College shows that there is some deviation of film thickness from the nominal value. However, this does not change the calculated volume defect density with sufficient magnitude to account for the change in linewidth by considering only dipolar interactions.

As in section 7.1, the linewidth is much less than that predicted by dipolar broadening alone, suggesting that the spins are in  $sp^2$  clusters, narrowed due to exchange resulting from delocalisation over the aromatic rings. The Tauc gap and

resistivity measurements suggest that the cluster size is growing with increasing deposition temperature (though the total  $sp^2$  content remains the same) [13].

However, the linewidth, and degree of narrowing, remain unchanged, within error, from deposition temperatures from 30°C to 210°C. This suggests that either the cluster size is not in fact changing, or that this process is not the dominant mechanism determining the linewidth. The theory propounded implies that the room temperature film has the smallest cluster size, and thus least narrowing.

However, this film, with 85%  $sp^3$  bonded carbon, has a linewidth narrowed to a greater extent than would be expected for the  $sp^2$  content, suggesting other factors are dominating the width of the EPR line.

As  $T_d$  is increased further to 325°C the linewidth increases dramatically to  $37 \pm 7G$ .

This film is approaching a highly graphite-like state; increases in linewidth have been seen in similar films [7, 12] and are attributed to fast relaxation broadening the line.

Low temperature measurements, conducted at 4-300K, show the presence of additional EPR lines in the 325°C film, visible in X-band measurements below 40K. The magnitude and position of these lines is, however, dependent on the orientation of the sample within the magnetic field. This orientation dependence suggests that these lines are defects within the polycrystalline silicon substrate, rather than in the amorphous film itself. The substantial study of defects in Si is not within the scope of this work. However, the presence of such lines may affect the signal as attributed to a-C.

### 7.2.3 Conclusions

Spin concentration and resonant linewidth measurements of amorphous carbon films grown using a filtered cathodic vacuum arc, FCVA, as functions of substrate temperature are reported. Previous work on these films [13] shows a transition from ~80% to ~0%  $sp^3$  bonded carbon at a deposition temperature,  $T_d \approx 250^\circ\text{C}$ . However, optical and electrical measurements suggest  $sp^2$  cluster size increases with increasing temperature. There is little change in the areal defect density of the films over the entire substrate temperature range studied (30 -  $325^\circ\text{C}$ ). The peak-to-peak linewidth,  $\Delta B_{pp}$ , of the resonance shows little change for substrate temperatures up to  $210^\circ\text{C}$ , and at  $4.3 \pm 0.3\text{G}$  is much less than the  $\approx 30\text{G}$  predicted by dipolar broadening alone. However, the linewidth of the  $325^\circ\text{C}$  film is increased above this by a factor of approximately eight. Both these trends are in contradiction of previous findings [1, 2]. The greater linewidth above the  $sp^2$  transition temperature is attributed to fast relaxation due to the graphitic nature of the film. The linewidth is approximately constant below  $T_d \approx 250^\circ\text{C}$ , and even for room temperature deposition, is significantly narrowed from the dipolar linewidth. This shows that if the size of clusters of  $sp^2$  sites is increasing, thus leading to greater delocalisation of spins and therefore increasing exchange, this is not affecting the linewidth of these ta-C films.

### 7.3 Characteristics of PECVD a-C:H films as a function of rf-power

A set of films was deposited in a plasma enhanced chemical vapour deposition (PECVD) reactor using various rf-powers from 30 to 400W by David Carey at the University of Surrey. The effect of increasing the power at which the films are deposited is to increase the energy of the ions incident on the films surface. I have attempted to measure g value, defect density, linewidth, line-shape, and relaxation times for all films. However, films in the lower section of the power range ( $\leq 80$ W) had a relatively low defect density and thus the signal-to-noise ratio was too low to perform the less rudimentary EPR measurements, for example of line shape and relaxation times, with any degree of accuracy or confidence. Previous studies [15] have suggested that the resonant line-shape tends to become more Gaussian as the power is decreased from 120W. Barklie, Collins *et al.* [8] have conducted similar experiments on films deposited with various powers. This repeated work shows continuity of manufacture – that similar films are obtained using a different reactor (of comparable design) in a different laboratory. These characterisations are also required for future study of these films for use in field emission devices.

There is essentially no change between the EPR signals of films deposited at powers  $> 120$ W; the g value is the typical carbon 2.0027(1) line [8] and the volume defect density is constant, within errors, at  $1.5(3) \times 10^{20} \text{cm}^{-3}$ . The films exhibit relatively fast relaxation times (obtained as described earlier) of approximately  $6 \times 10^{-7}$ s and  $1 \times 10^{-8}$ s for the spin-lattice and spin-spin relaxations respectively. The linewidth

decreases slightly with increasing power over this range and is motionally narrowed by approximately a factor of two from the width predicted by the dipolar broadening model of chapter 4. Reducing the power to 120W causes an increase in the linewidth to 14.9G, which is greater than the value predicted from dipolar-interaction. This may be caused by the presence of hydrogen within the film and a reduction in the exchange narrowing, which is also indicated by the slowing of the spin-lattice relaxation to  $23(4) \times 10^{-7}$ s. This is consistent with previous studies indicating that the  $sp^3$  fraction is at a maximum for films deposited with an energy per carbon atom of  $\approx 100$ eV [6]. The characteristics of the films are summarised in the figure 7.4, below; thanks are due to Dr. Carey for the EPR measurement of the 50W sample.

EPR measurements of the film deposited at 80W rf-power showed a decrease in defect density of approximately a factor of ten from that of the 120W sample, whilst the linewidth remained unchanged (within errors). This may be attributable to the greater hydrogen content of this 80W film. This will decrease defect density by allowing relaxation of stress within the material and may increase the linewidth [1]. Unfortunately there is, with the decrease in defect density, a decrease in the signal-to-noise ratio; thus it has proved impossible to measure relaxation times. Also the determination of the shape of the resonance line becomes more subjective.

I have attempted to fit both Lorentzian and Gaussian lines to the data (figure 7.5); from these fits it seems that the line is perhaps not purely Lorentzian and may contain some Gaussian components, which concurs with previous study [15]. However, I in no way present this result as definitive.

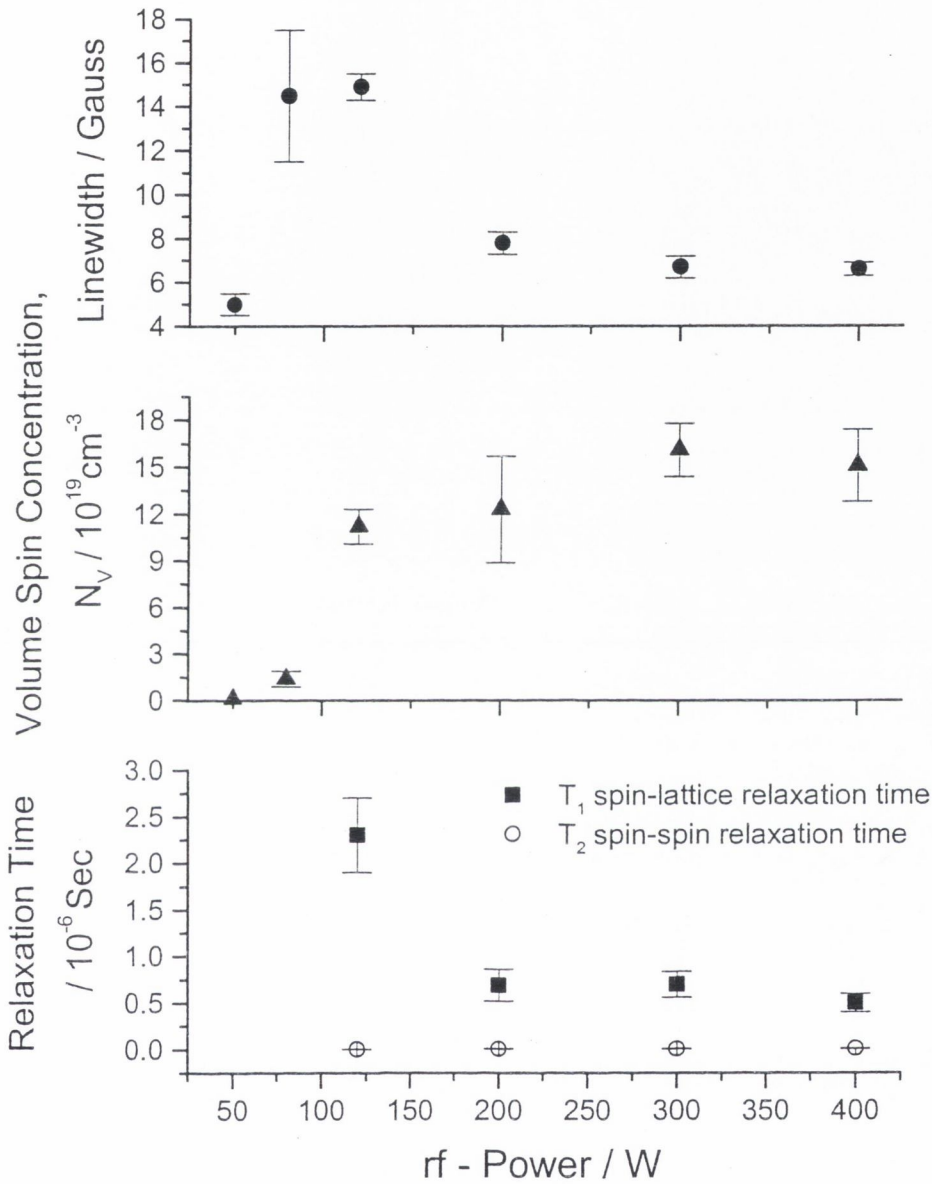


**Figure 7.4** Variation with rf-power of EPR linewidth, spin concentration and relaxation times. Data for 50W sample courtesy of J.D. Carey.

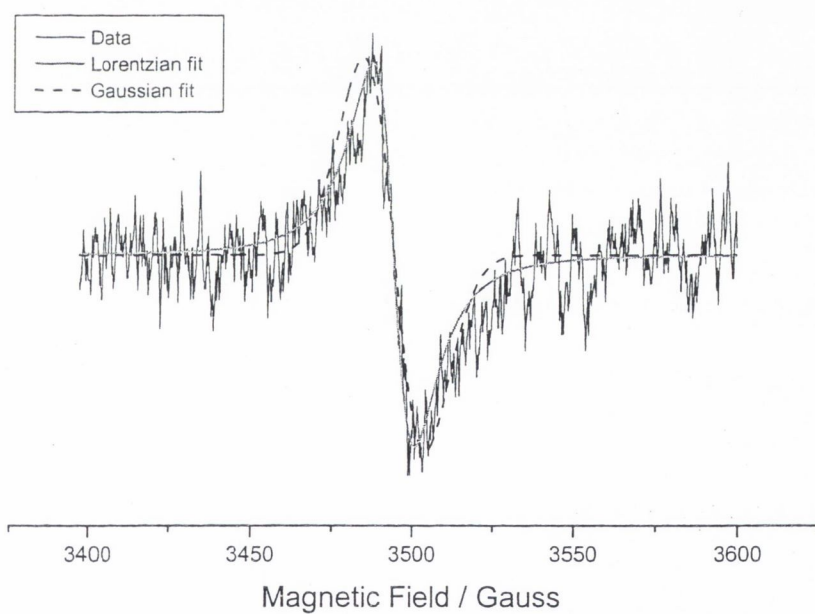


**Figure 7.5.** EPR signal of sample deposited at 80W rf-power, with Lorentzian (solid line) and Gaussian (dashed line) best-fit lines superimposed.

## 7.4 Depth profile of defects in diamond-like carbon films.

### 7.4.1 Introduction

Diamond-like carbon (DLC) films of various thicknesses were prepared by J.Zhao and P. Maguire at the University of Ulster at Jordanstown. The volume defect density,  $N_V$ , in this thesis and other works [7, 8, 17] is taken as the areal defect density divided by the film thickness, but it is not usually known whether the defect distribution is uniform throughout the film. The resultant average defect concentration is often compared to theoretical models [8] assuming even distribution of defects. However, if defects were non-uniformly distributed, for example being concentrated in the carbon-substrate interface, or at the film surface, the use of this calculation for defect density would be untenable, and the values obtained cannot satisfactorily be compared with the standard models for the EPR linewidth, and other parameters.

In this work I determine areal defect density in diamond-like carbon as a function of film thickness from 5nm to 100nm, with the aim of examining the depth profile of defects within the sample, including studying the concentration and nature of any defects contained in the silicon-carbon interface region. This complements work by Collins *et al.* [18] showing uniformity of distribution of defects in polymer-like films, and is a preliminary study for further development of DLC films as a thin hard-disk coating.

## 7.4.2 Experimental

The a-C:H films were deposited on silicon of resistivity  $\sim 30 \Omega \text{ cm}$  using a 13.56 MHz rf-powered plasma enhanced chemical vapour deposition (PECVD) system. Films were deposited using a 10:20 Ar:C<sub>2</sub>H<sub>2</sub> mixture, following a two minute pre-clean of argon only at 60sccm.

Films were grown to thicknesses of approximately 5, 10, 25, 50 and 100 nm. All the samples were loaded and then individual samples removed after a set time; therefore the thickest samples have their films built up over a series of runs. This method, as opposed to one run per thickness, has the advantage of keeping the Si / a-C:H interface conditions the same for each sample, and not subject to run-by-run variations.

X-band EPR measurements were made at room temperature, following the standard procedures as outlined in chapter three.

Some samples were produced with a 'stripe', a section of the substrate on which no film was deposited, to enable thickness measurements. Atomic force microscopy, AFM, was used to measure film thickness. Measurements were taken at three places along the stripe and on the deposited film, allowing an average film thickness and standard deviation to be calculated from the AFM data. For brevity the films

are referred to throughout the text by their nominal thicknesses; however, the measured thickness is used in all calculations.

### 7.4.3 Results and discussion

#### 7.4.3.1 Defect Densities

EPR studies of films of thickness  $\geq 10\text{nm}$  revealed a paramagnetic defect with a single, symmetric, Lorentzian line at  $g=2.0026(1)$ ; the shape and  $g$  value suggest that this is the usual defect associated with carbon unpaired electrons within the film [8, 18]. Plotting the areal defect density, i.e. the total defect density divided by the area of one face of the sample, versus measured thickness (which varies in a non-linear fashion with deposition time [19]), as in figure 7.6(a), shows that the areal defect density is proportional, within error, to the film thickness. A linear fit to this data gives a carbon defect density of  $(3.12 \pm 0.04) \times 10^{20} \text{cm}^{-3}$ . There is uncertainty in the y-intercept of the fit; thus the data is consistent with there being an areal defect  $\leq 3.4 \times 10^{13} \text{cm}^{-2}$  attributable to defects within the silicon and interface. This is consistent with work by Collins *et al.* [18] who find, in addition to the carbon defect with density proportional to film thickness, an areal defect density of  $5 \times 10^{12} \text{cm}^{-2}$  in each of their films, which they attribute to silicon dangling bonds associated with the substrate and possibly the interface region. Compared to the DLC in this study, the polymer-like carbon examined by Collins has a lower carbon defect density, thus allowing the calculation of the interfacial / substrate defect density to a greater precision.

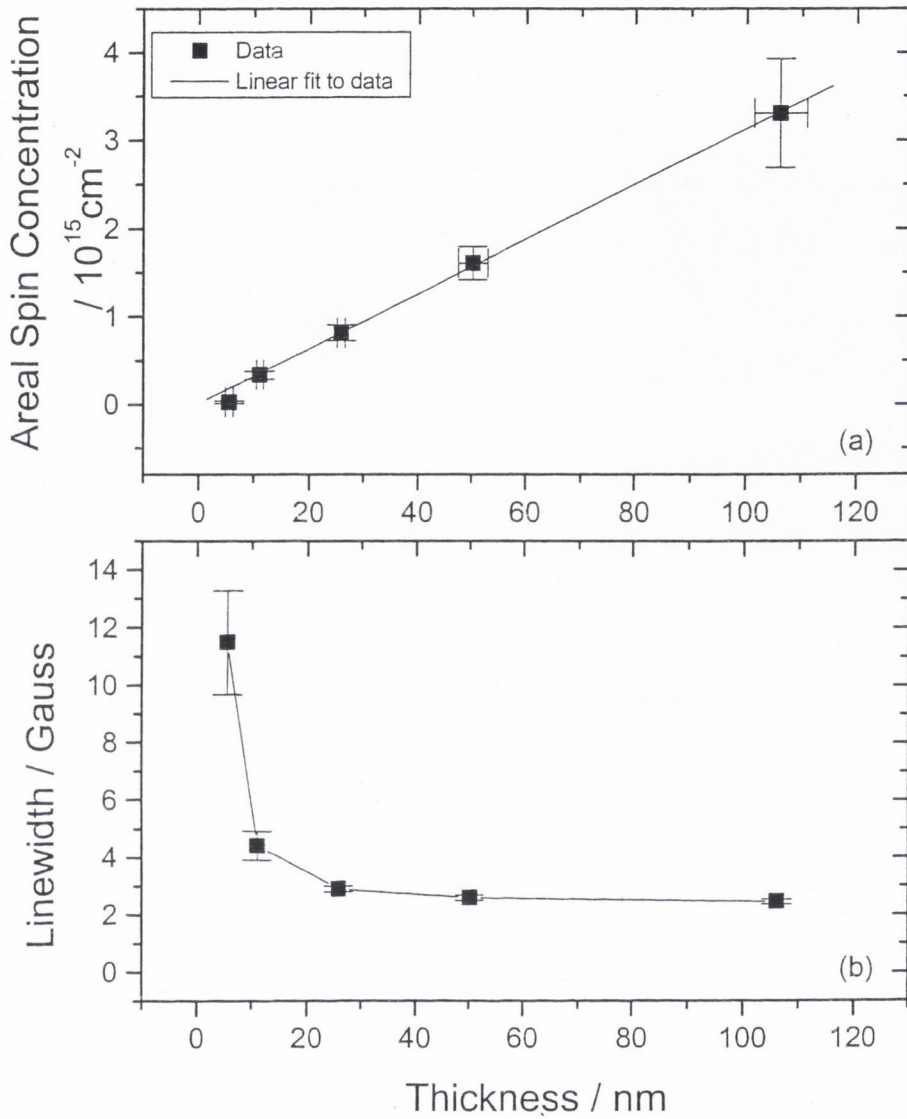


**Figure 7.6** Variation, with film thickness, of (a) areal concentration of carbon defect, with a linear fit to the data, and (b) peak-to-peak linewidth of resonance line

Support for the presence of substrate / interfacial defects comes from the study of the 5nm thick film. The EPR resonance line from this film has a  $g$  value of 2.0043(7) which possibly corresponds to a superposition of a line due to carbon defects ( $g \approx 2.0026$ ) and a line from defects in the silicon substrate or interface with  $g \approx 2.006$  as found in previous studies [11, 18].

#### 7.4.3.2 Linewidths and relaxation times

The peak-to-peak linewidth of the resonance line increases from  $0.245 \pm 0.008$  mT for the film of thickness 100nm to  $1.15 \pm 0.18$  mT for the 5nm film, as shown in figure 7.6(b). An estimation of the peak-to-peak linewidth contribution due to dipolar interactions alone can be calculated from the volume defect density [8]. A defect density of  $3.3 \times 10^{20} \text{ cm}^{-3}$  (as in films  $\geq 10$ nm thickness) would produce a Lorentzian line of  $\approx 2.7$  mT. For the 5nm film, the measured defect density is somewhat less than suggested by the linear fit; thus the predicted linewidth is 0.44mT. However, the error in these predictions is due to errors in thickness and areal defect density; thus for the 5nm film the error is  $\approx 90\%$ , 34% for the 10nm film and 15 - 20% for the other samples. The narrowing of the linewidth below that predicted for simple dipolar broadening, as in films of thickness  $\geq 10$ nm, may be accounted for by motional averaging resulting from greater wavefunction overlap. This in turn may arise from delocalisation due to a large  $sp^2$  cluster size [11, 14, 16]. The degree of narrowing seems to be smaller in the 10 and 5nm thick films than in the thicker samples. The most likely cause is that the observed line is broadened due to an increasing relative contribution from a line at  $g \approx 2.006$  due to defects associated with the substrate, as suggested by the change in  $g$  value of the resonance

line. However, it may be that the formation of a  $\sim 1\text{nm}$   $\text{sp}^2$  rich top-layer and / or a 5-10nm interface region, where bonding is different from that in the bulk of the sample, contribute to the effects seen in these thinner films [3, 12]; thus we would not expect the defects to vary as those in the bulk of the material.

Relaxation time studies on films of thickness 10 - 100nm, carried out as described in previous sections, showed little change in the saturation behaviour of the resonant signal with film thickness.

#### 7.4.4 Conclusions

For films of thickness 10 - 100nm the areal defect density,  $N_A$ , of the carbon defect at  $g=2.0026(1)$  increases approximately linearly with thickness at a rate of  $(3.12\pm 0.04)\times 10^{20}\text{cm}^{-3}$ . This indicates that the carbon defect is uniformly distributed through the bulk of the film. In addition, the data is consistent with the existence of a defect within the substrate and interface region that has an areal density,  $N_A \leq 3.4\times 10^{13}\text{cm}^{-2}$ . The existence of the substrate / interfacial defect is supported by the  $g$  value of the EPR signal of the 5nm film which, at 2.0043(7), suggests the presence of a defect other than the carbon dangling bond defect [11, 18].

The peak-to-peak linewidth of the resonance ( $0.25\pm 0.01$  mT for a 100nm film) is narrowed below that expected for dipolar broadening ( $2.5\pm 0.6$  mT) [8]. This is attributed to motional narrowing of the signal, resulting from greater wavefunction overlap. This in turn may arise from increased delocalisation due to an increase in  $sp^2$  cluster size [11, 14, 16]. The EPR linewidth is broader in films with low thicknesses; this may be due to the presence of an unresolved line at a different  $g$ -value arising from defects within the silicon or interface [8, 11, 18]. The EPR signal may also be affected by the presence of an interface region and surface region, with different bonding and constituents from the bulk, which in these thin films may be of comparable thickness to the film itself [3].

## 7.5 References

- [1] M. Chhowalla, J. Robertson, C.W. Chen, S.R.P. Silva, C.A. Davis, G.A.J. Amaratunga, W.I. Milne *J. Appl. Phys.* 81(1997)139
- [2] S. Sattel, J. Robertson, H. Ehrhardt *J. Appl. Phys.* 82(1997)4566
- [3] C.A. Davis, G.A.J. Amaratunga, K.M. Knowles *Phys. Rev. Lett* 80(1998)3280
- [4] C.A. Davis, K.M. Knowles, G.A.J. Amaratunga *Surf. Coat. Technol.* 76-77(1995)316
- [5] B. Kleinsorge, A. C. Ferrari, J. Robertson, W.I. Milne, S. Waidmann, S. Hearne *Diamond Relat. Mater.* 9(2000)643
- [6] M. Weiler, S. Sattel, T. Giessen, K. Jung, H. Ehrhardt *Phys. Rev. B.* 53(1996)1594
- [7] R.C. Barklie, M. Collins, J. Cunniffe, S.R.P. Silva *Diamond Relat. Mater* 7 (1998) 864
- [8] R.C. Barklie, M. Collins, S.R.P. Silva *Phys. Rev. B* 61 (2000) 3546
- [9] C.A. Davis, D.R. McKenzie, Y. Yin, E. Kravtchinskaia, G.A.J. Amaratunga, V.S. Veerasamy *Phil. Mag. B* (1994)1133
- [10] J. Hu, P. Yang, C.M. Leiber *Phys. Rev. B* 57(1998)R3185
- [11] B. J. Jones, R.C. Barklie, R.U.A. Khan, J.D. Carey, S.R.P. Silva *Diamond Relat. Mater.* 10(2001)993
- [12] M. Hoinkis, E.D. Tober, R.L. White, M.S. Crowder *Appl. Phys. Lett* 61(1992)2653

- [13] M. Chhowalla, A.C. Ferrari, J. Robertson, G.A.J. Amaratunga *Appl. Phys. Lett.* 76(2000)1419
- [14] J. Robertson, E.P. O'Reilly *Phys. Rev. B* 35(1987)2946
- [15] M. Collins *PhD Thesis* University of Dublin (1999) ch.4
- [16] J. Robertson *J. Non-Cryst. Solids* 198-200(1996)615
- [17] G. Fanchini, S.C. Ray, A. Tagliaferro, E. Laurenti *Diamond Relat. Mater.* 11(2002)1143
- [18] M. Collins, R.C. Barklie, J.V. Anguita, J.D. Carey, S.R.P Silva *Diamond Relat. Mater.* 9 (2000) 781
- [19] P.D. Maguire *Personal communication* (28 Sept. 2000)

## *Chapter 8*

### *Conclusions*

What can be said at all can be said clearly;  
and whereof one cannot speak thereof one  
must be silent.

Ludwig Wittgenstein

## 8. Overall conclusions

This thesis is an investigation into paramagnetic defects in thin carbon films, their nature and the effects of deposition parameters and post deposition treatments on the defects. Electron paramagnetic resonance (EPR) is used to examine samples with a wide range of structures from the hard tetrahedral amorphous carbons (ta-C) with a high percentage of  $sp^3$  bonded carbon, to soft polymer-like films with high hydrogen concentrations, grown by plasma enhanced chemical vapour deposition at low bias.

Some samples were, post manufacture, subjected to implantation of a range of ion species with doses of up to  $2 \times 10^{16} \text{cm}^{-2}$ . The EPR measurements show that ion implantation creates two types of paramagnetic centres, the carbon defect with  $g=2.0028(1)$  in the film and another defect in the silicon substrate. The carbon defect has a volume spin density that increases approximately linearly with dose, from  $3 \times 10^{17} \text{cm}^{-3}$  for unimplanted samples [1] to  $2.7 \times 10^{20} \text{cm}^{-3}$  for implantation of  $2 \times 10^{16}$  ions  $\text{cm}^{-2}$ . The silicon defect within the substrate has a  $g$  value of  $2.0058(6)$  and a spin concentration that saturates at about  $4 \times 10^{13} \text{cm}^{-2}$  at a boron dose of  $6 \times 10^{14}$  ions  $\text{cm}^{-2}$ . At high doses the carbon line narrows (to 0.13 mT at  $2 \times 10^{16}$  ions  $\text{cm}^{-2}$ ), and the spin-lattice relaxation time decreases and approaches the spin-spin relaxation time; this is attributed to exchange (motional) narrowing of the signal, resulting from greater wavefunction overlap. This in turn may arise from increased delocalisation due to an increase in  $sp^2$  cluster size, which is revealed by the fall in Tauc gap [2, 3]. Annealing of ion-implanted samples at  $550^\circ\text{C}$  causes an increase in the carbon defect density, which is greater for films with lower implantation dose,

and is attributed to loss of hydrogen. Annealing at temperatures  $\leq 350^\circ\text{C}$  causes no change in the EPR spectrum.

EPR was carried out at a range of temperatures (5-300K) and at two frequencies ( $\approx 9.5\text{GHz}$  and  $\approx 94\text{GHz}$ ). Studied under these conditions are a series of films deposited in a PECVD reactor with a range of bias voltages to give a variety of structures, and two samples implanted with  $6 \times 10^{15}\text{cm}^{-2}$  or  $2 \times 10^{16}\text{cm}^{-2}$  boron ions. Room temperature EPR shows that there is little or no increase in the width of the resonance line, of any sample, when the microwave frequency is increased by a factor of ten from X- to W-band ( $\approx 9.5\text{GHz}$  to  $\approx 94\text{GHz}$ ). This confirms earlier work [4] and shows that the resonance observed consists of one single symmetric line at  $g = 2.0026(2)$  and that there is no linewidth component due to a spread in  $g$ -values.

The temperature dependence of the susceptibility shows adherence to the Curie law at temperatures above  $\approx 13\text{K}$ . Below this temperature some deviation from this dependence may occur, possibly due to the onset of local magnetic ordering [5] of spin clusters [2, 3]. Further evidence of magnetic ordering comes from the presence of a magnetic hysteresis loop at 5K, although analysis of impurities within the film or substrate could show that this hysteresis is not due to carbon unpaired spins.

Measurements of the temperature dependence of the X-band EPR linewidth and relaxation times show that exchange interaction, rather than variable range hopping, becomes increasingly dominant as the  $sp^2$  content of the films is increased. Strong evidence for this is the highly “graphite-like” sample, which shows no variation of

linewidth or relaxation time, within error, over the entire temperature range studied [6].

Measurements on DLHC and GLHC show that the position of resonance at low temperature displays a dependence on the orientation of the sample within the field. Detailed analysis shows that this anisotropy can be attributed to shape effects associated with the anisotropy of the demagnetising field, as suggested in previous works [7, 8]. In these films the effect can be explained in terms of magnetization of unpaired carbon electrons, though there could be contributions from spin ordering and /or impurities. The maximum effect in the more polymer-like samples is, however, less than would be expected from this analysis.

In contrast to the X-band measurements, at W-band the linewidths of the diamond-like and graphite-like films increase substantially as the temperature is lowered from room temperature to 5K (the strongest increase, from 4.8G to 24.3G, is seen in sample C320). This increase in width is correlated with, and is of approximately the same magnitude as, the shift in resonance position. Thus the broadening of the line is attributed to variation in the demagnetising field over the sample, causing a spread in effective  $g$  value and therefore increasing the linewidth.

For all films at all temperatures and frequencies studied, the EPR signal due to unpaired carbon spins is observed to be a single symmetric line. No evidence was found of the powder patterns observed by von Bardeleben *et al.* [9] and attributed to unpaired spins in graphite-like clusters.

A study of the depth profile of defects, using a series of DLC films of thicknesses ranging from 5 to 100nm showed, for thicknesses  $\geq 10$ nm at least, that defects are uniformly distributed throughout the film. Studies on ta-C showed that paramagnetic defects are not concentrated in the  $sp^2$  layer on the surface of the film, despite the EPR signal suggesting that spins are located in  $sp^2$  regions of these highly  $sp^3$  films.

Finally, carbon nitride films are examined. Nitrogen incorporation into a-C:H films is shown to decrease the defect density in all types of films studied. This is attributed to a decrease in the disorder of the  $sp^2$  structure, the aromatic rings becoming less buckled and distorted and thus allowing greater delocalisation. The linewidth decrease associated with this fall in spin density, as predicted by a model assuming dipolar broadening, is observed only for polymer-like films.

Measurements show that nitrogen acting as a dopant can only be within the film at a density of at most  $\sim 10^{12} \text{ cm}^{-2}$ , which corresponds to at most only one in one million of the incorporated nitrogen atoms acting as donors. However, an increase in the contribution to the linewidth due to unresolved nitrogen hyperfine structure is suggested by a Gaussian component of the lineshape, the intensity of which seems to increase with increasing nitrogen content. This, and a reduction in exchange narrowing for the highly nitrogenated films, as indicated by the lengthening relaxation times, could outweigh the effect of the dipolar interaction and lead to the broadening of lines with the addition of nitrogen, as observed in the more diamond-like films.

In summary, this work provides a comprehensive, coherent picture of the nature of paramagnetic defects within amorphous carbon thin films.

## 8.1 References

- [1] M. Collins, R.C. Barklie, J.V. Anguita, J.D. Carey, S.R.P. Silva *Diamond Relat. Mater.* 9 (2000) 781
- [2] J. Robertson, E.P. O'Reilly *Phys. Rev. B* 35(1987)2946
- [3] J. Robertson *J. Non-Cryst. Solids* 198-200(1996)615
- [4] M. Hoinkis, E.D. Tober, R.L. White, M.S. Crowder *Appl. Phys. Lett* 61(1992)2653
- [5] D. Arčon, P. Cevc, R. Blinc, I. Pocsik, M. Koos, Z. Trontlj, Z. Jagličič in “*Molecular Nanostructures*” H. Kuzmany, J. Fink, M. Mehring, S. Roth Eds. World Scientific Pub. Co. Singapore (1998)533
- [6] J.P. Goldborough, M. Mandel, G.E. Pake *Phys. Rev. Lett.* 4(1960)13
- [7] B. Druz, I. Zaritskiy, Y. Yevtukhov, A. Konchits, M. Valakh, S. Kolesnik, B. Shanina and V. Visotski, *Materials Research Society Symposium Proceedings* 593(2000)249
- [8] V.V. Afanas'ev, A. Stesmans, M.O. Andersson *Phys. Rev. B* 54(1996)10820
- [9] H.J. von Bardeleben, J.L. Cantin, A. Zeinert, B. Racine, K.Zellama, P.N. Hai *Appl. Phys. Lett.* 78(2001)2843

## *Appendices*

Merely corroborative detail, intended to  
give artistic verisimilitude to an otherwise  
bald and unconvincing narrative .

-W.S. Gilbert

## A. Temperature dependence - Calculating $\chi$

Poole [1] shows that the absorption of power at resonance leads to a change in the Q,  $\Delta Q$ , of the cavity, given by

$$\Delta Q = \chi'' \eta Q_U^2$$

where  $Q_U$  is the Q value off resonance and  $\eta$  is a filling factor, needed as the sample does not totally fill the cavity, and given by:

$$\eta = \frac{\int_{\text{sample}} B_1^2 dV}{\int_{\text{cavity}} B_1^2 dV}$$

Poole [1] shows that for a set-up such as the X-band EPR system used here, with a reflection cavity and linear detector, and for optimum coupling, the change in reflected voltage at resonance,  $\Delta E_r$  (as measured by the detector diode) is given by:

$$\frac{\Delta E_r}{E} = \frac{\Delta Q}{2Q} = \frac{1}{2} \chi'' \eta Q_U$$

where  $E$  ( $\propto P^{1/2}$ ) is the voltage incident on the cavity,

therefore,

$$\Delta E_r = \frac{1}{2} \chi'' \eta Q_U E$$

The expression for  $\chi''$  in equation 3.11 can be rewritten, ignoring the  $B_1^2$  term, which is negligible in the absence of saturation, as:

$$\chi'' = \frac{1}{2} \chi_0 \omega_0 g(\nu)$$

$$\text{where } g(\nu) = \frac{2T_2}{1 + (\omega_0 - \omega)T_2^2} \text{ and } \int_0^{\infty} g(\nu) d\nu = 1$$

Therefore the voltage change at the detector becomes:

$$\Delta E_r = \frac{1}{4} \chi_0 \eta \omega_0 Q_U E g(\nu)$$

The measured area under the EPR absorption curve,  $A$ , is given by the integral of the change in voltage, over all frequencies. Therefore:

$$A = \frac{1}{4} \chi_0 \eta \omega_0 Q_U E$$

For two different samples then:

$$\frac{A_1}{A_2} = \frac{(\chi_0 \eta \omega_0 Q_U E)_1}{(\chi_0 \eta \omega_0 Q_U E)_2}$$

Thus when the values for area under the curve are normalised to a particular power (and therefore  $E$ ),  $Q$ , sample shape, gain etc, this reduces to:

$$\text{A.1} \quad \frac{A_1}{A_2} = \frac{\chi_{01} V_1}{\chi_{02} V_2}$$

where  $V_i$  is the volume of the sample. Thus knowing the susceptibility of one sample EPR allows the calculation of susceptibility of another, assuming the ratio of the sample volumes is known.

The calibration standard, pitch in KCl, has a Curie-like susceptibility. From chapter six:

$$\text{6.2} \quad \chi_c = \frac{\mu_0 N g^2 \mu_B^2 J(J+1)}{3kT}$$

where  $N$  is the number of spins per unit volume.  $J=S=1/2$ ,  $g=2$ ; thus this reduces to:

$$\text{A.2} \quad \chi_{\text{std}} = \frac{\mu_0 N \mu_B^2}{kT}$$

$$\text{Therefore, } (\chi V)_{\text{std}} = \frac{\mu_0 \mu_B^2 N_{\text{Tot}}}{kT}$$

where  $N_{\text{Tot}}$  is the total number of spins.

For the pitch in KCl standard used for calibrations throughout my X-band measurements, in the TE<sub>012</sub> cavity,

$$(\chi V)_{\text{std}} = 9.520 \times 10^{-17} \text{ m}^3$$

Thus, after normalising the measured area under the absorption curve of the KCl standard, the susceptibility of any sample can be calculated from:

$$\text{A.3} \quad \chi_{\text{sample}} = \frac{A_{\text{sample}}}{A_{\text{std}}} \cdot \frac{9.520 \times 10^{-17} \text{ m}^3}{V_{\text{sample}}}$$

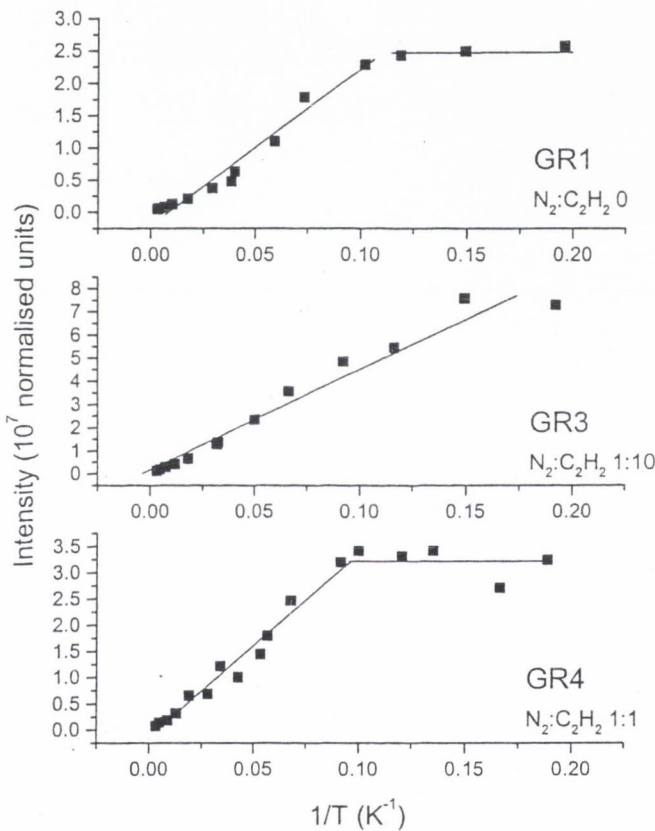
The value of  $A_{\text{std}}$  depends on the cavity used and the presence of cryo-apparatus etc. within the cavity, and is recalculated as necessary.

## Reference

- [1] C.P. Poole "*Electron Spin Resonance, A Comprehensive Treatise on Experimental Techniques*" John Wiley and Sons, New York (1983)

## B. Temperature dependence – Measuring $\chi$

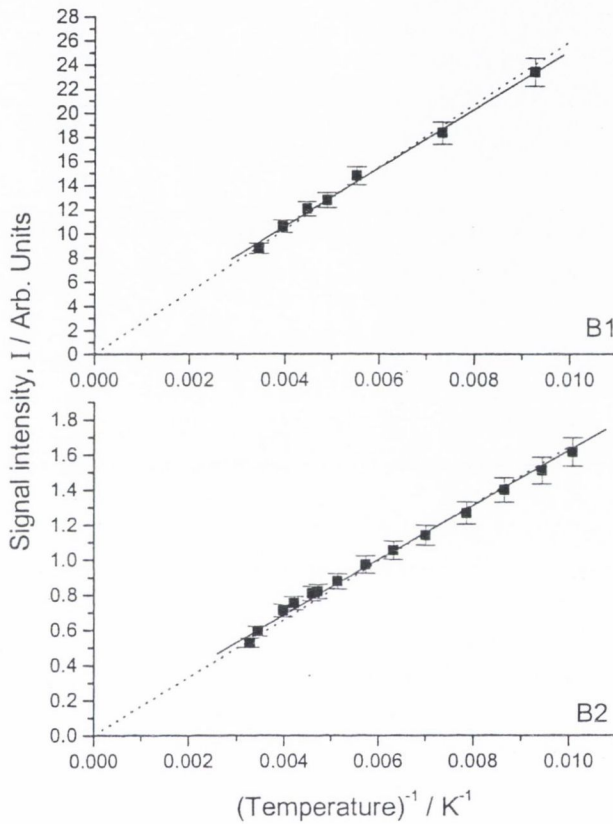
This appendix supplements the work covered in section 6.3 and is a repository for additional plots showing EPR signal intensity, and susceptibility, as a function of temperature. This is to provide a complete record of the temperature dependence of the EPR intensity of all samples studied.



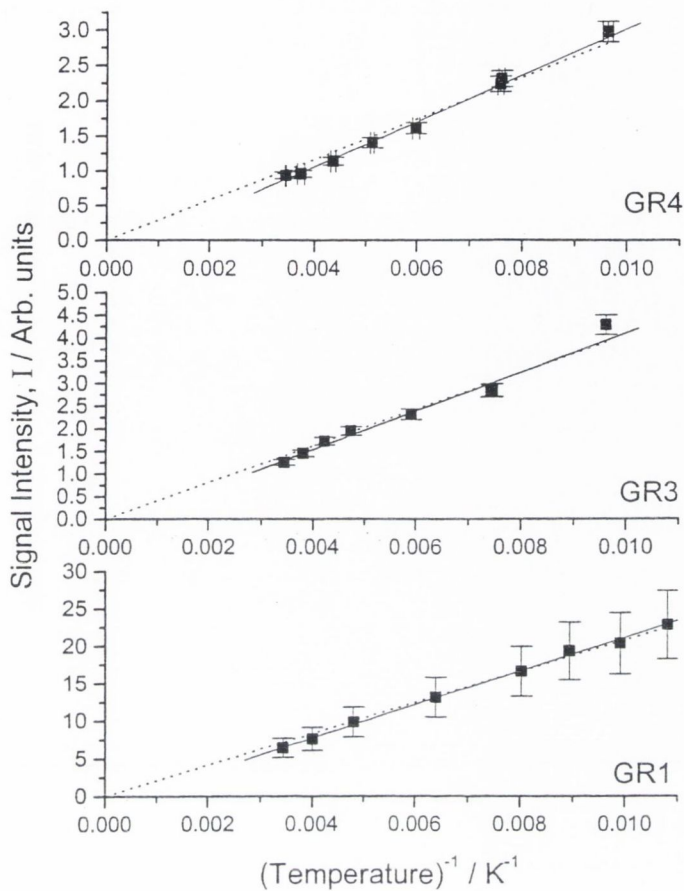
**Figure B.1** Temperature dependence, measured at X-band, of EPR intensity of carbon nitride samples GR1, GR3, GR4. Precursor gas ration as indicated, lines are guides to the eye.

Figure B.1 shows the temperature dependence of the EPR signal of carbon nitride samples, to a temperature of  $\approx 5K$ . Similarly to the a-C:H studied, some of these films exhibit a deviation from the expected Curie-like behaviour, at temperatures  $\leq 10K$ .

Figures B.2, B.3 and B.4 show signal intensity ( $\propto$  susceptibility) as a function of temperature, in the range  $\approx 90\text{K} - 300\text{K}$ , from experiments using liquid nitrogen as a coolant. This temperature range is also studied as part of experiments using liquid helium, which are included in the text.



**Figure B.2** X-band EPR signal intensity versus  $(\text{temperature})^{-1}$  of B1 and B2. Solid lines indicate linear fit, dotted lines indicate fit to  $I = C/T$ .



**Figure B.3** X-band EPR signal intensity versus  $(\text{temperature})^{-1}$  of GR1, GR3 and GR4. Solid lines indicate linear fit, dotted lines indicate fit to  $I = C/T$ .

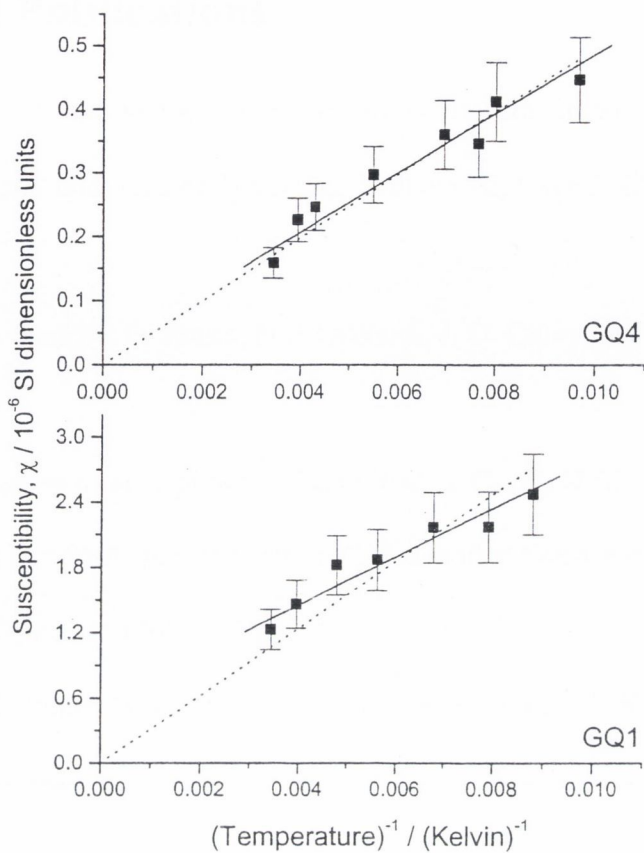


**Figure B.4** Susceptibility, measured at X-band, versus  $(\text{temperature})^{-1}$  of GQ1 and GQ4. Solid lines indicate linear fit, dotted lines indicate fit to  $I = C/T$ .

## C. Related Publications

“An EPR study at X- and W-band of defects in a-C:H films in the temperature range 5–300 K”, *Diamond and Related Materials*, Volume 12, Issue 2, (2003), Pages 116-123

B. J. Jones, R. C. Barklie, G. Smith, H. El Mkami, J. D. Carey and S. R. P. Silva

“Electronic properties of amorphous carbon nitride a-C<sub>1-x</sub>N<sub>x</sub>:H films investigated using vibrational and ESR characterizations”, *Journal of Non-Crystalline Solids*, Volumes 299-302, Part 2, (2002), Pages 907-911

M. Lacerda, M. Lejeune, B. J. Jones, R. C. Barklie, R. Bouzerar, K. Zellama, N. M. J. Conway and C. Godet

“Electron paramagnetic resonance study of ion implantation induced defects in amorphous hydrogenated carbon”, *Diamond and Related Materials*, Volume 10, Issues 3-7 (2001) Pages 993-997

B. J. Jones, R. C. Barklie, R. U. A. Khan, J. D. Carey and S. R. P. Silva

“Electron delocalisation in amorphous carbon by ion implantation”  
*Physical Review B (Condensed Matter and Materials Physics)*, volume 63, (2001)  
121201(R)

R. U. A. Khan, J. D. Carey, S.R.P. Silva, B.J. Jones and R.C. Barklie,